YIN, ZIYU, Ph.D. Hybrid Nanomaterials Based on Carbon Nanotubes (CNTs) and Nanofibers (CNFs) for Electrocatalytic and Biosensing Application. (2021)
Directed by Dr. Jianjun Wei. 151 pp.

As the field of materials science and engineering has become more well developed and advanced, the demand for highly functionalized materials with new characteristics for future purposes has risen. In particular, more and more new discoveries have merged from interdisciplinary into a central hub of hybrid nanomaterials and composites. Briefly, hybrid materials are a result of constituting with two or more components via formation of chemical and physical interactions, such as Van der Waal, hydrogen bonding, weak electrostatic interaction or covalent bonds. Herein, hybrid materials not only inherit some of merits and functions from those constituents, but also acquire some new physicochemical properties that were not present in individual components.

Carbon based nanomaterials have attracted paramount attention in the materials and biosensor communities owing to a large number of their unique properties, including improved mechanical, electrical, thermal, biocompatibility and catalytic virtues. Among different allotropes of carbon ranged from 0D to 3D structures, 1D filamentous forms of carbon, in terms of carbon nanotubes (CNTs) and carbon nanofibers (CNFs), are very attractive materials for a broader research community, taking one of the striking advantages in their superior length to width ratio (>1,000) with a high specific area. Thus, there is an emerging opportunity to design and create multi-functional hybrid nanomaterials based on carbon nanomaterials with various organic/inorganic materials at

the nanoscale or molecule level, exhibiting great potential in electronics, catalysis, sensors and energy conversion and storage.

This dissertation includes three research thrusts using hybrid carbon nanomaterials. 1) We investigated the direct electrochemistry of glucose oxidase (GOx) entrapped into a single-wall carbon nanotubes (SWCNTs)-poly(ethylenimine) (PEI) matrix under presence of glucose. We found the direct electrochemistry and ET kinetics of the GOx were impacted by glucose and correlated to its concentration. This finding may offer a promising way for the development of reagentless or mediator-free glucose biosensors or biofuel cells. 2) We examined the synergistic effect of mingled binary metal oxide (MnO_2/Co_3O_4) on well-aligned electrospun carbon nanofibers (WA-ECNFs) towards electrocatalytic oxidation of glucose and a non-enzymatic glucose sensor. The results demonstrate a superior electrocatalytic performance due to the nanostructure feature of the binary metal oxides interfaces. 3) We studied nitrogen dopant in ECNFs (NECNFs) for the nucleation of metal oxide nanoparticles (Co_3O_4) and exploited the electrochemical performance towards selective detection of dopamine. We found the N dopant could induce the nucleation and growth of cobalt oxide nanoparticles (nanograin morphology) via strong covalent coupling effect, sustaining improved catalytic effect in contrast to the smoothly deposited Co_3O_4 film without the N-dopant. The Co_3O_4@NECNFs electrode demonstrated rapid responsive and highly sensitive, in-situ, real-time monitoring dopamine secreted by living cells. In summary, the findings in this dissertation work present advanced knowledge associated with novel nanohybrid structures and the structure-property-performance. We hope this research can promote the development of new hybrid materials and composites, thereby benefiting our lives in human society.

HYBRID NANOMATERIALS BASED ON CARBON NANOTUBES (CNTS) AND NANOFIBERS (CNFS) FOR ELECTROCATALYTIC AND BIOSENSING APPLICATION

by

Ziyu Yin

A Dissertation Submitted to
the Faculty of The Graduate School at
The University of North Carolina at Greensboro
in Partial Fulfillment
of the Requirements for the Degree
Doctor of Philosophy

Greensboro
2021

Approved by

Dr. Jianjun Wei

Committee Chair

APPROVAL PAGE

This dissertation written by ZIYU YIN has been approved by the following committee of the Faculty of The Graduate School at The University of North Carolina at Greensboro.

Committee Chair	Dr. Jianjun Wei
Committee Members	Dr. Dennis R. LaJeunesse
	Dr. Tetyana Ignatova
	Dr. Eric Josephs
	Dr. Lifeng Zhang

03/11/2021
Date of Acceptance by Committee

03/11/2021
Date of Final Oral Examination

ACKNOWLEDGMENTS

First and foremost, I would like to express my deep and sincere gratitude to my advisor, Dr. Jianjun Wei, for his persistent support and invaluable guidance within my whole Ph.D. period. His insights towards problems also inspires me to think issues deeply as well as expand my ideas. In particular, he is not only my academic mentor, but also plays a role of wise man in my life journey. To be honesty, I feel so lucky to become a student in his group.

Next, I would like to thank my committee members, Dr. Eric Josephs, Dr. Tetyana Ignatova, Dr. Dennis R. LaJeunesse and Dr. Lifeng Zhang for their guidance and insight comments to guarantee the implementation of my project. In addition, I am also thankful to my teachers, Dr. Ajit Kelkar and Dr. Joseph Starobin, Dr. Hemali Rathnayake, Dr. Dan Herr and Dr. Christopher Kepley, who have guided me over these years as well.

Subsequently, I would like to thank to my lovely group members, Dr. Xinping Zeng, Dr. Zheng Zeng, Dr. Yiyang Liu, Dr. Taylor Mabe, Dr. Harish Chevva, Dr. Wendi Zhang, Dr. Zuowei Ji, Dr. Alex Sheardy, Dr. Durga Arvapalli, Kokougan Allado, Anitha Jayapalan, Mengxin Liu, Frank Tukur and Mahsa Azami. I feel so lucky to study and collaborate in such big and lovely group. I wish all of you every happiness and all the best.

Last but not least, I would like to express my greatest love to my family. They are always my strongest support and let me focus my achievement without any worries of the

rear. I would never go so far without their support and love. Thus, I wish they are in good health and wait me to back and accompany with them. I love them forever!

TABLE OF CONTENTS

LIST OF TABLES

LIST OF FIGURES

CHAPTER I

INTRODUCTION

Hybrid materials have achieved paramount accomplishments in the arena of academic and industrial world, in terms of electrochemical science,[1] catalysis,[2] energy storage,[3] biomedical[4] and environmental[5] applications. The property of hybrid materials do not only simply merge inherent physical and/or chemical characteristics of individual components into a balanced intermediate, but also aim to create the synergetic effect by the presence of a very large hybrid interface.[6-8] Briefly, hybrid materials are a result of chemically constituting of different components with the formation of interactions via 1) weak chemical bonds, including van der Waals, hydrogen bonds, or electrostatic bonds; 2) strongly coupling effect, such as covalent or ionic covalent bonds.[4] Indeed, improving the health and well-being of world's increasing population are grand challenges in the near future for our society; and one of technological solutions is enabling personalized medical treatments.[1] Thereby, new innovative materials with multifunctionality which contribute to complementary features for miniaturized and hybridized robust electronic devices would open up entirely new horizons in advanced materials research community.[9]

Carbon based hybrid nanomaterials have attracted enormous attention in electronic device and electrochemical electrode materials composition, owing to their versatile merits for good electronic conductivity, natural abundance and strong mechanical properties.[1, 10, 11] In addition, it is noteworthy to allotropic forms of nanocarbon, such as graphene,[12] carbon nanotubes (CNTs)[13] and carbon nanofibers (CNFs)[14] are very interesting materials offering scientific and technological possibilities for research, development and large-scale production. Furthermore, various physicochemical properties of nanocarbons, including thermal, electrical, thermal, electrochemical, optical and biological could be engineered into the carbon-based hybrid materials with desirable combination of functionalities. In particular, one of the many advantages present in CNTs and CNFs is the high length to width ratio (>1,000), which results in a filamentous structure translating into a high specific surface area in architecture and composition of hybrid materials.[15] To this end, this dissertation work focuses on the state-of-the-art advances of hybrid materials based on CNTs and CNFs in electrochemical science.

Immobilization of Glucose Oxidase (GOx) and Its Direct Electrochemistry. With nanomaterials engineering rapidly development in recent years, the use of natural proteins in the design of novel hybrid materials for electronic and medical purpose has emerged. To give a few examples, Abdelkader et al. shown the efficient wiring of enzymes in a conductive pure CNTs matrix for fabricating a glucose biofuel cell with excellent performance.[16] In addition, Shengyuan et al. realized a novel biosensor by immobilizing glucose oxidase (GOx) on nitrogen-doped CNTs with enhanced electron transfer (ET) for direct electrochemistry, exhibiting good biocompatibility, excellent electron-conductive network and large surface-to-volume ratio.[17] Furthermore, Muguruma et al. demonstrated the side wall of debundled SWCNTs could be plugged into the grove of FAD-GDH and realize a mediator-less direct ET, owing to the unzipping state of the low-diameter of individual SWCNTs fits specific groove position with an appropriate direction effectively.[18] Taking account into the chemical composition of protein, consisting of positively charged amino and negatively charged carboxyl, that can take part in the electrostatic effect with functionalized CNTs for hybridization. Thereby, in the Chapter II, glucose oxidase (GOx) cross-linking to a single-wall carbon nanotubes (SWCNTs)-poly(ethylenimine) (PEI) matrix is investigated using cyclic voltammetry (CV) for its direct electrochemistry and kinetics involved in the specific electrocatalytic interaction with presence of glucose. It is a key step to realize the interfacial electron transfer between the redox enzymes and electrode for enzymatic bioelectrocatalysis in various bioelectrochemical devices.[19] However, owing to electrical insulation of the redox-active site by the surrounding polypeptides, it is generally difficult to enable the efficient ET kinetics for the redox-active site and the support via merely immobilizing the enzyme onto a solid electrode surface. Basically, two classified mechanism of realizing accessibility of ET are mediated ET and direct ET. In the mediated ET, an extra mediators[20] or relay[21] are utilized to shuttle electrons between the redox-active sites and the electrode, which may bring other concerns, such as toxicity, possibility of leakage from the cells system, and a more positive redox potential required to provide the driving force.[22-24] In contrast, a direct ET system is more desirable and ideal with faster ET directly between the redox active sites within the intrinsic electron relay system of enzymes and the solid electrode. Although the use of carbon-based nanomaterials enables the direct ET of redox enzymes to carry out bioelectrocatalysis has achieved considerable efforts, the underlying role of carbon nanomaterials in interfacial ET remains unclear. In particular, understanding electrical communication between the redox enzymes and the solid electrode is of scientific significant in the exploration of the mechanism of biological redox reactions and of great practical meaningfulness in the fabrication of bioelectronic devices.[22, 25-31] Herein, two key questions are solved as following in Chapter II, including realizing sufficient ET between the redox active centers within the enzyme and the support; how the ET reaction correlates to the enzymatic or electrocatalytic activities of GOx confined at the electrode. These compelling findings may offer promise of a way to development of reagentless or mediator-free glucose sensor in state-of-the-art application.

Metal Oxides-based Nonenzymatic Sensing. With electrochemical biosensors being the first successfully commercialized biosensor technology, in particular, glucose sensors, they have gained paramount attention from the research community, owing to their versatility and cost-effective point-of-care biomolecular sensing.[32-34] Basically, glucose sensors are generally divided into two categories, namely, enzymatic and nonenzymatic.[35-37] Furthermore, the obvious advantages provided by nonenzymatic electrochemical sensors have propelled the demand of high efficient, superior sensitive and selective electrocatalysts. The earth-abundant transition metals such as Co, Mn, Fe, Cu and Ni based oxides are promising catalytic materials due to their high catalytic activity, low cost and chemical stability.[38-42] Among them, MnO_2 with different structural form (α, β, γ, δ) based on its tunnel structure, enables high surface area and high redox activity and delivers a high capacity and good catalytic performance, which make it an interesting transition metal oxide (TMO) in both electrocatalytic and energy storage application.[43-45] Additionally, cobalt oxide, with unparallel advantages of diversity of oxidation states for charge transfer and high energy density, has been considered as a promising candidate for various electrochemical application, especially, electrocatalysis and supercapacitance.[46-48] In particular, mixed valence oxides of transition metals with their superior morphological structure are a class of biofunctional electrocatalysts with substantially improved electrocatalytic activity for analyte molecular sensing.[49-51] However, TMO also have the issue of poor conductivity, restraining its broad application. Thus, the majority of strategies for improving the performance is to hybridize them with conductive carbon nanomaterials to mitigate the issue and synergically enhance the catalytic activity.[34, 51] Indeed, even very small amount of carbon nanomaterials hybridized with metal oxide could enhance the electron transfer, accelerate the reaction kinetics and suppress the aggregation of metal oxide during the formation process. Herein, the carbon support plays as a role of conductive substrate, interacting with active transition metal species via strong covalent coupling effect. In addition, the integration of metal oxides and carbon could modify the physicochemical property of both components, simultaneously, introduce new favorable active sites. In this regard, the key objectives in Chapter III are to 1) design and develop the geometry and morphology of the 3D interconnectional architecture of nanomaterials for obtaining larger surface area and engineering their interface to accelerate the charge transfer; 2) examine fundamentals of electrocatalytic principle of the carbon-based hybrid materials; 3) investigate the hybrid metal oxides-carbon electrode for its electrochemical performance in nonenzymatic sensing. Thereby, the focus of the Chapter III is to investigate a suitable heterogenous hybrid component for giving good mass transport channels and exposed active sites for electrochemical detection of biomolecules.

Nanohybrid Electrode for *in-situ* Sensing. Improving the health and wellbeing of the world's increasing population is one of the grand challenges which our society is to be faced in the near future. Besides the diabetes, another example of the grand challenge is neural disorders. It is well known that neuronal communication in the brain is highly relied on the precisely controlled neurotransmitter dynamics, those of which are used to neuron-to-neuron signaling.[1, 52] Consequently, changes in the spatial and temporal kinetics of the neurotransmitters are associated with several diseases of the brain, including Parkinson's diseases, Alzheimer's disease, schizophrenia or associated rare tumors arising in neural crest tissue.[53] Thus, the approaches in the basic research as well as in the treatments of neurological diseases are aiming to affect the turnover and the amount of the neurotransmitters in the brain, which are broadly used. Hence, accurate determination of neurotransmitter concentration variation is the key to understand the operation of treatments as well as to the development of new approaches. In recent years, the development of low-cost and non-invasive diagnostics to prompt readout for users at the point of need has concentrated in research community, in particular, electrochemical biosensors, a benchmark in the biosensor community owing to high sensitivity, relatively low cost, short response time, and compatibility with integrated circuit technology for readout.[54-56] Dopamine (DA), an important neurotransmitter belonging to the catecholamine family, plays a critical role in a number of physiological process in synaptic communication in cells.[57] Furthermore, cell-based therapy for neurological diseases has attracted much attention. PC12 cells (rat pheochromocytoma cells) are often used as a model in terms of dopamine releasing, which are stimulated by injecting highly concentrated K^+ and inducing the releasing of dopamine by exocytosis by depolarizing cells.[52, 53, 55, 56, 58-60] In particular, hybrid materials with flexible and potential miniaturization ability would be suitable for the construction of point-of-care sensors/devices and widen their applications in extreme conditions, where only small quantities of samples are available for analysis.[60] To address these needs, a sensing platform with excellent flexibility and sensitivity is highly anticipated. One dimensional electronspun carbon nanofiber (ECNFs) has emerged as a novel supporting scaffold for hybrid flexible electrode materials, owing to its extraordinary properties, such as effective electron transfer, good electrical conductivities and high surface-to-volume ratios.[61-63] Significantly, heteroatom doping into the carbon framework introduces charge redistribution. Doping of nitrogen (N) and oxygen (O) has drawn significant attention in the improvement of the specific activity and active site densities.[51, 64] Among aforementioned metal oxides, cobalt oxide nanostructures have shown a promising electrode materials for electrochemical application, including batteries, supercapacitances and electrocatalysis, owing to their merits of high theoretical capacity, highly-active catalytic properties, and outstanding thermal/ chemical stability.[51] It was reported that the supplementation of a large amount of nitrogen dopants and N-containing functional groups could offer abundant binding sites for anchoring cobalt oxides nanostructures and active sites to improve ion storage performances and/or electrocatalytic activities for detection of biomolecules.[49, 65-68] To this end, the objective of Chapter IV is to focus on the implantation of N dopant in the carbon skeleton, the investigation of growth of cobalt oxide nanostructure on ECNFs, and the performance of the electrochemical detection of DA secreted from living cells.

In summary, the theme of my dissertation research is focus on carbon-based hybrid materials for exploiting their synergetic effects between individual components in terms of their physicochemical properties and application in electrocatalytic and biosensing application. In particular, the goal of the dissertation research is to advance both the fundamental understanding and technical methods on development (design, synthesis, and testing) of novel hybrid nanomaterials emphasizing the electrocatalytic reactions at the interfaces and associated charge transfer process. The electrochemical biosensor platforms proposed in this dissertation potentially provide a solution to address one of the grand challenges that our society is facing, i.e., the point of care monitoring of the health and disease development, thus improving the health and wellbeing of the world’s increasing population.

CHAPTER II

THE GlUCOSE EFFECT ON DIRECT ELECTROCHEMISTRY AND ELECTRON TRANSFER REACTION OF GLUCOSE OXIDASE ENTRAPPED IN A CARBON NANOTUBE-POLYMER MATRIX

This chapter has been publicated as: Yin, Z., Ji, Z., Zhang, W., Taylor, W., Zeng, X., Wei, J. (2020). The Glucose Effect on Direct Electrochemistry and Electron Transfer Reaction of Glucose Oxidase Entrapped in a Carbon Nanotube-Polymer Matrix, 2020, 5, 12224-12231.

Introduction

Understanding of electrical communication between an electrode and immobilized redox enzymes is of scientific significance in the exploration of the mechanism of biological redox reactions and of great practical meaningfulness in the fabrication of bioelectronic devices.[22, 25-31] In particular, the direct electrochemistry of electroactive enzymes is a critical reaction for developments of mediatorless electrochemical devices for sensing and energy conversion.[23, 69] Glucose oxidase (GOx), as a type of homodimeric flavin protein, consisting of two noncovalently symmetric bound flavin adenine dinucleotide (FAD), plays an important role in catalyzing the oxidation of β-D-glucose.[70, 71] It is generally difficult to obtain direct electron transfer (ET) between the GOx and a conventional bare electrode, due to the fact that the redox active FADs, the cofactors of GOx, are deeply embedded within an electrically well-insulated protein shells.[31, 72] The distance is around 15 Å from the enzyme surface,[73] which exceeds the critical electron-tunneling distance.[25, 28] In bioelectronic devices, enzymes are usually immobilized on an electrode surface, however, the efficient ET between the active redox centers and the electrodes is limited by electron-tunneling distance within the protein and microenvironment.[74-77] Therefore, considerable efforts have been employed to alleviate the inaccessibility of ET between cofactors and electrodes via redox mediators[20] or relays,[21, 78] metal nanoparticles,[30, 79] and nanocomposite matrix[80, 81] to facilitate the ET. However, mediators or relays to shuttle electrons between the redox active centers and electrodes may bring other concerns such as toxicity, possibility of leakage from the cell system, a more positive redox potential required to provide the drive force for the mediated ET.[22-24] Hence, a mediator-less approach for ET of enzymes has attracted enormous attention. Publications suggest that realizing the ET between an electrode and immobilized GOx can help to eliminate the concerns regarding the oxygen deficiency in the absence of mediators in applications for glucose biosensors and biofuel cells.[16, 82-84]

Although there is a debate towards rationalizing the occurrence of direct ET of GOx,[85] more reported that the electrical communication of GOx could be enhanced by conductive nanomaterials. To this end, various conductive nanomaterials, including carbon nanotubes (CNTs), graphenes and gold nanoparticles (NPs), have been extensively used to promote the ET of immobilized GOx. An intensive research focus is to use carbon nanomaterials to facilitate the ET between the electrode and the immobilized proteins due to its unique chemical, physical, and electrical properties. Conductive carbon nanomaterials may effectively shorten the electron-tunnelling distance and thus provide an electron-mediating function.[18, 25, 27, 86] Among these carbonaceous nanomaterials, carbon nanotubes (CNTs) have received marvellous attentions acting as ET media and/or supporting matrix for the immobilization of enzymes owing to their superior electric conductivity,[24] high chemical stability, remarkable mechanical properties,[84] biocompatibility[87] and large surface area.[88] The enzyme-immobilized CNTs to promote the ET has been reported in connection with various biomolecules.[18, 25, 89] Baughman et^^al. showed that the tubular fibrils of SWCNTs could be positioned within the tunnelling distance of the active redox cofactor of the enzyme, facilitating the transfer of electron with little consequence to denaturation.[90] Muguruma et al. speculated the side wall of debundled SWCNT could be plugged into the grove of FAD-GDH, because the unzipping state of the low-diameter individual SWCNT fits specific groove positions with an appropriate direction effectively.[18] CNTs have also been widely applied as an excellent electron-media supports for direct ET of GOx and the electrodes to develop a mediator-free glucose sensor.[17, 91] San et al. reported that the number of walls of CNTs has the effects of quantum properties on the direct ET and electrocatalytic activity of GOx towards glucose oxidation.[92] Simonov et al. suggested that different population of defect and functional groups on CNTs immobilized with GOx result in the ET process gated by conformational changes of the cofactors.[93] Zhao et al. observed that the reduction in the amount of α-helix caused the conformational changes of GOx upon adsorption at the CNTs, leading a less shield GOx active sites and decreased the resistance of the direct ET between GOx and the CNTs-modified electrode surface.[94]

In the past decades, some researches claim that the GOx with direct ET possesses electrocatalytic property for glucose oxidation evident by the anodic current increase with the addition of glucose at the absence of oxygen;[25, 71, 79] Some indicate that surface confined GOx undertakes direct ET in the absence glucose but forfeitures direct ET with presence of glucose, but the GOx exhibits enzymatic activity towards glucose oxidation with mediators.[95, 96] Apparently, how the ET reaction correlates to the enzymatic or electrocatalytic activities of GOx confined at the electrode is inadequately addressed. Furthermore, rare reports focus on the ET kinetics with the presence of glucose.

Herein, based on previous work on GOx captured by a SWCNT-poly(ethylenimine)(PEI) matrix,[97] we further investigated the direct electrochemistry of GOx with presence of different glucose concentrations. It was found that the Faradaic current of the bound flavin cofactor (FAD/$FADH_2$) of the GOx is suppressed by addition of glucose, but the ET rate constant of the GOx shows a monotonic increment with the concentration increase of glucose in a mediator-free condition. Control experiments using sucrose for the GOx electrode or pure FAD immobilized electrode with presence of glucose confirm that the responses to glucose is arising from the immobilized GOx. Experiments of the electrode in a mediated glucose oxidation suggest the essential intactness of GOx for enzymatic activity. The correlation of the GOx ET rate constant and Faradaic current changes as a function of glucose concentration is reported. The results are rationalized by a mechanistic process of the ET reaction associated with presence of glucose.

Materials and Methods

Solution Preparation

The COOH functionalized SWCNTs were dispersed in DMF solvent with a concentration of 1mg/ml and then ultrasonicated for 30 min to form a stable CNT suspension. 1mg/ml poly(ethylenimine) (PEI) solution was obtained by diluted it in deionized water. A certain amount of chitosan was used for adding into 1.0 % (wt %) acetic acid with ultrasonication until it was transparent and homogeneous, and then the chit-acetic solution of 0.5 % (w/v) was obtained, which was used as a protective biomembrane for protein. After that, 60% (w/w) polytetrafluoroethylene (PTFE) was diluted into the chit-acetic solution to form 2.0% (w/w) liquid sealant. This solution was used to protect the GOx captured in SWCNT-polymer matrix. The stock solution of glucose was prepared in 0.02 M phosphate buffer saline (PBS) containing 0.1 M KCl (pH 7.4). The stock solution was stored at room temperature overnight to ensure the mutarotation of glucose and equilibrate the α- and β-D-glucose form before the usage. All other chemicals of analytical grade were employed for the experiment without further purification.

Electrode Preparation

Figure 2.1 shows the preparation of the GOx captured in a SWCNT-polymer matrix. The 3 mm diameter glassy carbon electrode (GCE) was carefully polished with 1.0, 0.3 and 0.05 μm micro-polishing powder sequentially, followed by ultrasonication in deionized water for several minutes. The cleaned GC electrode was dried in ambient environment. The PTFE/GOx/PEI/CNTs/GCE system was fabricated with layer-by-layer process with slight modification of previously reported procedure.[97] Free FAD replaced GOx for preparing the control electrode. Briefly, 1 µl of SWCNTs suspensions was dropped onto the polished GCE and dried completely in a cleaned oven at 45°C. We performed different SWCNTs loading volumes ranging from 0.6 µl to 3.6 µl and found that 1.0 µl of the SWCNTs suspensions showed the best electrochemical signal in cyclic voltammetry and collections of data for direct ET of GOx immobilized onto the nanostructured matrix. Therefore, further electrochemical studies were based on the electrode modified with a fixed loading volume (1 µl) of SWCNTs suspensions if not specified. The SWCNTs/GCE was then soaked in a 1 M NaOH solution for 5 min to introduce more negative charges and rinsed with DI water. After introducing negative charges, the electrode was incubated in 1 mg/ml poly(ethylenimine) (PEI) aqueous solution for 10 min to self-assemble the positive charged polymer to the electrode, and then the PEI/SWCNTs/GCE was rinsed with DI water, allowing the solvent to evaporate at room temperature. Then, drop-casting 10 µl of freshly prepared 10 mg/ml GOx (50 mM HEPES, 0.5 mM EDC/NHS) onto the surface of PEI/SWCNTs/GC electrode and dried at 4°C. Before use, a 5 µl volume of the PTFE dispersion (2%(w/w)) was spread onto the surface of the GOx/PEI/SWCNTs/GC electrode as a binder to hold the film on the surface stably. Note that the GOx molecules were immobilized by covalent bond to the CNT/PEI matrix and the PTFE was used for the film stability. After that, the PTFE/GOx/PEI/SWCNTs/GCE system was placed at 4°C until the solvent was evaporated. All working electrodes were stored under dark at 4°C if not use.

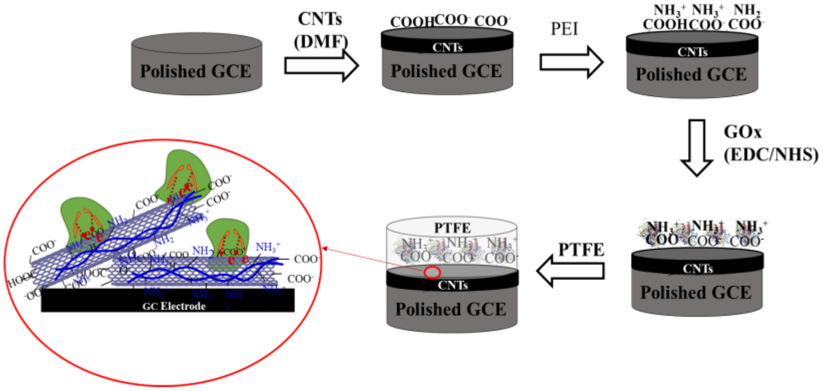

Figure 2.1 A Schematic Illustration of Preparation of Enzyme-Nanomatrix system: Illustration of a protocol for the layer-by-layer fabrication process and GOx immobilization on the nanocomposite PTFE/PEI/SWCNTs/GCE system and a schematic of the nanomatrix system for the electrochemical electron transfer study of the immobilized GOx (not in actual scale ratio)

Electrochemistry Study

Cyclic Voltammetry (CV) was performed using a Bio-Logic VMP3 electrochemical workstation with a conventional three-electrode cell which was composed of an Ag/AgCl reference electrode (3 M KCl), a platinum wire counter electrode and the PTFE/GOx/PEI/CNTs/GCE or PTFE/FAD/PEI/CNTs/GCE as a working electrode. The electrochemical measurements were performed in a nitrogen-saturated high ionic strength supporting solution of 0.02 M PBS (pH 7.4) containing 0.1 M KCl. The electrolyte solutions were deoxygenated by high purity of nitrogen for at least 15 min and N_2 was kept following over the solution during electrochemical measurement. Each working electrode was incubated in the electrolyte solution for at least 10 min before the data collection to stabilize the electrode and allow the dissociation of the loosely adsorbed enzymes from the surface of the electrode. In addition, a tough washing process was employed to washed out some free FAD of GOx modified electrodes. CV measurements were performed in 0.02 M PBS (pH 7.4) containing 0.1 M KCl incubated with different concentrations of glucose at room temperature under a nitrogen environment at scan rates of 50, 100, 150, 200, 300, 400, and 500 mV s^{-1}. Each electrochemical experiment was repeated at least three times, and the average data are presented.

The Calculation for Active GOx in ET at Electrode Surfaces

The redox couple (GOx(FAD)/GOx($FADH_2$)) is immobilized on the electrode surface, therefore, the peak current is determined by the redox reaction of active GOx and given by:[98]

$$I_p = n^2F^2/4RT * vN \qquad (2\text{-}1)$$

where n is the number of electrons transferred, F is Faraday's constant, R is the gas constant, T is the temperature in Kalvin (298K), v is the voltage scan rate and N represents the number of redox active sites on the electrode in mol.

Methods for Electron Transfer Rate Calculation

The ET rate constant k^0 of the immobilized GOx was calculated using two different methods: the extended Marcus theory[99, 100] and Laviron model[101, 102] for surface confined redox species.

Marcus Method for Electron Transfer Rate Constant

To adequate understanding the ET process within the GOx, in generally, it requires to accurately determine a series of parameters, the standard rate constant, k^0, reorganization Gibbs free energy, λ_0, and the electronic coupling, V_{AB}, etc. Therefore, the

CV data-processing algorithm based on the extended Marcus theory, developed by Weber and Creager[99] and Murray et al.[100], as the most straightforward and advanced method, is used for determining k^0 and λ_0 in this work.

The electron transfer between the immobilized, the electrochemical reporter, such as GOx, and an electrode can be written as follows by assuming the ET reaction is the dominant pathway,[103]

$$GOx(FAD) \xleftrightarrow[k_{red}]{k_{ox}} Electrode \quad \text{.......} (2\text{-}2)$$

where the ET reaction can be express as:

$$GOx(FAD) + 2e + 2H^+ \leftrightarrow GOx(FADH_2) \quad \text{.......} (2\text{-}3)$$

It is worth to mention that the reorganization Gibbs free energy of the reaction above can be easily changed by the overpotential (η). Therefore, the electron transfer rate constants are impacted by the overpotential. In brief, the moderate ET rate constants occur at nearly zero driving force, that is around zero overpotential conditions in ET processes, which is ascribed to lower the Gibbs energy barrier, that is, actually effective reorganization free energy, owing to obtaining the slowest conformational reorganizable degrees of freedom modes. On the basis of the extended Marcus theory for heterogeneous electron transfer, the standard heterogeneous rate constants (k^0), that is, the rate constant obtained at $\eta = 0$, which can be expressed as:[104]

$$k^0 = 2\pi/\hbar * |H_{DA}|^2/\sqrt{(4\pi\lambda k_B T)} * \int_{-\infty}^{\infty} \rho(\varepsilon) f(\varepsilon) \exp\left(-(\lambda+(\varepsilon_F-\varepsilon))^2/4\lambda k_B T\right) d\varepsilon \quad \text{..........} (2\text{-}4)$$

in which, ħ is the Planck constant, H_{DA} is the effective electronic coupling between the electrode and the redox probe states, λ is the reorganization energy, k_B is Boltzmann's constant, T is temperature in Kalvin, $\rho(\varepsilon)$ is the electronic density of states of the electrode, $f(\varepsilon)$ is Fermi function, ε_F is the Fermi energy, and ε is the energy of an electronic state in the electrode.

The application of this algorithm to the fitting of the Faradaic peak potential shifts from the formal potential as a function of the scan rate, log(υ), was used to obtain k^0 values[105] for the electron transfer rate constant of the entities GOx immobilized on the composite nanostructured electrode.

Laviron Method for Electron Transfer Rate Constant

The electrochemical electron transfer kinetics was also analyzed by classic Laviron Method based on the conventional Butler-Volmer approach, based on the analysis of peak-to-peak separation potential position as a function of the scan rate (ν),[101, 102] then the electron transfer constant is given by:

$$k^0 = (1-\alpha) * nF\nu_i/RT \qquad \text{(2-5)}$$

where α represents the transfer coefficient, ideally, α equals to 0.5 for all overpotentials, and ν_i represents the x-intercept of the linear ranges in the plot of peak potential shift vs. log (ν).

Results and Discussion

The representative cyclic voltammograms (CVs) of the PTFE/GOx/PEI/CNTs/GCE are shown in Figure 2.2A. A pair of well-defined and nearly symmetrical redox peaks presents in the CVs of the PTFE/GOx/PEI/CNTs modified GC electrodes. The formal potential at about -0.45 V vs. Ag/AgCl electrode is consistent with the Nernstian dependence, a good agreement to other reports for direct ET of GOx.[25, 26, 28, 82, 92] The redox peaks indicate the cofactors of GOx undergo a reversible ET on the nano-matrix modified electrode without the assistance of any ET mediators. The intactness of GOx was verified by its electrocatalytic activity towards glucose oxidation (vide infra).[97] No obvious anodic or cathodic peaks were observed in the CVs of GOx/GCE, CNTs/GCE and PEI/CNTs/GCE (Fig. S2.1). However, the non-faradaic charging currents in CVs of the CNTs/GCE and However, the non-faradaic charging currents in CVs of the CNTs/GCE and PEI/CNTs/GCE were significantly enhanced comparing to the bare GCE caused by their double layer capacitance, owing to increased effective surface areas of the CNTs matrix. The PEI/CNTs/GCE displays a slight increase of the non-Faradaic charging current compared to the CNTs/GCE, suggesting a minor contribution in the effective reaction surface area from polymer PEI. Both GOx/PEI/CNTs/GCE and PTFE/GOx/PEI/CNTs/GCE yielded redox peak pairs, indicating the GOx entities were active and immobilized successfully in the matrix and involved in the direct ET at the nano-matrix electrode. The presence of carboxyl groups and л-л conjugated systems of the nano-matrix favor the potential orientation of GOx absorbed onto the CNTs-matrix for the interface ET reaction.[89, 92] The film of PTFE plays a role to fix the modifier on the electrode and protect the nanostructured composite from dropping. The redox peak decreases slightly.

The strength of association and stability of the entrapped GOx were assessed by normalizing the peak current of CVs with time. The peak current is proportional to the amount of GOx immobilized on the electrode. In the procedure, the modified electrode was placed in the electrolyte solution, CVs were initiated at a scan rate of 50 mVs^{-1} at subsequent intervals. Figure 2.2B shows a profile of the normalized peak current as a function of time, indicating the good stability of the immobilized GOx at the nanomatrix-modified electrode. In addition, according to a comparison of the reduction of peak current with or without glucose (Fig. S2.2), one could conclude that the large decrease of peak current is ascribed to the involvement of glucose instead of the instability of the electrode.

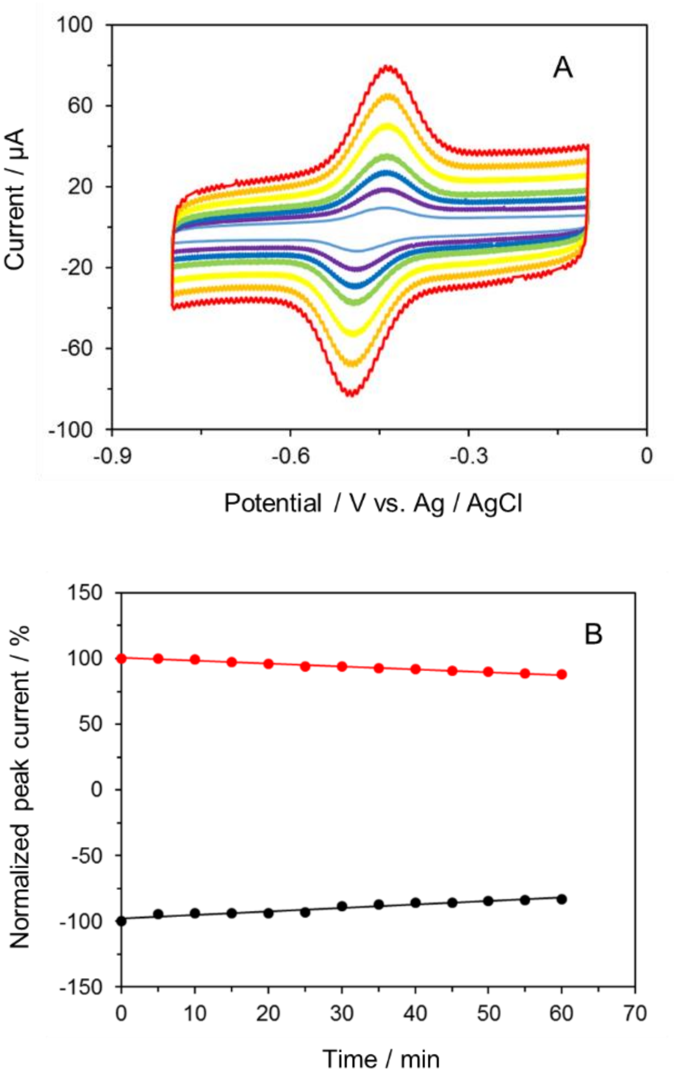

Figure 2.2 Cyclic Voltammograms and Stability Profile: (A) Representative cyclic voltammograms (CVs) for PTFE/GOx/PEI/CNTs/GCE in a nitrogen-saturated 0.02 M phosphate-buffer saline (PBS) with 0.1 M KCl at pH 7.40 in the absence of glucose. Note that the scan rates are 50, 100, 150, 200, 300, 400, and 500 mV s-1, respectively. (B) The peak current profile vs. time at a scan rate of 50 mV s-1 in the absence of glucose.

The reversible direct electrochemistry of GOx on the nano-matrix modified electrode was investigated in the absence and presence of glucose under nitrogen-saturated environment. Figure 2.3A shows typical CVs of the GOx at different glucose concentration up to 70 mM. In cyclic voltammetry, the peak current ip, displayed as a function of the voltage scan rate for the electrode modified with the GOx embedded in the nanostructured composite at different concentrations of glucose. Hence a series of scan rates were performed for the GOx electrode at each glucose concentration. The i_p was found to exhibit a linear dependence on the scan rate under the same solution condition (Fig. S2.3, Figure 2.3B). With the increase of scan rates, the anodic peak potentials shift positively, whereas the cathodic peaks shift towards negative potential. The peak current linearly increases with scan rates, demonstrating the redox reaction of $FAD/FADH_2$ of the GOx captured in the SWCNT matrix is a typical surface-confined process, rather than a diffusion-controlled process with the scan rates.[97] Moreover, the immobilized GOx shows excellent recovery after the running electrochemistry in glucose. Figure 2.3C displays CVs of the electrode before and after running CVs in 20 mM glucose solution. The magnitude of the peak current maintains almost identical before and after recovery running CVs in glucose.

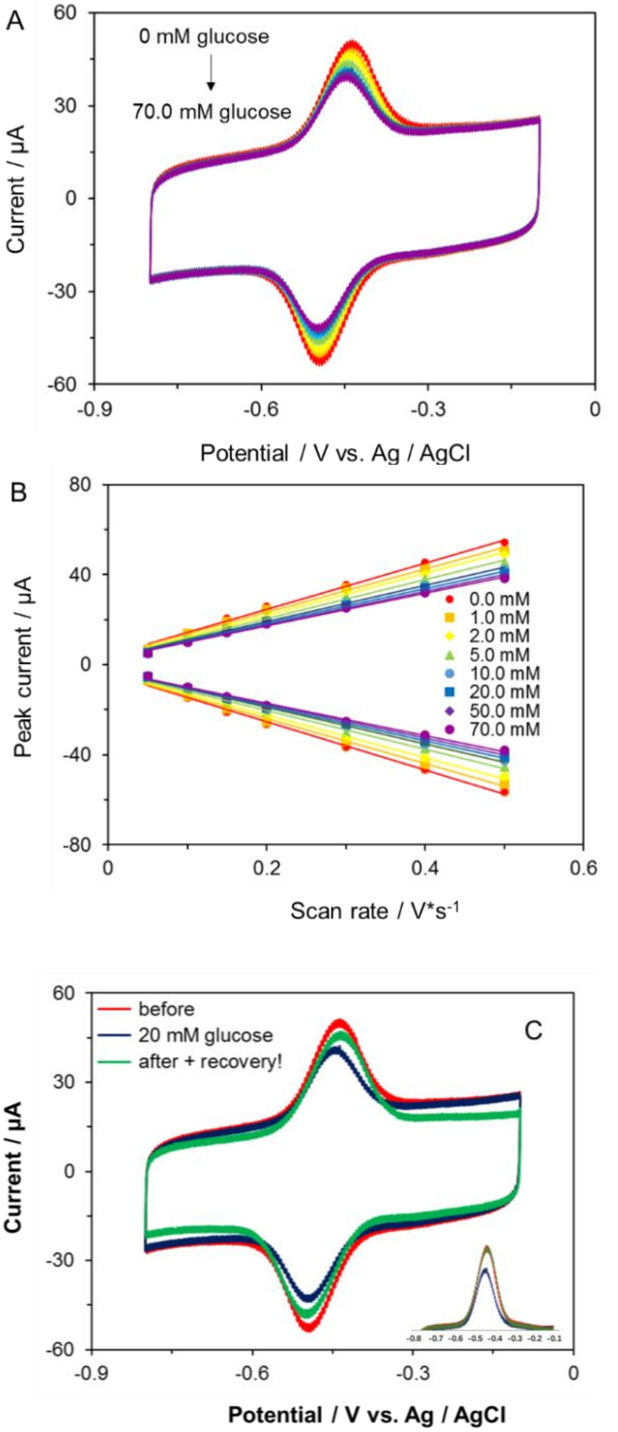

Figure 2.3 Kinetcis Direct Electrochemcial Tests: (A) Representative cyclic voltammogram for the glassy carbon electrode modified with PTFE/GOx/PEI/CNTs at the scan rate of 300 mV s-1 under different concentrations of glucose. (B) The linear dependence of the peak current on the voltage scan rate under different concentrations of

glucose. (C) The CVs of the electrode with presence of 20 mM glucose and before/after running in glucose with absence of glucose (the insert shows the oxidation peaks after subtracting the baseline background, full spectrum see Fig. S2.4).

The effect of glucose on the ET of GOx was performed by cyclic voltammetry at the presence of different concentration of glucose in solution. The CVs at the same scan rate (300 or 50 mV/s) for the PTFE/GOx/PEI/CNTs/GCE (Figure 2.3A and Fig. S2.5) demonstrate a correlation of the ET reaction of GOx to the glucose concentration. When the glucose concentration increases, both the magnitude of CVs' peak current and the separation of anodic and cathodic peak position decrease. According to these observations, in the case of the presence of glucose, two possible reactions are proposed occurring at the electrode, which are:

$GOx(FADH_2) \leftrightarrow GOx(FAD) + 2H^+ + 2e$..(2-6)

$G + GOx(FAD) \rightarrow GOx(FAD) \cdot G \rightarrow GOx(FADH_2) \cdot P \rightarrow GOx(FADH_2) + P$.................(2-7)

where $FADH_2$ and FAD are the reduced and oxidized forms of the GOx redox center, respectively; G is β-D-glucose and P is the product of glucose oxidation, i.e. D-glucono-1,5-lactone. Eq. (2-6) represents a quasi-simultaneous proton-coupled two-electron transfer reaction of the GOx captured in the nanocomposite electrode; and the nonadiabatic ET reaction mechanism is well-characterized in a previous report.[97] The distinct single pair of anodic and cathodic Faradaic peaks around formal potential –0.45 V vs. Ag/AgCl (Figure 2.3A) can be attributed to the chemically reversible concerted two-electron process.[93, 106] The Eq. (2-7) demonstrates the glucose oxidation at the electrode surface which is a typical cyclic enzyme catalyzed glucose oxidation process, including the diffusion of G to enzyme for a GOx(FAD)·G complex, conversion of G to P, and then departure of P from GOx.[82] The intermediate complexes engaging FAD and glucose have been directly observed and identified by mass spectroscopy; and the complexes are responsible for the cyclic coenzyme conversion of FAD and glucose oxidation.[107] Such complexes are formed through weak electronic affinity, introducing nucleophile of glucose into the reactive sites GOx; and the FAD reduction and glucose oxidation occurred subsequently with the help of some amino acid residues, e.g. His, Trp and Tyr near the surface of GOx.[108, 109] It should be noted that the stability of GOx and intermediates of the FAD-glucose could be impacted by local pH value during the glucose oxidation because of the electrostatic effect.[110] Lower pH would decrease the activity of GOx.

The results and analysis suggest that some bound redox active centers (FADs) of GOx at the electrode are directly involved in the oxidative reaction of glucose. As the concentrations of glucose increases, more GOx(FAD)s undertake the enzymatic catalysis of glucose oxidation, increasingly converting to GOx($FADH_2$), therefore, the amount of GOx (FAD) for the direct electrochemistry decreased, leading to both the cathodic and anodic peak currents decrease continuously. It seems there is a competition of the GOx between direct ET and the enzymatic catalysis of glucose oxidation, because, if GOx($FADH_2$) generated in Eq. (2-7) participates to the ET reaction, the oxidation peak current in Eq. (2-6) should increase, which is not observed in this case. In other words, once a GOx molecule participates the enzymatic oxidation of glucose, then the GOx does not undertake the direct electrochemical reaction (deactivated in direct ET reaction).

To confirm the responses are resultant from the enzymatic oxidation of glucose by GOx, rather than any contaminated free FAD, or non-specific sugar effect to the electrode, two control experiments were performed. One control experiment was conducted using a pure FAD immobilized nano-matrix electrode. Figure 2.4A exhibits a pair of redox peaks with a formal potential around - 0.39 V vs. Ag/AgCl from the FAD, however the Faradaic peaks do not vary with the addition of 70 mM glucose. Although bound GOx and free FAD could show almost similar characteristic redox peak pair for the CVs, the electrochemistry of free FAD doesn’t show any impact by 70 mM glucose. The other experiment was performed using the PTFE/GOx/PEI/CNTs/GCE with a nonspecific sugar, sucrose at 70 mM. Figure 2.4B shows no changes of the redox pair of bound FAD of GOx before and after addition of sucrose. These results are strong evidences to support that the decrease of peak current from the direct ET of GOx on the electrode is ascribed to the presence of glucose and plausible enzymatic oxidation by GOx at the electrode.

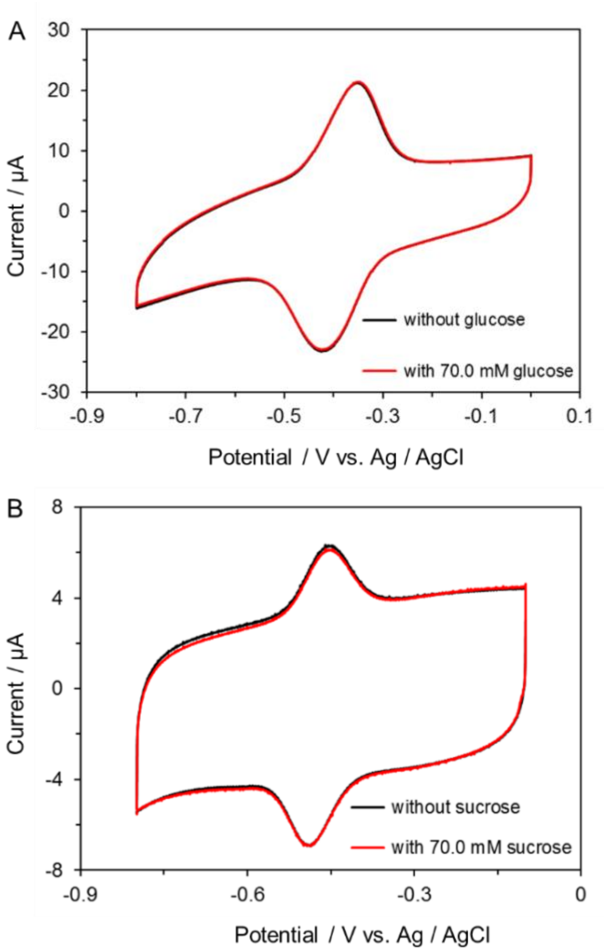

Figure 2.4 Control Experimental Tests: (A) Cyclic voltammogram profile of the effect of glucose on the free radical of flavin adenine dinucleotide (FAD) immobilized electrode, PTFE/FAD/PEI/CNTs modified GC electrode. (B). Cyclic Voltammograms of examining the effect of non-specific substrate (sucrose) on the PTFE/GOx/PEI/CNTs modified GC electrode. Scan at 50 mV/s.

To further examine the electrocatalytic activity of the PTFE/GOx/PEI/CNTs/GCE with presence of glucose, the CVs of the electrode in mediator hydroquinone (HQ) solution were performed. The electrochemical oxidation of glucose was studied by adding different concentrations glucose in the electrochemical cell containing 1 mM HQ as the ET mediator under a nitrogen-saturated condition. The cyclic voltammetry covers the potential window for both the direct electrochemistry of GOx and HQ mediated glucose oxidation. Figure 2.5 shows the active electrocatalytic reaction of the PTFE/GOx/PEI/SWCNT/GCE electrode, which demonstrates increase of the anodic peak currents of HQ with the addition of glucose, indicating an electrocatalytic current for the oxidation of glucose. Meanwhile, the direct electrochemistry of GOx was observed and presented a similar change to Figure 2.3A at the presence of glucose without HQ. Namely, the increase of glucose in the solution, the Faradaic current of GOx decreases, and the peak separation becomes smaller, suggesting a faster ET reaction of the immobilized GOx.[97, 98] The coincidence of the two cases confirms that, once a GOx undergoes catalyzing glucose oxidation by either the enzymatic or the electrocatalytic process, it may not participate to the direct electrochemistry reaction.

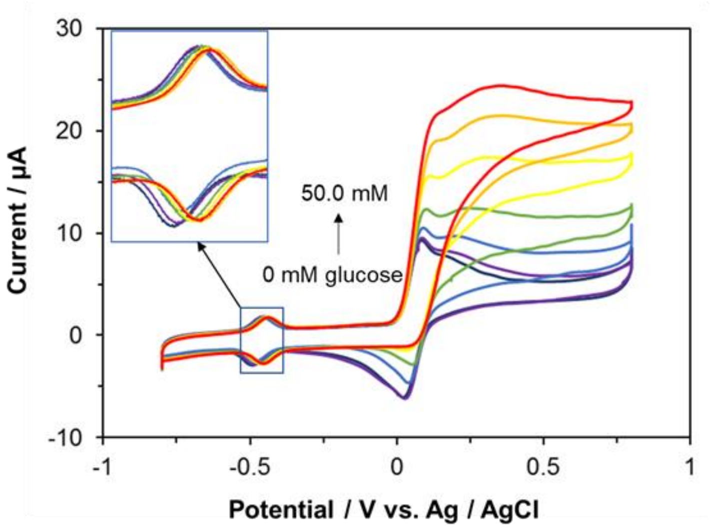

Figure 2.5. Mediated Electrochemcical Kinetics Test: CVs for the PTFE/GOx/PEI/SWCNT/GCE with addition of 1mM hydroquinone as electron-transfer mediator under a nitrogen-saturated electrolyte solution with different concentrations of glucose. pH 7.4, at scan rate of 10 mV*s^{-1}. Inset is the enlarged CVs of GOx reactions.

It would be of significance to examine how the ET rate constant and magnitude of peak current of GOx correlate to the glucose concentration. The CVs (Fig. S2.3) of the PTFE/GOx/PEI/CNTs/GCE were obtained at presence of different concentration of glucose at scan rates from 50 to 500 mV/s. This scan rate range warrants the ET kinetic control rather than a proton diffusion control.[97] First, the amount of the GOx involved in direct ET at the PTFE/GOx/PEI/CNTs/GCE was determined by the linear dependence (Eq. (2-1) in Method section) of the peak current on the voltage scan rate (Figure 2.3B). Using n=2, the amount of electroactive GOx of ~ 2.89×10^{-11}, 2.68×10^{-11}, 2.55×10^{-11}, 2.27×10^{-11}, 2.15×10^{-11}, 2.04×10^{-11}, 2.01×10^{-11}, and 1.99×10^{-11} mol are obtained with a decrease trend under glucose concentrations of 0.0, 1.0, 2.0, 5.0, 10.0, 20.0, 50.0, and 70.0 mM, respectively. According to the amount changes and Eq. (2-6)~(2-7), one may conclude that about 0.9×10^{-11} mol GOx (31 %) from the electrode participates the enzymatic catalysis of glucose oxidation at the 70.0 mM glucose solution.

The ET between the GOx and the modified electrode can be assumed that the CNTs may “safely” penetrate into the central interior part of GOx, providing a “wired” ET of the FADs residing inside GOx while not significantly denaturing the protein.[18, 90, 97] The dependence of the redox peak potentials on the voltage scan rate can be employed to calculate the ET rate constant.[98] Figure 2.6 shows the corresponding plot of the peak potential shift from the apparent formal potential versus the voltage scan rate under different concentrations of glucose. The simulation results along with the best fit for the ET rate constant were obtained by the Marcus model for immobilized redox species at reorganization energy (λ) values of 0.3, 0.5, and 0.8^^eV,[111, 112] respectively. For the rate constant calculation, the contribution of iR drop was compensated by following our previously reported method.[97, 98] The obtained ET rate constant is not very sensitive to the value of the reorganization energy, owing to the CV data do not extend to high overpotentials. Meanwhile, the ET rate constant was obtained by the Laviron method for a comparison. With a reorganization energy of 0.3 eV, in the absence of glucose, the standard heterogeneous ET rate constant (k^0) for the PTFE/GOx/PEI/CNTs/GCE system is calculated to be about 3.74 s^{-1}. In the presence of glucose, the k^0 increases by approximately 5.6 %, 13.9 %, 26.2 %, 35.3 %, 41.7 %, 42.5 %, and 43.9 % at the glucose concentrations of 1.0, 2.0, 5.0, 10.0, 20.0, 50.0, and 70 mM, respectively.

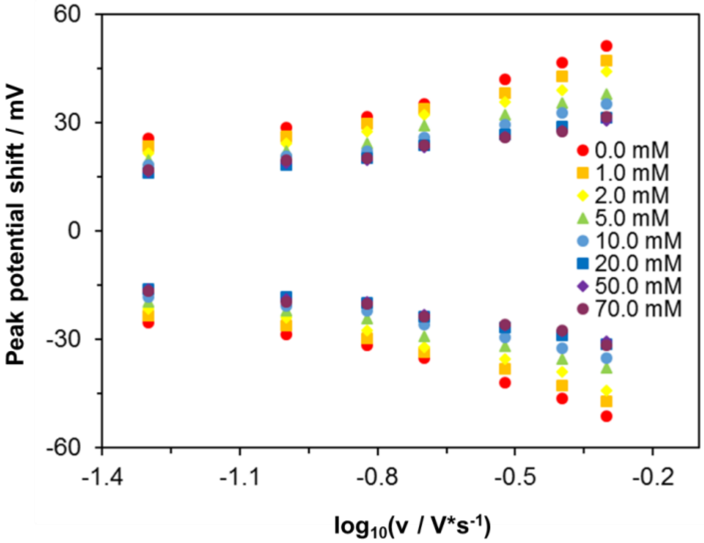

Figure 2.6 Electron Transfer Rate Constant (k^0) Calculation Profile: the dependence of the peak potential shift on the scan rate under different concentrations of glucose.

Table S2.1 shows a summary of ET rate constant obtained with and without presence of glucose. The rate constant k^0 results from the two models demonstrate similar trend to the change of glucose concentration; i.e. higher glucose concentration results in less GOx in measurable effective redox reaction and faster ET rate constant. One may concern that the addition of glucose increases the viscosity of the solution thus decrease the k^0 due to solvent friction.[112] However, in this study the addition of glucose results faster ET reaction, the viscosity effect is very minor because of the low concentration of glucose. Moreover, experiments with absence of glucose performed before and after a series of glucose concentrations to the electrode show that the peak current and the ET rate constant almost 100 % recovered (Fig. S2.6, Fig. S2.7, Table S2.1). These results further confirm that effect of glucose on the direct electrochemistry and the ET reaction of GOx.

The promotion of CNTs for the ET between the redox centers of GOx and the GC electrodes without ET mediators is convinced that CNTs were exploited as the electrode extensions. The putative penetration of CNTs' free segments into the protein's operational channel potentially provides their access to the active sites, permitting the ET to the adsorbed enzyme.[18, 90, 97] Furthermore, the nanocomposite matrix enriched by respective carboxylate and amine charged groups potentially provides excellent sliding ability for such a penetration by taking into account GOx structures.[113-115] The ET distance between the GOx active site and the GCE varies with the distribution of GOx and conformational structure of CNTs on the surfaces of electrode. Figure 2.7 schematically shows the GOx immobilization in the CNT-polymer matrix as an instance of the ET reaction scenario. First, the ET to the CNT and then to the GC electrode through the CNT/PEI matrix. The ET distances of individual GOx to the CNT and GC electrode are different depending on how depth the SWCNTs penetrate into the protein and the location of the GOx in the matrix. In general, the GOx closer to the GCE surface would have shorter pathway for the ET. Moreover, the glucose diffusions to the interface of the nanomatrix and the catalytic oxidation perturbates the solvent relaxation modes. Both of which contribute to the electronic coupling strength and reorganization energy, hence causing the GOx electrode in ET process nonergodicity,[116] i.e. the activation energy may vary individually for active GOx. The outmost layer GOx, which are accessible by the diffusion of glucose, would have the longer ET transfer distance as well as the large solvent conformational change. The ET rate constant would be slower than the GOx of the inner layer for ET process. Considering the measured ET rate constant is the ensemble of all GOx involved in cyclic voltammetry, the addition of glucose results in exclusion of outer layer GOx in electrochemically measurable ET reactions. Consequently, the faster ET rate constant from the inner layer GOx is obtained. The simultaneously reduced magnitude of the peak current is a manifestation of the less amount of active GOx in the direct electrochemistry by cyclic voltammetry.

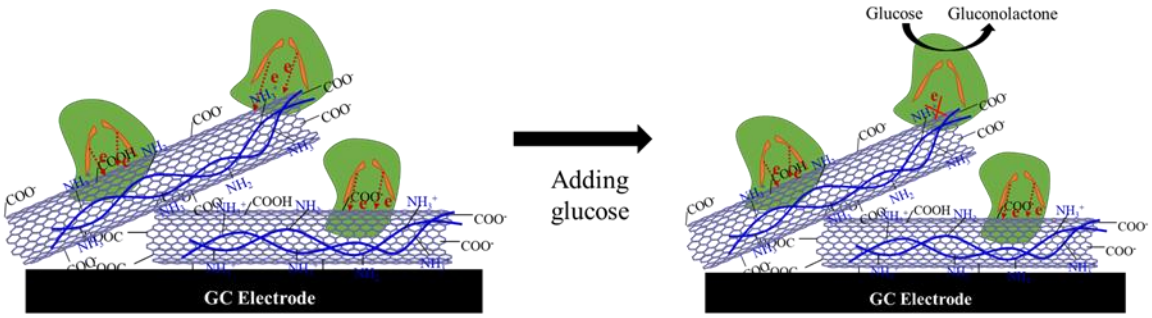

Figure 2.7 A Schematic Illustration of Electron Transfer and Enzymatic Kinetics: schematic illustration of the ET of GOx and enzymatic activity of GOx immobilized on the nanocomposite electrode.

Recently, both experimental and theoretical studies support the direct charge transfer of GOx immobilized at electrodes. The theoretical investigation concluded the possible coexist of a multistep hopping of holes to/from the oxidized or reduced FAD through residues of aromatic amino acid and direct electron tunneling between FAD and organic semiconductor.[109] The hole transfer was experimentally studied using GOx immobilized p-type polymer semiconductors.[117] In our case, the usage of electron rich PEI (n-type) in the matrix may function as trapping sites for hole charges, leading to block of hole transport and promotion of electron transfer.[118] Hence, with the matrix of conductive CNTs and PEI in this work, the direct electrochemistry of GOx(FAD) is most likely dominated by electron tunneling pathway rather than the long range hole transfer.

Practically, it might be useful to correlate the direct electrochemistry of GOx (both the ET rate constant and Faradaic current) to glucose concentration. Figure 2.8 shows the measured Faradaic peak current and ET rate constant k^0 of GOx as a function of glucose concentration. Both the rate constant and peak current present an excellent linear dependence on the logarithmic value of glucose concentration up to 20 mM, which agrees with allosteric protein regulation of binding reaction mechanism.[119, 120] The direct electrochemistry of the outer layer GOx entrapped in the nanostructured matrix electrodes was “saturated” by increasing the glucose concentration at 50 mM. Therefore, the increasing trend for the ET rate eventually levelled off to an almost constant value, exhibiting a plateau behavior, alignment with the result previously reported by Odebunmi et al.[70] In this case, the inner layer GOx are not accessed by glucose molecules with the time scale of the cyclic voltammetry due to steric hindrance.

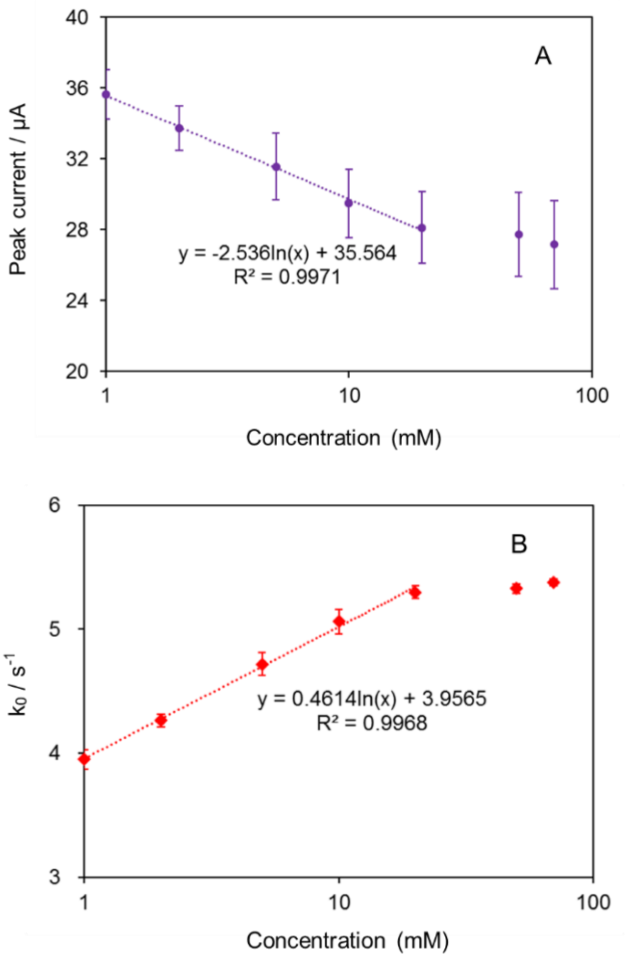

Figure 2.8 The Relationship of Faradaic Current and k^0 versus Glucose Concetration: (A) Faradaic peak current of CVs (at 300 mV s^{-1} scan rate) versus concentrations of glucose, and (B) The representative plot of ET rate constant (k^0) of PTFE/GOx/PEI/CNT/GCE as a function of the concentration of glucose. Note that the ET rate constant (k0) is calculated from the extended Marcus method with the reorganization energy of 0.3 eV.

Conclusion

In summary, the GOx captured into the nano-matrix becomes deactivated in the direct electrochemistry when it exposes the access of glucose at the electrode surface. Cyclic voltammetry studies show a significant change in the Faradaic current and peak potential shift of the CVs of GOx as a function of glucose concentration. The standard ET rate constant (k^0) was obtained by fitting the Marcus model and the Laviron method; and the rate constant (k^0) from the active GOx shows a monotonic increment with the addition of glucose. The ET mechanistic analysis suggests a scenario that the distribution of electroactive GOx sites in the electrode is non-ergodicity in terms of the immobilization microenvironment (e.^g. distance for ET pathway) and the outer layer GOx may participate in the catalyzed glucose oxidation. A shorter distance of ET and less conformational change of inner layer GOx are attributed to the faster ET rate constant. The outer GOx undertaking catalysis of glucose oxidation becomes deactivated in direct electrochemistry in cyclic voltammetry. As a result, the expressed ET rate constant increases and the Faradaic current decreases with the presence of glucoses. These results suggest that the GOx entrapped in the nanomatrix electrode may not undertake direct ET reactions and catalysis of glucose oxidation in concert. Further quantitative analysis of the relationship of ET rate constant and Faradaic current of the direct electrochemistry of the immobilized GOx indicates a strong linear relationship to logarithmic value of the present glucose concentration up to 20^^mM. This finding may offer promise of a way to the development of reagentless or mediator free glucose biosensors by measuring the direct Faradaic current of the entrapped GOx.

CHAPTER III

MINGLED MNO2 AND CO3O4 BINARY NANOSTRUCTURES ON WELL-ALIGNED ELECTROSPUN CARBON NANOFIBERS FOR NONENZYMATIC GLUCOSE OXIDATION AND SENSING

This chapter has been publicated as: Yin, Z., Allado, K., Sheardy, A., Ji, Z., Arvapalli, D., Liu, M., He, P., Zeng, X., Wei, J. (2021), Mingled MnO2 and Co3O4 binary nanostructures on well-aligned electrospun carbon nanofibers for nonenzymatic glucose oxidation and sensing, Crystal Growth & Design, 2021, 21, 1527-1539.

Introduction

Electrochemical glucose biosensors have occupied a substantial portion in current blood glucose testing, clinical diagnosis, pharmaceutical analysis and environmental monitoring owing to their rapid response, high sensitivity and selectivity, excellent stability and reproducibility. While enzymatic glucose sensors have superb sensitivity and selectivity, which also dominate major commercial market currently, they suffer from some intrinsic weaknesses including high cost, insufficient chemical and thermal stability, operating temperature limitations and short shelf lifetime. These are associated to the structure and properties of the immobilized enzymes (e.g. glucose oxidase and/or dehydrogenase), and surrounding environments, such as pH, humidity, oxygen, temperature and toxic chemicals.[33, 121] Therefore, the development of nonenzymatic glucose sensors for reliable and fast detection have received special attention to overcome aforementioned shortcomings of enzyme-based glucose sensors.

Nonenzymatic glucose sensors are generally operated by a direct electrocatalytic oxidation of glucose at an electrode surface which is modified with functional materials as a replacement of enzymes.[33] Noble metals and alloy nanoparticles have showed high electrocatalytic activity towards glucose oxidation,[121] however they still suffer from sluggish kinetics and serious deactivation due to their surface poisoning and fouling from intermediates or chloride ions adsorption.[122, 123] Herein, versatile transition metal oxides have been considered as one of the most promising catalysts for glucose detection,[124] energy storage and conversion,[125, 126] owing to their low cost, good biocompatibility and excellent electrocatalytic activity. These metal oxides that have been studied include MnO_2,[39, 43, 44] Co_3O_4,[40, 127, 128] NiO,[129, 130] and CuO,[131-133] etc. Among these non-precious metal oxide catalysts, MnO_2 has multiple crystallographic phases based on its tunnel structure,[44, 45] which is recognized an environmentally friendly electrocatalyst possessing high catalytic activity, good stability against corrosion, and abundant earth reserves.[134, 135] The Co_3O_4 based nanocomposites enjoy outstanding electrocatalytic activity and stability, because the cobalt ions possess d-band electrons exhibiting similar property with the noble metals.[40, 136] The diversiform d-orbitals in cobalt ions endow more dynamic d-electrons on the surface with highly active sites for electrocatalysis.[137] More importantly, multi-metal oxides demonstrate improved catalytic activity compared to monometallic oxides. This can be ascribed to the interfacial synergistic effect, potential complementary benefits, as well as combined compositions and structures for stabilizing an appropriate electronic configuration in high efficiency electrocatalysts.[138, 139] Recently, the Mn/Co oxide catalyst has showed its excellent electrocatalytic activity superior to single metal oxide by providing more highly active sites and charge storage properties.[134, 138] Sinha et al.[34] got a hybridized structure from 1D α-MnO_2 nanorods and Co_3O_4 nanoparticles and explored its glucose-sensing application. Their work achieved a sensitivity of 127 μA mM^{-1} cm^{-2}, a detection range of 60 μM ~ 7 mM, and the detection limit of 0.03 μM.

Even with such superior electrocatalytic activities, the intrinsic low electronic conductivity of metal oxides leads to a poor efficiency in electrocatalysis and limits the applications in electrochemistry. To overcome the drawback, some efforts have been made to construct a hybrid microelectrode which incorporates nanostructured metal oxides with high electrically conductive materials, including carbon materials,[48, 127, 140] metal-organic frameworks,[141, 142] and conducting polymers.[133, 143] Among these materials, electrospun carbon nanofibers (ECNFs) is considered to be a potentially promising candidate due to their large porosity, high conductivity and inexpensive production with freestanding nature.[144, 145] Electrospinning is a simple, efficient and scalable method, which utilized an electrical force to draw charged threads of polymer solution or polymer melt followed by thermal treatment to create porous carbon nanofibers.[146] Especially, the well-aligned ECNFs (WA-ECNFs) structure could be utilized as good scaffolds to support uniformly coated metal oxide nanostructures. Such aligned structure may shorten the distance of electron transport, therefore, enhancing the electrodeposition rate of metal oxides.[48] Besides, introducing carboxyl groups on the ECNFs surface can promote the nucleation of nanostructured metal oxides and bond well with the conductive supports.[147] Meanwhile, the ECNFs with large amounts of edge-plane-like defective sites are expected to show attractive electrocatalytic property.[148] One can expect that WA-ECNFs combined with mingled nanostructured metal oxides will provide improved conductivity and electrocatalytic activity regarding the applications in electrochemical sensing.

In this work, nanostructured MnO_2/Co_3O_4@ECNFs were synthesized by a facile one-step electrodeposition technique with a low constant current at 60 μA for 3h to co-wrap MnO_2 and Co_3O_4 onto the surface of WA-ECNFs. Such new hybrid nanocomposite electrode not only forms mesoporous surface features,[149] but renders innovations of the mingled binary metal oxides aligned to the conductive carbon nanofiber for facilitating ion diffusion and charge transfer, thus improving electrocatalytic performance.[150, 151] The fully characterized MnO_2/Co_3O_4@ECNFs were performed for the electrocatalytic oxidation of glucose and demonstrated as a superior nonenzymatic glucose sensor. Indeed, in a parallel comparative study with monometallic oxides electrodeposited onto the WA-ECNFs, i.e. the MnO_2@ECNFs and Co_3O_4@ECNFs electrodes, the results show that binary MnO_2/Co_3O_4@ECNFs electrode exhibits much better performance in terms of the electronic conductivity, large active site surface area, superb ratio of surface to volume, ion diffusion, and charge transport ability in the glucose oxidation and sensing applications. The MnO_2/Co_3O_4@ECNFs hybrid nanoelectrode was directly applied to test glucose concentration without any sonication or dissolution preparation for electrode fabrication, promising development for flexible, portable and miniaturized point-of-care medical products.

Materials and Methods

Fabrication of WA-ECNFs

The preparation of the WA-ECNFs was followed our previously reported method and process.[48, 135, 144, 152] Briefly, a self-designed sample collector consisting with four steel poles were welded on a plate to collect the ECNFs without any substrates. 10 wt.% PAN mixed in DMF solution was electrospun onto a fast-rolling collector with a rate of 2000 revolution per minute (rpm) to form the well-aligned precursors. A high positive voltage of 18 kV was applied between a syringe needle and the collector, which are located 15 cm apart from each other. The well-aligned sheets of PAN-precursor were provided at a rate of 1 mL h-1 for 5 h by using a syringe pump. The eletrospun PAN-precursor was stabilized with a heat rate of 1 °C min-1 to 280 °C and kept for 6 h in air. Later, the stabilized sheet was carbonized at a ramping rate 5 °C min-1 up to 1200 °C for 1 h in a nitrogen atmosphere to yield high mechanical strength ECNFs. The pristine WA-ECNFs could be obtained through these heat treatments.

Co-electrodeposition of Binary MnO_2/Co_3O_4 onto the WA- ECNFs

The WA-ECNFs cut into 1.5 × 1 cm^2 were used to electrodeposit MnO_2 and Co_3O_4 with a three-electrode setup, employed a charging current of 60 μA for 3 h and performed on a Bio-Logic VMP3 electrochemical workstation. We chose 60 μA for electrodeposition because higher ratio Co:Mn was obtained compare to other deposition current (e.g. 40 μA). Here, a gold electrode decorated with ECNFs, a platinum wire and Ag/AgCl (3 M KCl) were utilized as the working electrode, counter electrode and reference electrode, respectively. In order to facilitate deposition of binary MnO_2/Co_3O_4, the WA-ECNFs were pretreated with 4 M HNO_3 at 60°C for 3h to introduce carboxyl and hydroxyl functional group and to increase more active site area for nucleation of metal oxides. The supporting electrolyte solution for electrodeposition was composed of 100 mM $NaSO_4$, 10 mM $MnSO_4$ and 20 mM $CoSO_4$. After the deposition, the obtained MnO_2/Co_3O_4@ECNFs were washed with deionized water and dried at 80°C for further experiments. MnO_2@ECNFs was followed the same procedure as MnO_2/Co_3O_4@ECNFs excepting using an aqueous solution containing 10 mM $MnSO_4$ and 100 mM $NaSO_4$. Co_3O_4@ECNFs was synthesized by using 20 mM $CoSO_4$ and 100 mM $NaSO_4$ as a supporting electrolyte for electrodeposition.

Structure and Morphology Characterization

Field-emission scanning electron microscopy (FE-SEM) (Carl Zeiss Auriga-BU FIB FESEM Microscope) at an accelerating voltage of 5.0 kV and transmission electron microscopy (TEM) (Carl Zeiss Libra 120 PLUS) were performed to study the morphological features of the well-aligned ECNFs and metal oxide nanostructured on the surface of ECNFs (MnO_2@ECNFs, Co_3O_4@ECNFs, MnO_2/Co_3O_4@ECNFs). TEM sample preparation was carried out by dissolving fibers into ethanol/water (1:1 v/v) with ultrasonication, then dropping casting dissolved fibers onto a TEM grid for imaging. Energy dispersive X-ray spectroscopy (EDX) (Hitachi S-4800-I FESEM w/Backscattered Detector & EDX) was used to obtain the elemental mapping and atomic ratio. The phase and crystalline structure of the synthesized materials were assessed by X-ray powder diffraction (XRD) (Agilent Technologies Oxford Gemini X-Ray Diffractometer) equipped with a Cu-Kα radiation source (λ=0.15418 nm). Raman spectrum was performed by a Horiba XploRA One Raman Confocal Microscope System with 532 nm laser as the excitation source. X-ray photoelectron spectroscopy (XPS) (XPS, Thermo Fisher ESCALAB 250 Xi) was employed to study the elemental composition of the synthesized materials.

Electrochemical Measurement

All electrochemical measurements, including cyclic voltammetry (CV), Nyquist plots of electrochemical impedance spectroscopy (EIS) and chronoamperometry (CA), were performed on a Bio-Logic VMP3 electrochemical workstation by using a three-electrode set up system with a 3 mm diameter glass carbon (GC) working electrode, a platinum wire as a counter electrode and an Ag/AgCl (3 M KCl) as a reference electrode operating at room temperature. The electrodeposited square-shape MnO2/Co3O4@ECNFs (MnO_2@ECNFs, Co_3O_4@ECNFs) was cut into wafers with geometric area 0.5 × 0.5 cm^2 and then adhered onto the GC as a modified electrode with conductive carbon glue for further electrochemical experiment. EIS was performed in 0.1 M KCl and 5 mM $[Fe(CN)_6]^{3-/4-}$ by setting the working electrode voltage at 0.0 V vs. reference electrode Ag/AgCl within the frequency range from 100 kHz to 0.01 Hz where the distribution amplitude was 10 mV.

Results and Discussion

Preparation of Metal Oxide Electrodes and Characterization

The morphology and structure of as-prepared ECNFs, Co_3O_4@ECNFs, MnO_2@ECNFs and MnO_2/Co_3O_4@ECNFs were firstly characterized by a field-emission scanning electron microscopy (FESEM) and a transmission electron microscopy (TEM).

Figure 3.1 shows the FESEM images of the pristine and modified ECNFs with metal oxides. Figure 3.1a-b show low and high magnification FSSEM images of the as-prepared pristine ECNFs. They exhibit a well-aligned and smooth surface morphology. Figure 3.1c-h show the monometallic oxide or mingled binary metal oxides electrodeposited on the WA-ECNFs. It is obvious to see that the metal oxides on the scaffold were uniformly distributed to the carbon fibers. Comparing to the pristine ECNFs (Figure 3.1a-b), the diameters of the fibers with electrodeposition of metal oxides increase significantly, manifesting the electrodepositing successfully of the ultimate products. Figure 3.1d demonstrates that Co_3O_4@WA-ECNFs possess sheet-like Co_3O_4 clusters compacted at the surfaces of the fiber scaffold. The high-magnification SEM image of MnO_2@WA-ECNFs (Figure 3.1f) shows the interconnected MnO_2 frameworks which are composed of mesopores thorn-like nanostructure vertically grown at the surfaces of WA-ECNFs. For the electrodeposited binary MnO_2/Co_3O_4@WA-ECNFs, the mesoporous morphology of mingled metal oxides was observed as shown in the Figure 3.1h, which indicates the formation of hierarchical nanostructured MnO_2/Co_3O_4 hybrid. The morphology of the carbon fiber and metal oxides was further examined by TEM in Figure 3.1i-l where the crystallinity of them was confirmed by selected area electron diffraction (SAED). The plane (002) obtained in the inset of Figure 3.1i is consistent with the XRD peak of ECNFs at $2\theta = 26.54°$ plane in Figure 3.2b. In this pattern, the bright and broad continuous circle rings indicate amorphous character of carbon nanofiber layers.[153] Figure 3.1j shows coated Co_3O_4 nanostructured film with compacted mesopores at the carbon fiber surface where the SAED pattern represents the broad diffraction circle shape, suggesting more likely amorphous property of the Co_3O_4@WA-ECNFs. Different from Co_3O_4, the deposited MnO_2 exhibits thorn-like mesoporous structure in Figure 3.1k. The SAED pattern of the MnO_2@WA-ECNFs is characterized by complex bright diffraction spots, which indicates that the MnO_2 in the composites exists in polycrystallinity form.[154] For the binary MnO_2/Co_3O_4 deposition, Figure 3.1l features with the flocculent structure and mesopores of the mingled metal oxides. Combining the amorphous structure of Co_3O_4 film and polycrystallinity form of MnO_2, the characteristic multi-concentric diffraction rings of SAED pattern in Figure 3.1l still shows somewhat the polycrystalline nature of the nanostructured Co_3O_4/MnO_2 in the composites.

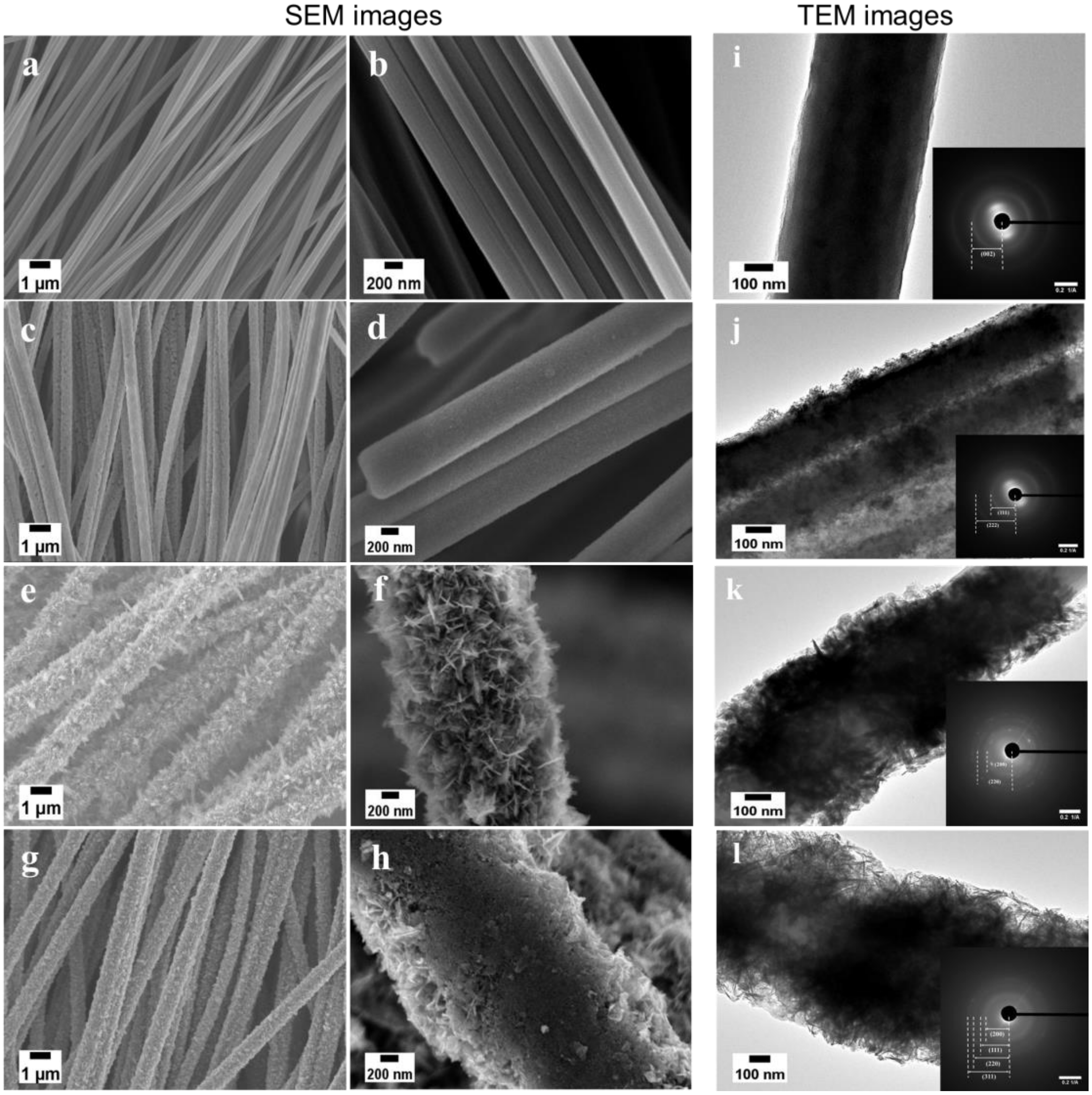

Figure 3.1 SEM and TEM Images: Low- and high-magnification SEM images of WA-ECNFs (a-b), Co_3O_4@ECNFs (c-d), MnO_2@ECNFs (e-f) and MnO_2/Co_3O_4@ECNFs (g-h); And TEM images of the ECNFs (i), Co_3O_4@ECNFs (j), MnO_2@ECNFs (k) and MnO_2/Co_3O_4@ECNFs (l), respectively. The inset in (i-l) are the selected area electron diffraction (SAED).

The chemical composition of the MnO_2/Co_3O_4@ECNFs was analyzed by energy-dispersed X-ray (EDX) spectroscopy. The EDX spectra (Fig. S3.1) verifies that the surface composition of the MnO_2/Co_3O_4@ECNFs is uniformly distributed the elements of C, O, Mn and Co. Therein, C and O elements are derived from the ECNFs, and the atomic ratio of manganese and cobalt is 15.82 % and 1.62 %, respectively, namely the mole ratio ~8:1 of Mn/Co in the composite. Raman spectroscopy, a non-destructive conventional tool,[62] was used to investigate the chemical structure of the carbon materials. In Figure 3.2a, the Raman spectrum (black curve) of the as-prepared ECNFs appears two prominent peaks of D-band and G-band at Raman shift of 1352 cm^{-1} and 1585 cm^{-1}, corresponding to the disordered carbon and graphitic carbon, respectively.[155] The intensity ratio of D/G band represents the atomic ratio of sp^3/sp^2 carbons, which is a measure of the extent of disordered graphite in plane sp^2 domains.[156] The intensity of D/G (I_D/I_G) was found to be approximately 1.03 for the as-prepared ECNFs. The Raman spectrum (Figure 3.2a red) of MnO_2/Co_3O_4@ECNFs also have both D and G bands at the same Raman shift, however the intensity decreased significantly, ascribing to the decorated metal oxides.[157] The intensity of D and G bands for Co_3O_4@ECNFs and MnO_2/Co_3O_4@ECNFs behaves much less than that of ECNFs or MnO_2@ECNFs. This is mostly ascribed to much more denser metal oxide parcel at the fiber surfaces. Besides, the ratio of (I_D/I_G) slightly decreased from 1.03 of the pristine ECNFs to 1.00 of the MnO_2/Co_3O_4@ECNFs. The change in the intensity ratio of D/G suggests that the increment of the graphitic degree was caused by the binding of carbon and MnO_2/Co_3O_4.[158] And the decrease of the sp^2 domains manifests the defect in the carbon matrix due to the removal of oxygen containing groups from the ECNFs surfaces.[108] For the MnO_2@ECNFs, Mn-O stretching vibration band present at the expected Raman shift of 635 cm^{-1}, and another peak at 342 cm^{-1} could be regarded as the lattice vibration of

Mn-O (Figure 3.2a magenta),[159, 160] notably, both monometallic MnO_2 and binary decorated ECNFs exhibits these characteristics. Besides, the characteristic Co-O Raman shift of 497 cm^{-1} and 640 cm^{-1} (Figure 3.2a blue) exists for the Co_3O_4@ECNFs sample.[48] The Raman spectrum for the MnO_2/Co_3O_4@ECNFs represents coupling of the Raman shift of the mingled binary metal oxide nanostructures co-wrapped at the surfaces of the WA-ECNFs. Compared with the other two samples, the MnO_2/Co_3O_4@ECNFs could observe a slight red shift at Raman shift of 628 cm^{-1}, which sheds light on the big influence from the synergistic effect of manganese and cobalt oxides.[161] The observed Raman shift to lower wavelength could attribute to an increment of the crystal size of the mingled oxides based on a phonon quantum confinement model.[162]

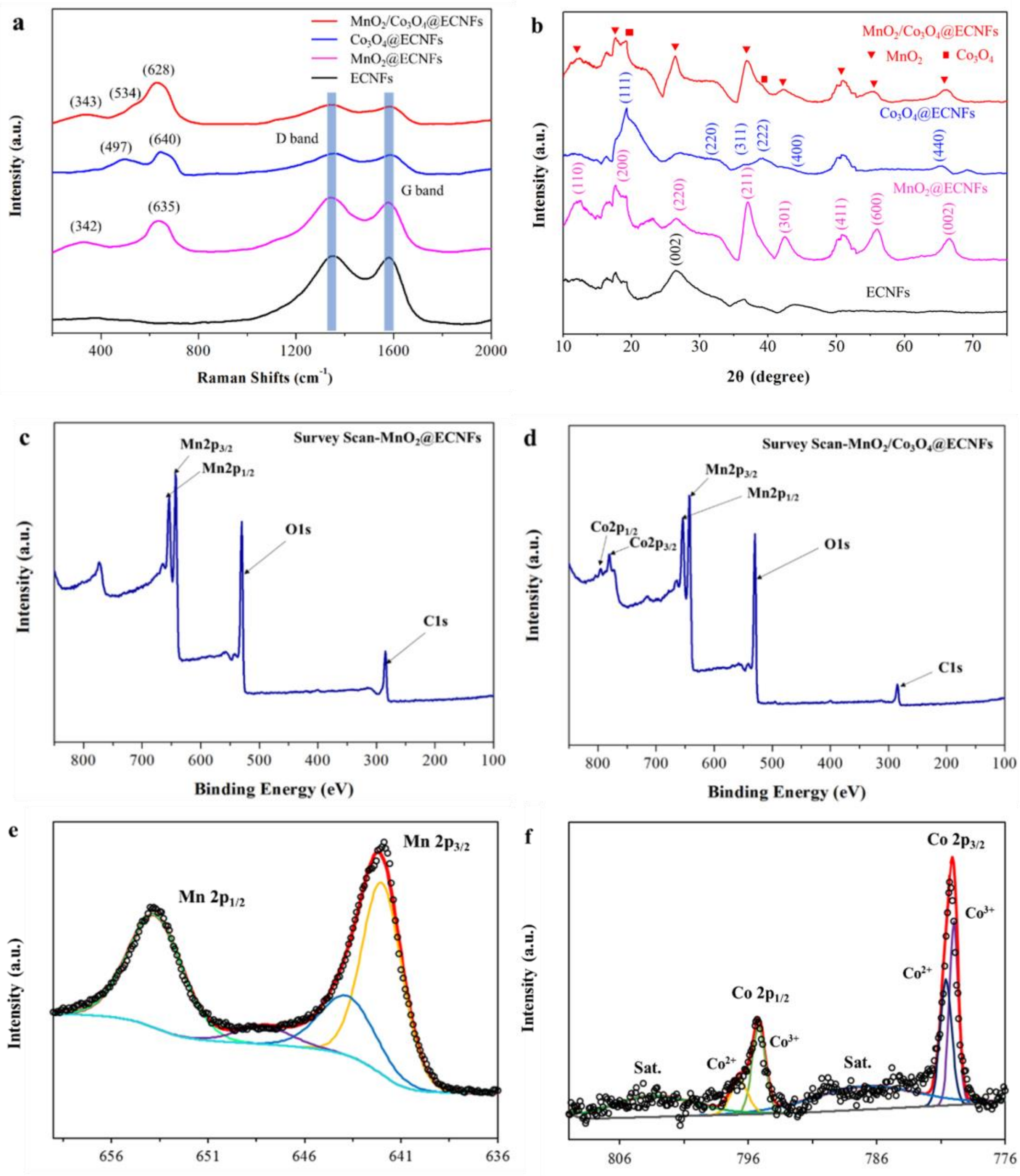

Figure 3.2 Raman, XRD and XPS Characterization: (a) Raman spectrum and (b) XRD patterns of the as-prepared ECNFs, MnO$_2$@ECNFs, Co$_3$O$_4$@ECNFs and MnO$_2$/Co$_3$O$_4$@ECNFs. (c-d) Survey scan spectra of XPS of MnO$_2$@ECNFs and MnO$_2$/Co$_3$O$_4$@ECNFs, respectively. Deconvoluted peak of (e) Mn$_{2p}$, (f) Co$_{2p}$.

Furthermore, the phase compositions and crystallographic structures of ECNFs, Co_3O_4@ECNFs, MnO_2@ECNFs and MnO_2/Co_3O_4@ECNFs were examined by X-ray diffraction (XRD) measurement. In Figure 3.2b (black), a broad peak at around $2\theta=26.54°$ corresponds to the (002) reflection of a graphitic-type lattice of the ECNFs. The XRD pattern of the MnO_2@ECNFs (Figure 3.2b magenta) can be indexed into a pure tetragonal phase of α-MnO_2 (JCPDS 44-0141),[163-165] at 2θ of 12.4°, 17.7°, 26.6°, 37.1°, 42.4°, 50.7°, 55.9° and 66.5°, corresponding to the diffraction planes of (110), (200), (220), (211), (301), (411), (600) and (002) of MnO_2 crystals, respectively. The XRD spectrum (Figure 3.2b blue) of the Co_3O_4@ECNFs matches well with the standard pattern (JCPDS No. 43-1003),[166, 167] revealed by the diffraction peaks at 2θ values of 19.18°, 31.23°, 36.85°, 38.99°, 44.72° and 64.40°, corresponding to (111), (220), (311), (222), (400), and (440) crystal planes, respectively. From the XRD spectrum of Co_3O_4@ECNFs, it is observed that all the peaks are weak and broad, except (111) crystal planes. Thus, the sample has the poor crystallinity which corresponds with the amorphous structure confirmed by SAED (Figure 3.1j). For the MnO_2/Co_3O_4@ECNFs (Figure 3.2b red), the diffraction peaks at 19.2° and 39.1° can be index to the (111) and (222) planes of Co_3O_4,[168] respectively. The peaks of Co_3O_4 in the composite show obvious low intensity, ascribing to a small crystallite size of the decorated Co_3O_4 compared to α-MnO_2,[34, 169] and a low atomic ratio of cobalt which is consistent with the results of EDX spectroscopy.

The chemical composition and the metal oxidation states of the synthesized materials were further investigated by the X-ray photoelectron spectroscopy (XPS). XPS full survey spectrum of the MnO_2@ECNFs (Figure 3.2c) illustrates the presence of carbon, oxygen and manganese on the surface of the materials by their distinctive peaks, while the survey spectrum of the hybrid MnO_2/Co_3O_4@ECNFs shows distinctive peaks which could be indexed into Co_{2p}, Mn_{2p}, O_{1s} and C_{1s} regions (Figure 3.2d). The atomic ratio of cobalt obtained from XPS result is about 1.98 %, which is reasonably consistent with EDX spectroscopy (Fig. S3.1). The high-resolution Mn_{2p} spectrum (Figure 3.2e) for the MnO_2/Co_3O_4@ECNFs shows two distinct peaks having a spin-energy separation of 11.4 eV at binding energies of 642.2 and 653.6 eV in the Mn_{2p} spectrum signifying $Mn_{2p3/2}$ and $Mn_{2p1/2}$, which demonstrate the valence value of Mn^{4+} in the composite, a good agreement with those reported value for MnO_2.[170] Similarly, the devolution of the complex Co_{2p} spectrum in Figure 3.2f shows the presence of two chemically distinct states of Co^{2+} and Co^{3+}. Specially, two distinctive peaks located at 780.1 and 795.3 eV having a spin orbital splitting of 15.2 eV can be assigned to the $Co_{2p3/2}$ and $Co_{2p1/2}$, respectively.[171] In particular, the two principle peaks are fitted into four subpeaks, wherein two peaks at 779.9 and 795.1 eV with the satellite peak at 786.9 eV prove the chemical nature of Co^{3+}, and the fitting peaks at 780.6 and 796.7 eV with the satellite peak at 803.4 eV are indexed to Co^{2+}.[40, 172] These results verify the presence of Co_3O_4 phase in the as-fabricated MnO_2/Co_3O_4@ECNFs. The O_{1s} spectrum (Fig. S3.2) is composed of three peaks at 529.6, 530.8 and 532.4 eV, which are attributed to oxygen states in the Co_3O_4 and MnO_2 crystal lattice, the O_x^- (O^- or O_2^-) ion absorbed by the oxygen deficient region of the hybrid nanomaterials lattice and additional physically absorbed and/or chemisorbed oxygen caused by surface hydroxyl,[34, 173] These functional groups will be beneficial to the electro-catalytical performance, owing to improving the wettability between the electrode and electrolyte.

Electrochemical Characterization of the Metal Oxide Electrodes

The electrochemical behaviors of the as-prepared ECNFs, Co_3O_4@ECNFs, MnO_2@ECNFs or MnO_2/Co_3O_4@ECNFs modified GC electrodes and bare GCE in 0.1 M KCl containing 5 mM $[Fe(CN)_6]^{3-/4-}$ were firstly studied at a scan rate of 20 mV/s by cyclic voltammetry (Figure 3.3a). The cyclic voltammograms (CVs) of bare GCE present a pair of anodic and cathodic peaks with lower peak current signal than that electrodes with different modified ECNFs. Besides, the current values represent the sum of the charge current in the positive and negative scan direction at the modified electrodes, correspondingly. Herein, the geometric area could be used for qualitative determination of double layer capacitance. Therefore, the electrode decorated with MnO_2/Co_3O_4@ECNFs exhibits the highest charge current storage ability over the others in Figure 3.3a.

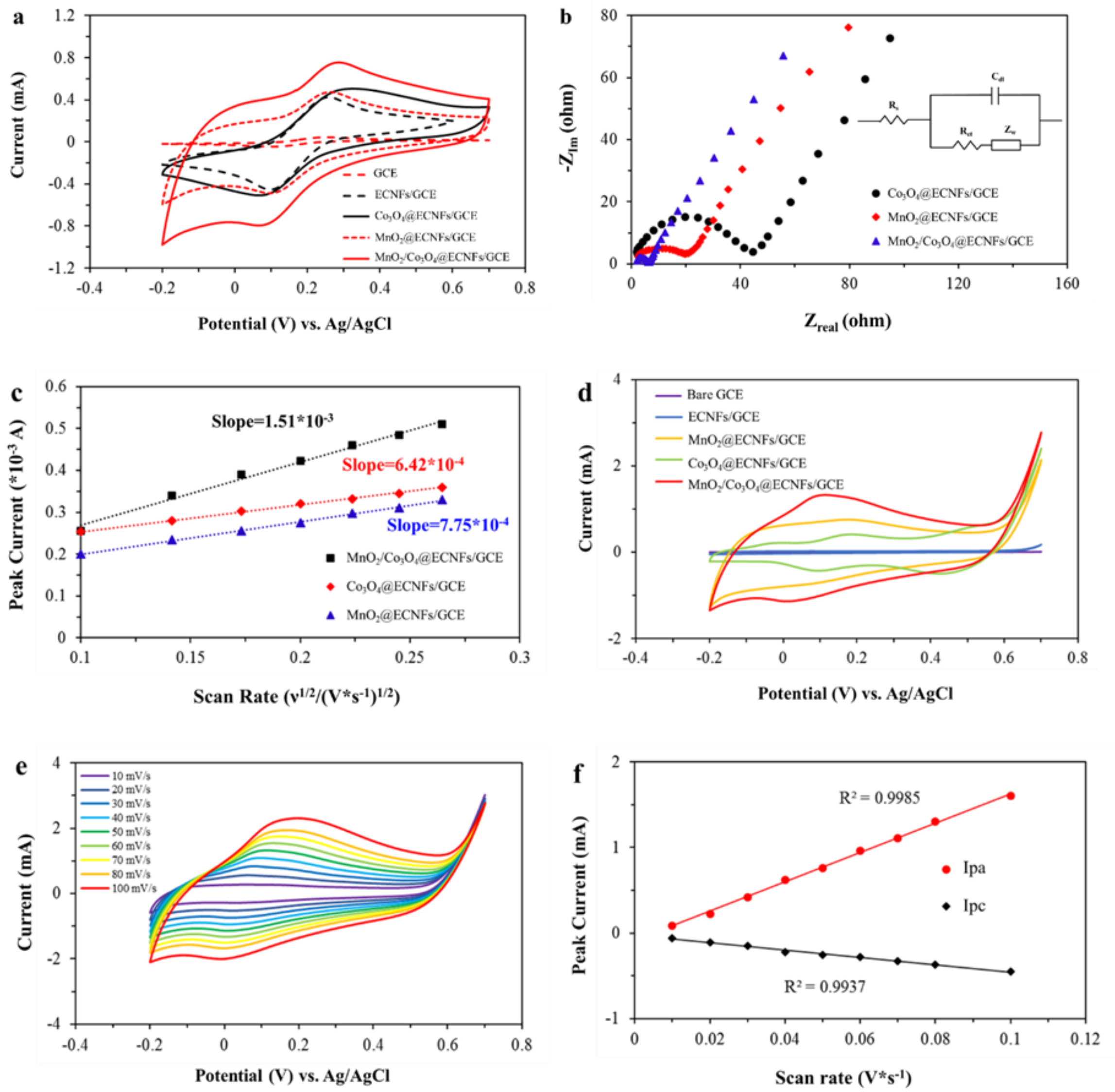

Figure 3.3 Electrochemcial Characterization: (a) CV curves and (b) Nyquist plots of EIS within the frequency range from 100 kHz to 0.01 Hz where the distribution amplitude was 10 mV of different modification of electrodes in 0.1 M KCl solution containing 5 mM $[Fe(CN)_6]^{3-/4-}$; (c) Randles-Sevcik plots derived from the dependences of anodic peak current on the square root of the voltage scan rate of different modified GC electrode (MnO_2/Co_3O_4@ECNFs, Co_3O_4/ECNFs, MnO_2/ECNFs) immersed in 0.6 M NaOH solution containing 5 mM $[Fe(CN)_6]^{3-}$, scan rate from 10 to 70 mV s^{-1}. (d) CV curves of different modification of electrodes in 0.6 M NaOH solution at the scan rate of 50 mV s^{-1}. (e) CV curves of the MnO_2/Co_3O_4@ECNFs modified GC electrode with different scan rates in 0.6 M NaOH electrolyte solution. (f) The plot of peak currents vs. scan rates with MnO_2/Co_3O_4@ECNFs modified GC electrode.

Electrochemical impedance spectroscopy (EIS) was carried out to investigate the electrochemical kinetics of GC electrodes modified with different electrocatalysts at an open-circuit potential within the frequency range from 100 kHz to 0.01 Hz where the distribution amplitude was 10 mV. Figure 3.3b exhibits the EIS spectra of three electrodes, i.e. the Co_3O_4@ECNFs, MnO_2@ECNFs and MnO_2/Co_3O_4@ECNFs. The efficient charge transport ability was conformed in the Nyquist plots in Figure 3.3b, whose data were analysis by fitting a Randle's equivalent circuit,[57] shown in the inset. The Nyquist plot consists of a depressed overlapping capacitive semicircle in the high frequency region and a linear line in the low frequency domain. The diameter of the semicircle in the high frequency indicates the bulk charge transfer resistance (R_{ct}), while the linear portion is attributed to an interfacial diffusion-limited process.[174] Therein, MnO_2/Co_3O_4@ECNFs shows smallest semicircle and lowest R_{ct} (~8 Ω) compared to the ones that electrodeposited monometallic oxide of MnO_2 (~20 Ω) or Co_3O_4 (~45 Ω) onto the WA-ECNFs, indicating the highest efficient electron and mass transport at the MnO_2/Co_3O_4@ECNFs electrode. The decrease of resistance could be ascribed to the porous structure with more accessible surface area for the electrolyte ions.[175] This corroborates the improvement of the ion diffusion to the electrode surface and electrical conductivity due to the structural and morphological features of the binary MnO_2/Co_3O_4@ECNFs.

In order to assess the specific active surface area of the modified GC electrode in electrochemistry, CV curves were recorded at different scan rates in 0.6 M NaOH solution containing 5 mM $[Fe(CN)_6]^{3-}$ (Fig. S3.3). The peak current for the reversible redox reaction is given by the Randles-Sevcik equation:[176]

$$I_P = 2.69 \times 10^5 n^{3/2} A C_0 D^{1/2} v^{1/2} \ldots\ldots(3\text{-}1)$$

where n represents the number of electrons, A represents the active surface area of the electrode (in cm^2) , C_0 is the concentration of the electroactive compounds (in mol cm^{-3}), D is the diffusion coefficient of $[Fe(CN)_6]^{3-}$ (7.6×10^{-6} cm^2 s^{-1}),[158] v represents the scan rate (in V s^{-1}). The active surface area was determined by the slope of the linear behavior of I_p versus $v^{1/2}$ (Figure 3.3c). The active surface area of different modified electrodes was obtained 0.41 ±0.01 cm^2 for MnO_2/Co_3O_4@ECNFs, 0.17 ± 0.01 cm^2 for Co_3O_4@ECNFs and 0.20 ± 0.01 cm^2 for MnO_2@ECNFs. Such findings agree with the morphology analysis by SEM and TEM images. The electrode of MnO_2/Co_3O_4@ECNFs shows the highest current signal in Figure 3.3a, owing to its highest electron conduction property and largest specific active surface area compared to ECNFs, Co_3O_4@ECNFs or MnO_2@ECNFs.

Figure 3.3d shows the steady-state CV curves of different electrodes in 0.6 M NaOH electrolyte solution without any analyte (glucose) at a scan rate of 50 mV s^{-1}. CV experiments were carried out in the potential range from -0.2 to 0.7 V vs. Ag/AgCl to observe the redox reaction of the electrodes. The anodic and cathodic peaks only can be observed on the electrodes modified with metal oxides on the WA-ECNFs. There are no noticeable redox peaks observed for either the bare GCE or ECNFs modified GCE in the alkaline solution. One can conclude that the oxidation and reduction peaks are arising from the metal oxides of Co_3O_4 and/or MnO_2. In the CV curve of Co_3O_4@ECNFs/GCE (Figure 3.3d green curve), two pairs of redox peaks were observed at oxidation peaks, 0.15 V and 0.48 V, which can be assigned to the reversible transition between Co_3O_4 and CoOOH, as well as the transition between CoOOH and CoO_2 (Eq.3.2, 3.3 and 3.4), respectively.[34, 177]

$Co_3O_4 + 4H_2O + 2e^- \leftrightarrow 3Co(OH)_2 + 2OH^-$ ....(3-2)

$Co(OH)_2 + OH^- \leftrightarrow CoOOH + H_2O + e^-$ ....(3-3)

$CoOOH + OH^- \leftrightarrow CoO_2 + H_2O + e^-$..(3-4)

In addition, a pair of broad but weak oxidation and reduction peak of MnO_2@ECNFs/GCE between -0.1 and 0.4V was obtained in Figure 3.3d (yellow curve), owing to the oxidation of MnO_2 to Mn (VI) and reduction of Mn (VI) to MnO_2.[178] What's more, the binary MnO_2/Co_3O_4@ECNFs/GCE shows a high-intensity redox pair with a larger broad oxidation peak at around 0.1 V in Figure 3.3d (red curve). The presence of a single oxidation peak in the electro-catalytical system with two metal oxides suggest that the centers of nanocomposites act together in the electrochemical reaction. Besides, this oxidation peak potential of the binary metal oxide electrode has a shift to a smaller over potential than that of the monometallic oxide, MnO_2 or Co_3O_4 (Eq. 3.3 &3.4) electrode, suggesting a faster kinetics of the redox reaction. Such shift in the negative direction is attributed to the "mingled" binary metal oxides and increased interfaces which enhance the active sites and large electron transport channels in the electrode. It is expected that molecules and ions involved in the glucose oxidation will be facilitated to approach the active sites; and the activation energy, i.e. the required applied voltage, for glucose oxidation will be reduced, thus accelerating the catalyzed reaction.[179] Furthermore, the MnO_2/Co_3O_4@ECNFs electrode exhibits much higher current and capacitance in the electrolyte solution compared to the electrode of monometallic oxide MnO_2 or Co_3O_4, a manifestation of its higher conductivity and larger specific electrochemical surface area.

In order to confirm the intrinsic redox reactions of metal oxides, the relationship between the peak current and voltage scan rate was performed by using cyclic voltammetry in 0.6 M NaOH. The measurements were carried out under different scan rates (10, 20, 30, 40, 50, 60, 70, 80 and 100 mV/s). The results are shown in Figure 3.3e for the binary metal oxides and Fig S3.4a and Fig S3.4c for the monometallic oxide Co_3O_4@ECNFs and MnO_2@ECNFs, respectively. The linear relationship of the anodic and cathodic peak currents versus scan rate (Figure 3.3f, Fig. S3.4b and Fig. S3.4d) indicates the redox reactions of the metal oxides decorated electrodes are a typical surface-confined reaction.[180]

Electro-oxidation of Glucose at the Metal Oxide Electrodes

The electrooxidation of glucose at Co_3O_4@ECNFs/GCE, MnO_2@ECNFs/GCE and MnO_2/Co_3O_4@ECNFs/GCE was characterized by cyclic voltammetry. Figure 3.4a demonstrates the CVs of the binary MnO_2/Co_3O_4@ECNFs electrode with glucose concentrations in the range from 0 to 7 mM. The oxidation peak currents increase correspondingly with the augment of glucose concentration, an indication of the glucose oxidation. Taking the peak currents at the potential position of 0.55 V, which shows the most significant changes with addition of glucose, we plotted the corresponding calibration curve of peak current as a function of glucose concentration (Figure 3.4b). It displays a linear correlation over the glucose concentration with a correlation coefficient of 0.987. Similarly, the CV curves (Fig. S3.5) of Co_3O_4@ECNFs and MnO_2@ECNFs were also obtained with addition of glucose. The linear fitting of the calibration curves gives the slopes of 0.0655, 0.1986, and 0.2258 for MnO_2@ECNFs, Co_3O_4@ECNFs, MnO_2/Co_3O_4@ECNFs, respectively. To further understand the enhanced electrochemical performance of MnO_2/Co_3O_4@ECNFs towards glucose oxidation, the Tafel curves were obtained in Fig. S3.6, depicting a comparison for the three types of electrodes. In the Tafel curve of MnO_2/Co_3O_4@ECNFs, the equilibrium potential as defined by zero overpotential was observed at -0.13 V. Whereas, MnO_2@ECNFs and Co_3O_4@ECNFs hold more negative equilibrium potential, -0.15 V and -0.18 V, compared to the hybrid electrode. The hybrid MnO_2/Co_3O_4@ECNFs demonstrates the highest kinetics (largest exchange current density at equilibrium potential). In addition, the Tafel slope of the three electrodes followed a trend as Co_3O_4@ECNFs > MnO_2@ECNFs > MnO_2/Co_3O_4@ECNFs shown in Figure 3.4c. The lowest Tafel slope of the hybrid composite electrode indicates the highest charge transferability of the materials,[181] suggesting the synergistic effect of mingled metal oxides at the ECNFs. These results indicate a better electro-oxidative performance of the MnO_2/Co_3O_4@ECNFs than the monometallic oxide electrodes. The plausible reactions involved for the electrocatalytic oxidation of glucose at the MnO_2/Co_3O_4@ECNFs electrode are described in Eq. 3-5 and 3-6.[182] The CoO_2 and MnO_2 in the presence of glucose convert to CoOOH and MnOOH, respectively. Therefore, the redox reactions would greatly promote to the forward oxidative reaction ($CoOOH \rightarrow CoO_2$, $MnOOH \rightarrow MnO_2$), resulting in monotonic increase of the oxidation peak upon the addition of glucose.

$2CoO_2 + C_6H_{12}O_6$ (glucose) $\rightarrow 2CoOOH + C_6H_{10}O_6$ (gluconolactone) ....(3-5)

$2MnO_2 + C_6H_{12}O_6$ (glucose) $\rightarrow 2MnOOH + C_6H_{10}O_6$ (gluconolactone).....................(3-6)

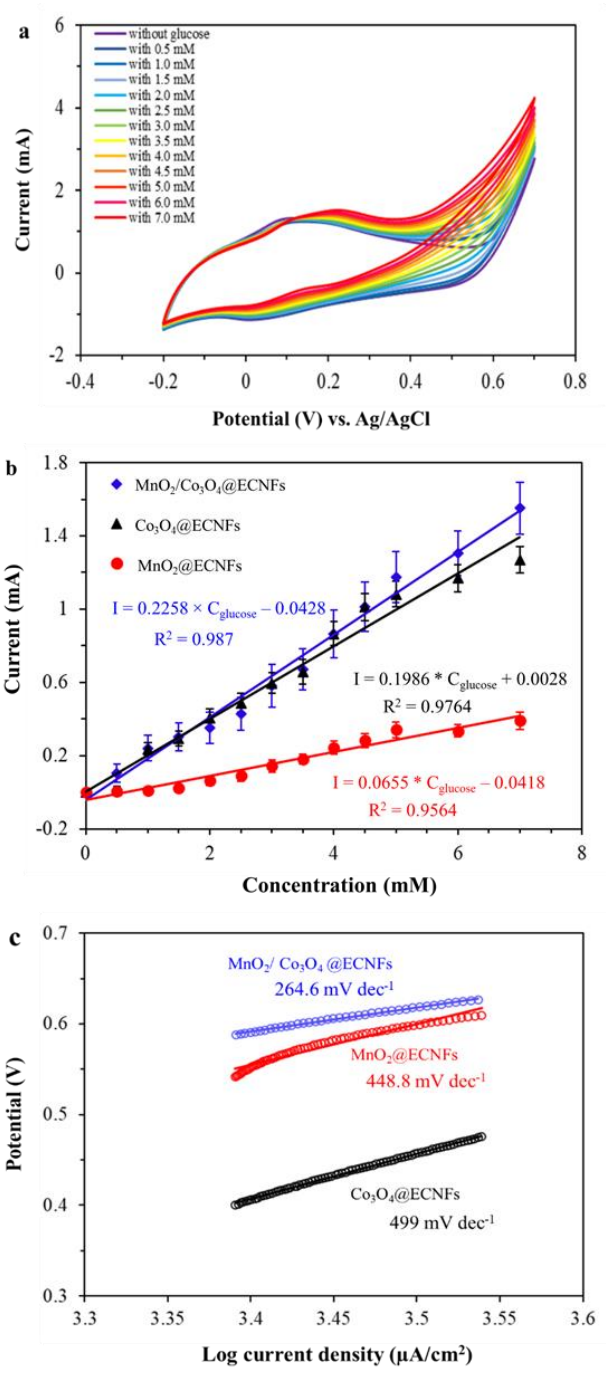

Figure 3.4 Electrochemical Performance Tests: (a) CV curves of the MnO_2/Co_3O_4@ECNFs/GCE at different concentrations of glucose, ranging from 0.5 to 7 mM at the scan rate of 50 mV/s. (b) Corresponding calibration plot of oxidation current versus concentration of glucose of the MnO_2/Co_3O_4@ECNFs, Co_3O_4@ECNFs and MnO_2@ECNFs. (c) Tafel slope diagram of various electrodes with 1mM glucose.

According to aforementioned reaction mechanisms, the electrooxidation of glucose at the binary metal oxide electrode is schematically illustrated in the Figure 3.5. Because the MnO_2/Co_3O_4@ECNFs demonstrate the well-alignment and mesoporous morphology of metal oxides, the scaffold not only enhances the mobility of electrons through the whole body of MnO_2/Co_3O_4@ECNFs, but also extends the number of electron transfer channels. Hence it may increase the delocalization of charges, realizing the improved conductivity and better electrochemical performance in the efficiency for glucose oxidation. The glucose molecules diffuse onto the high porosity of the binary metal oxides, then access and absorb to the metal oxide catalytic active sites, followed by the electrocatalytic oxidation. The intimate contact of the heterogeneous interfaces for glucose molecules with a minimal diffusion resistance is achieved.[183] Besides, such hybrid nanomaterials integrate fine electronic configuration of semiconductor of MnO_2 and Co_3O_4, which have more valence states to provide more redox reactions.[34, 173] It is plausible that the charge transfer from p orbital of O in the glucose molecules to the d orbital of Mn and Co in the nanocomposite, enhancing the density of state (DOS) of Mn and Co d orbital near the Fermi level after anchoring glucose molecules. The presence of occupied states near the Fermi level would be in favor for metal ions to transfer charge from the glucose through redox reactions. Hence, the synergistic effect between WA-ECNFs and binary metal oxides is expected. The MnO_2/Co_3O_4@ECNFs possess a nonzero DOS at the Fermi level, where substantial charge transfer from metal oxides to ECNFs occurs due to the energy difference of valence between conduction band edges and conductivity of the presence of ECNFs, which in turn may enhance the sensitivity of the nonenzymatic sensor from MnO_2/Co_3O_4@ECNFs.[32]

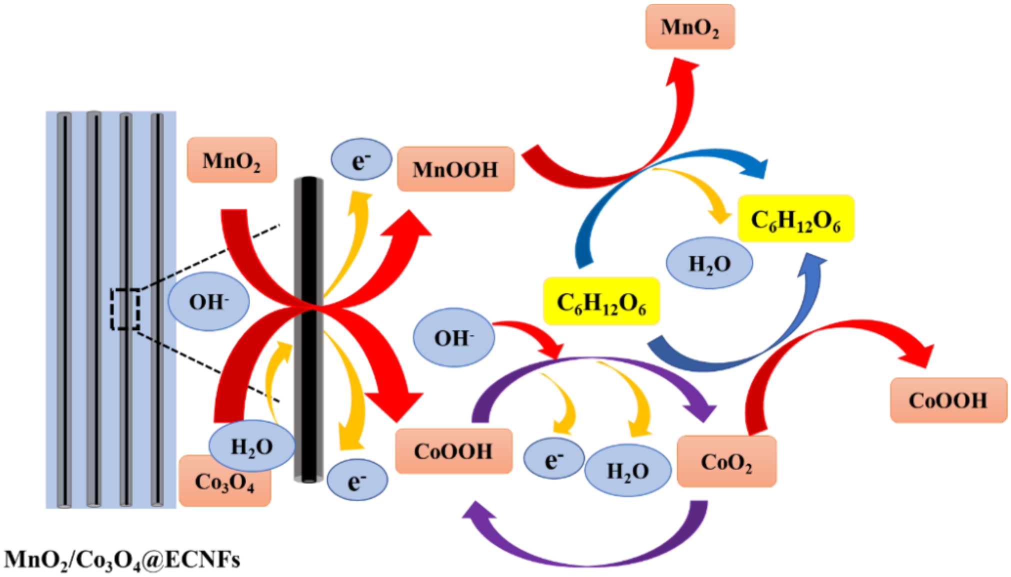

Figure 3.5 A Schematic Illustraction of Electrocatalytic Machenism: schematic illustration of the proposed electrocatalytic mechanisms for the glucose oxidation at the MnO_2/Co_3O_4@ECNFs hybrid structure.

Amperometry Detection of Glucose

Because the MnO_2/Co_3O_4@ECNFs electrode shows better electrocatalytic activity in contrast to monometallic oxide at ECNFs, it was tested for amperometric glucose sensing. Amperometry is a simple and economic electrochemical technique for evaluating sensing application in terms of the sensitivity and specificity. In order to determine the best voltage for electrocatalytic reaction of glucose oxidation, we measured the current responses with presence of glucose at different voltages. Fig. S3.7 displays the results which clearly indicate that the potential at 0.55 V has the greatest electrocatalytic current of glucose oxidation for optimal electrochemical sensitivity and selectivity.

The real-time amperometric detection of glucose on the MnO_2/Co_3O_4@ECNFs electrode was performed by successive stepwise addition of different concentration of glucose into stirring alkaline electrolyte solution with fixed intervals at an applied potential of 0.55 V, resulting in a step rise of current (Figure 3.6a). The nonenzymatic electrode demonstrated a rapid glucose response at a concentration of 5 μM by reaching a steady signal within 5 s. The limit of detection (LOD) was determined to be 0.3 μM (with S/N=3) and the detection sensitivity of 1159 μA mM^{-1} cm^{-2} determined by the slope of the linear fitting. The detection performance of this enzymeless glucose sensor was compared to a series of reported enzymeless glucose sensing based on MnO_2 or Co_3O_4 in Table S3.1. The MnO_2/Co_3O_4@ECNFs electrode in this work exhibits greatly improved sensitivity and detection limit as a comparsion to most reported results.

Figure 3.6b shows the corresponding calibration curve fits well with a Langmuir isothermal model. This result suggests that the electrochemical oxidation of glucose on MnO_2/Co_3O_4@ECNFs is a surface catalytic reaction.[171] The calibration data fit the Langmuir isothermal equation very well over a range of concentration from 5 μM to 10.9 mM (R^2=0.9997), which is expressed as Eq. 3-7:

$$I(\mu A) = 475.16 \times C_{glucose}\,(mM)/\,(1 + 0.397 \times C_{glucose}\,(mM)) \quad \text{.......................................(3-7)}$$

When the glucose concentration is as low as the value of $0.397 \times C_{glucose} << 1$, the Eq. 3-7 can be approximated as a linear equation: $I(\mu A) = 475.16 \times C_{glucose}(mM)$. In this case, the sensitivity is calculated to be 1159 μA mM^{-1} cm^{-2}, which reasonably agrees with the experimental result (1045 μA mM^{-1} cm^{-2}) if only considering the linear range of 5 μM

~ 0.57 mM. On the other hand, the glucose oxidation can be separated to be two ranges of linear function for the concentration of 5 μM ~ 0.57 mM and 0.57 mM~1.93 mM (inset: Figure 3.6b). The two linear calibration plots of the oxidation current vs. glucose concentration can be fitted as (I): $I(\mu A) = 428.52 \times C_{glucose} - 0.2016$ (R^2=0.9985) and (II): $I(\mu A) = 209.42 \times C_{glucose} + 124.23$ (R^2=0.9948). The sensitivity of concentration range of 0.57 mM ~ 1.93 mM is calculated to be 511 μA mM^{-1} cm^{-2}. The fit of Langmuir isothermal theory to the electroxidation of glucose suggests that the reaction is limited by the absorption process of glucose onto the electrochemical active sites followed with faste redox reaction and charge transfer. In the linar range of 5 μM ~ 0.57 mM of the fit, MnO_2/Co_3O_4@ECNFs could ideally both absorb the glucose molecules and desorb reaction of by-products efficiently to allow further catalytic reactions to take place. When $C_{glucose}$ further increases to the range of 0.57 mM~1.93 mM, the MnO_2 and Co_3O_4 in the hybrid nanoelectrode allow them strongly bind to the glucose molecules via van der Waals interactions because of the formation of a band between O of glucose and O of the hybrid MnO_2/Co_3O_4 with glucose system, accompanying with large change in the density of states (DOS), where the glucose molecules are at the valence band maximum of the hybrids.[32] At higher concentrations, it is unlikely that the glucose molecules can be oxidized and then released from the defect for efficient sensing because of the surface fouling from by-products of glucose oxidation thus decreased diffusion coefficient and slower electron transfer.[54]

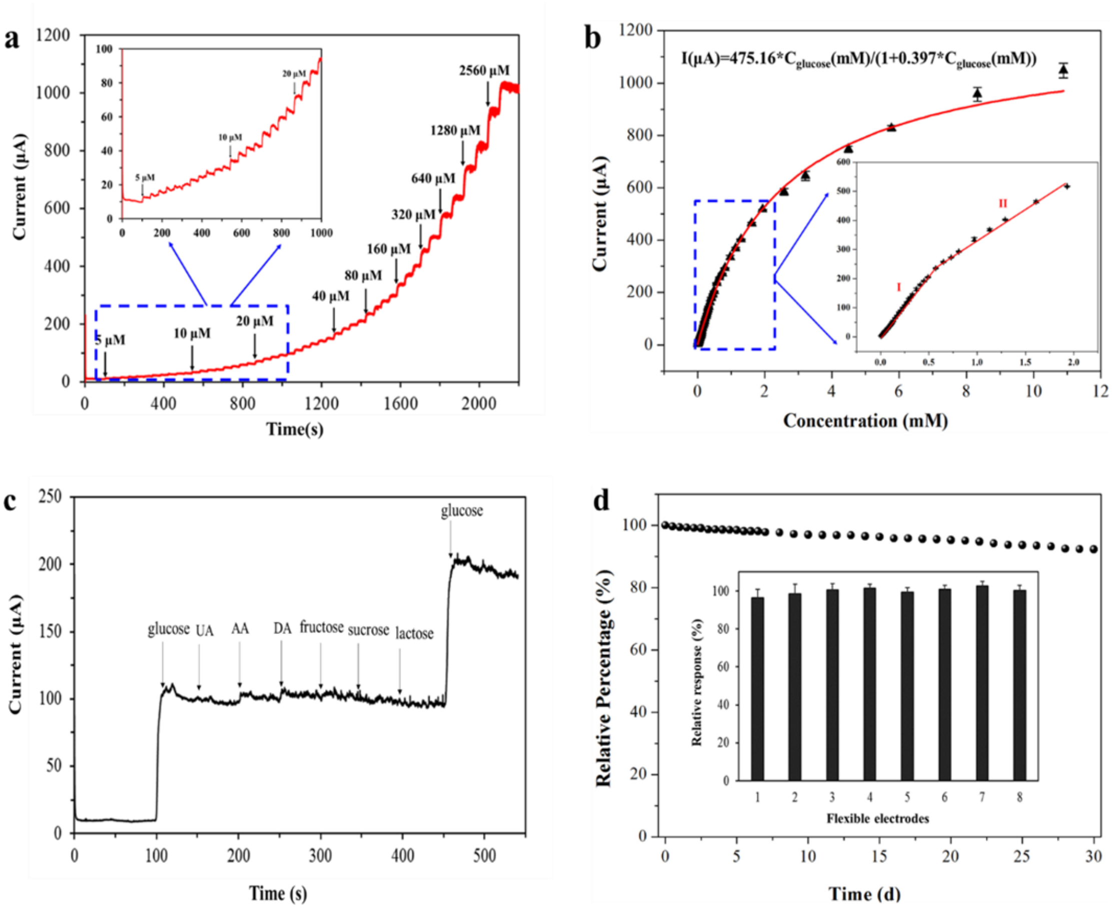

Figure 3.6 Sensitivity, Selectivity, Stability and Reproducibility Tests: (a) Typical amperometric response of GC electrode modified with MnO_2/Co_3O_4@ECNFs against successive addition of different glucose concentration in 0.6 M NaOH at a constant applied potential of 0.55 V (v. Ag/AgCl). (b) The corresponding Langmuir isothermal fitting curve (red line); the inset is a zoom of linear range. (c) Amperometric response of MnO_2/Co_3O_4@ECNFs/GCE to the addition of glucose (0.25 mM) and different inferences (0.025 mM, respectively) in 0.6 M NaOH at an applied potential of 0.55 V (v. Ag/AgCl). (d) Variation of the response current of the MnO_2/Co_3O_4@ECNFs based nonenzymatic glucose sensor to 5.0 mM glucose with time, and the inset is the current response of 8 separately prepared MnO_2/Co_3O_4@ECNFs/GC electrodes to 5.0 mM glucose.

The specificty of the MnO_2/Co_3O_4@ECNFs/GC electrode is a significant parameter to evaluate the performance for an electrochemical glucose sensor. Some endogenous compounds, such as uric acid (UA), ascorbic acid (AA), dopamine (DA), fructose, sucrose and lactose, typically co-exist with glucose on physiological fluids. The physiological glucose level is normally 10 times higher than the interferences. Hence the MnO_2/Co_3O_4@ECNFs/GC electrode was evaluated using those compounds. Figure 3.6c shows the amperometric responses with glucose and interfering substances at the applied voltage 0.55 V vs. Ag/AgCl. It was observed that the addition of other carbohydrate isomers had negligible influence on glucose electrochemical signals at the MnO_2/Co_3O_4@ECNFs electrode, indicating that the resultant amperometric sensor is highly selective for the detection of glucose.

Furthermore, the stability of the MnO_2/Co_3O_4@ECNFs electrode stored at room temperature was investigated by periodically recording its current response to 5.0 mM glucose. The oxidation current retained 92.3 % of its initial value after 30 days (Figure 3.6d). Besides, the reproducibility of the glucose sensor was evaluated independently at a given glucose concentration for five successive measurements with eight different MnO_2/Co_3O_4@ECNFs/GC electrodes. The results provide a relative standard deviation less than 4 % (Figure 3.6d inset), confirming that the binary metal oxide electrodes have great long-term stability and reproducibility. The practical testing of this MnO_2/Co_3O_4@ECNFs electrode was established by spiking human serum samples with predetermined amount of glucose solution. The human serum was centrifuged at 10000 rmp for 15 mins and dilute 50 times with (1x) potassium buffer solution (PBS) at PH 7.4. Then, the diluted serum was mixed with different concentrations of glucose and added into the experimental system. The measurement results are summarized in Table S3.2.

The recovery rates of the spiked standard solutions are almost 100 %, indicating the potential of the nonenzymatic glucose sensor in practical applications.

Conclusion

In summary, an electrode of binary metal oxides (MnO_2/Co_3O_4) decorated on the WA-ECNFs has been successfully synthesized through a facile electrodeposition technique. The MnO_2/Co_3O_4 metal oxides exhibit mesoporous surfaces with excellent electrochemical performance for glucose sensing. Primarily, the mophology of the binary metal oxides guarantees improved electrical conductivity (faster charge transfer), increased active surface area in electrochemistry over the monometallic oxides (MnO_2 or Co_3O_4) and facilitated mass transfer to the surfaces. The defects in the hybrid nanoelectrode have more valence states to provide redox reactions, and allow electronic configuration to facilitate the charge transfer. These synergistic effects of the binary metal oxides with aligned scaffold have significantly improved the sensing activity with excellent sensitivity of 1159 $\mu A\ mM^{-1}\ cm^{-2}$ and a good detection limit of 0.3 μM (S/N =3) with a dynamic range of 5 μM to 10.9 mM. The nonenzymatic glucose biosensor has been tested with high specificity, long-term stability and reproducibility. It shows almost 100% recovery for detection of glucose spiked in human serum samples. This work demonstrates significant improvement on developing metal oxide-based, low-cost and high-efficient nonenzymatic electrooxidation of glucose and an electrochemical sensor detection.

CHAPTER IV

COBALT OXIDE NANOGRAINS ON ALIGNED N-DOPED ELECTROSPUN CARBON NANOFIBERS AS SENSORS FOR THE ELECTROCHEMICAL DETECTION OF DOPAMINE SECRETED BY LIVING CELLS

Introduction

Despite significant advances in the electrochemical detection of small molecular metabolites, a growing need exists for the development of portable point-of-care medical products with flexible, implantable, and wearable electrochemical sensing systems.[184] Such biosensors hold considerable promise for clinical diagnosis and continuous monitoring of complex human health conditions and are currently implemented for recording glucose levels,[185] monitoring relevant serotonin levels[186] and determination of hydrogen peroxide contents,[187] amongst others. As such, the development of new sensors and the miniaturization of existing sensors, or the amount of a sample required to yield diagnostic information, is of great interest to the field of flexible bioelectronics.

Carbon-fiber based microelectrodes are particularly advantageous for bioelectronic sensors because of their light weight, high tensile strength and flexibility, and affordability.[61, 62, 188-192] Moreover, one-dimensional (1D) carbon nanomaterials, including fibers, tubes, wires and rods, exhibit extraordinary properties for sensing; namely efficient electron transport, high electrical conductivities, and large surface-to-volume ratios.[63, 158] A conventional strategy for fabricating 1D nanomaterials is electrospinning which can be used to produce larger-scale materials with a defined surface area and morphology.[193, 194] Introduction of other components into or on the surface of the carbon-fibers can further control their electrochemical characteristics and hence performance.[195, 196,65, 66, 197, 198] For instance, charge exchange between heteroatom dopants and the carbon framework has been shown to modulate electronic structure characteristics and affect catalytic performance.[68] Incorporation of nitrogen-containing functional groups, such as pyridinic and pyrrolic nitrogen, into the carbon matrix allows for the adsorption and immobilization of metal atoms or nanoparticles into the system and can be used to further tailor the material's characteristics.[67] Furthermore, N co-doped with other different heteroatoms, including N/B, N/P, N/S, N/F and N/O have been proven to exhibit improved reaction kinetics and catalytic activity.[11] For example previous experiments have shown that the covalent attachment of metal oxide nanoparticles onto a carbon matrix increases the conductivity and electrochemical activity of the composite system.[49]

Cobalt oxide is attractive as a sensor material because of its good chemical durability, promising surface structure for facilitating catalytic activity, and its ability to perform fast reversible redox reactions.[127, 199, 108] The utility of cobalt oxide for electrochemical sensing is often limited because of relatively poor capacitance and slow electron transfer kinetics,[51] however, previous studies have shown that the formation of hybridized cobalt-based nanomaterials with doping or composites with a heterointerface on conductive materials, such as carbon nanotubes,[200] carbon nanofibers,[158] and metal nanosheets,[167] can alleviate these issues. In addition, cobalt oxides are classified as a low toxic chemical substance with relatively good biocompatibility.[51, 201]

Dopamine is an essential neurotransmitter of the catecholamine family and plays a paramount role in regulating various physiological activities in the central nervous, renal, cardiovascular, and hormone systems.[57, 202] Changes in DA concentration and its spatial and temporal kinetics can indicate neurodegenerative disorders, such as Parkinson's disease and schizophrenia.[203, 204] Moreover, abnormal levels of DA, in either urine or blood, can indicate the presence of pheochromocytomas and paragangliomas, which are rare and imperceptible tumors arising in neural crest tissue.[53] Up to now, there are no effective serological test for Parkinson's diseases or schizophrenia. Therefore, the monitoring DA levels in the serum or bodily fluids offers merits for doctors to determine if a patient either has a neurotransmitter expressing tumor or is surreptitiously taking a neurotransmitter drug. Traditional methods for the detection of DA include, fluorescence spectroscopy,[205, 206] surface-enhanced Raman spectroscopy,[207] and high-performance liquid chromatography;[208] however, these approaches require sophisticated instruments, time-consuming analysis, appropriately trained technicians, and sophisticated preparation procedures,[52, 209] which can hinder wide-scale applicability. By contrast, electrochemical sensing of DA offers the potential for real-time, on-site, and *in situ* detection.[55, 210, 211] The coexistence of other reactive species, such as AA (ascorbic acid) and UA (uric acid), have similar redox properties to DA and can degrade sensor selectivity on unmodified electrodes. To account for interferents, these studies engineer the nanohybrid sensor with nitrogen dopants which introduces excess negative charge on the surface-active sites and inhibits detection of the negatively charged AA and UA.[202, 212]

In this study, electrospun carbon nanofibers (ECNFs) with uniformly distributed nitrogen-doped functional groups are used to guide electrodeposition of cobalt oxide; Co_3O_4@NECNFs. The studies presented herein demonstrate the rational design of a novel electrochemical sensor by integrating Co_3O_4 nanograins on nitrogen-doped, aligned, electrospun carbon nanofibers. The sensor exhibits superb catalytic performance towards the oxidation of DA and provides capability of *in-situ* real-time detection of DA from the living dopaminergic cells, pheochromocytoma (PC12). These findings illustrate the applicability of electrochemical biosensors as an implantable, portable, miniaturized, and point-of-care clinical diagnostic device in living tissues.

Materials and Methods

Materials and Instrumentation

A Carl Zeiss Auriga-BU FIB field-emission scanning electron microscopy (FESEM) was used to determine the topographies of the samples. The X -ray powder diffraction (XRD) patterns were recorded by an Agilent Technologies Oxford Gemini X-Ray Diffractometer equipped with a Cu-Kα radiation source (λ=0.15418 nm). The Raman spectra were collected using a Horiba XploRA One Raman Confocal Microscope System with a 785 nm laser as the excitation source. X-ray photoelectron spectroscopy (XPS) analysis was conducted on an XPS-ESCALAB Xi+ Thermo Scientific instrument using an Al K-α radiation source. The binding energies of spectra were calibrated to a C1s peak at 284.6 eV. Ultraviolet photoelectron spectroscopy (UPS) measurements were performed using an ESCALAB 250XI XPS instrument with a He(I) discharge lamp. A -5.0 V bias was applied to the stage and a pass energy of 3.5 eV was used during collection. All electrochemical experiments were carried out using a Bio-Logic VMP3 electrochemical workstation, with a conventional three-electrode system. Electrodeposition, cyclic voltammetry (CV), chronoamperometry (CA), electrochemical impedance spectroscopy (EIS), and differential pulse voltammetry (DPV) measurements were performed using the electrochemical workstation. A 0.1 M phosphate buffer solution (Invitrogen) at pH 7.4 was used as the supporting electrolyte, unless otherwise specified. All solutions were prepared using deionized (DI) water and deoxygenated by bubbling with nitrogen for 20 min before performing DA electrocatalytic measurements.

Fabrication Electrospun Carbon Nanofibers (ECNFs)

An electrospinning method was used to fabricate the pristine well-aligned ECNFs using a polymer solution of 10 wt.% polyacrylonitrile (PAN, MW=150,000, ACROS Organics) in *N*,*N*-dimethylformamide (DMF, Sigma Aldrich). A self-designed sample collector, with four steel poles welded on a plate, was employed to collect the ECNFs without any substrates, which was according to our previously reported method and process.[48, 135, 152] A high voltage of 18 kV was applied between the needle and the collector, which was located 15 cm apart from each other. During the electrospinning, the collector was maintained at a rate of 2000 revolutions per minute, while the ECNFs precursor was fed at a rate of 1 mL h^{-1} for five hours using a syringe pump. The PAN sheets were then put into a furnace (Oxidation and Annealing Furnace) for stabilizing the formation of graphitic carbon structure. The heating rate was 1 °C min^{-1} from room temperature to 280 °C and then kept for 6 h in air. Next, the stabilized nanofibers were carbonized at a ramping rate of 5 °C min^{-1} up to 1200 °C for 1h under a nitrogen atmosphere to yield high mechanical strength well-aligned ECNFs.

Preparation of Co_3O_4@NECNFs

Following fabrication of the pristine ECNFs, the material was activated by immersion in 8 M nitric acid solution (HNO_3, J.T. Baker) for 2 h to promote the nitrogen-doping. The activated ECNFs (AECNFs) were placed in a Teflon autoclave reactor (50 mL volume, PPL-lined vessel chamber kettle, 250 °C), filled with 25 ml of 1 M ammonia solution (Sigma Aldrich), and heated at 180 °C for 5 h to dope the ECNFs with nitrogen (NECNF). The NECNFs were then rinsed with DI water and dried using nitrogen gas. The nitrogen doping was confirmed using XPS; see Fig. S4.1 for survey spectra upon doping. Cobalt oxide was then electrodeposited onto a 1 cm^2 NECNF substrate using a three-electrode configuration at a constant current of 55 μA for either 2 hours or 4 hours. To apply the potential to the NECNFs a gold electrode was used as a base and the NECNFs were taped on top. An aqueous solution containing 40 mM $CoSO_4$ (ACROS Organics) and 100 mM $NaSO_4$ (ACROS Organics) under a nitrogen atmosphere was used as the electrodeposition solution. The obtained nanohybrids, Co_3O_4@NECNFs, were then rinsed with DI water and dried at 80 °C for 3 hours.

Electrochemical Characterization and Measurement

A Bio-Logic VMP3 electrochemical workstation was used to carry out all these electrochemical characterization and measurement with a three-electrode system. The above prepared Co_3O_4@NECNFs electrode was cut into appropriate size in to flake morphology. The working electrode was a 5 mm × 5 mm Co_3O_4@NECNFs flake taped onto a glassy carbon electrode using conducing carbon glue (TED PELLA, INC), Ag/AgCl was used as the reference electrode, and platinum wire was used as the counter electrode. CV and EIS measurements were carried out to record the electrochemical performance of the nanohybrid electrode in 5 mM $[Fe(CN_6)]^{3-/4-}$ containing 0.1 M KCl solution. DPV and CA methods were performed to detect analyte of DA. Electrochemical monitoring DA was conducted in the three-electrode system containing 0.1 M PBS (pH = 7.4) with high purity nitrogen bubbling for 20 min.

Cell Cultivation

The PC12 cell line was selected to investigate regulated neurotransmitter secretion from neurons and was obtained from American Type Culture Collection (ATCC®CRL-1721™). The cells were cultured in optimized Dulbecco's Modified Eagle's Medium (DMEM, ATCC®30-2002™) supplemented with 10% horse serum (Sigma Aldrich), 5% fetal bovine serum (Sigma Aldrich), and 1% streptomycin-penicillin (Fisher Scientific), respectively. Cells were grown in a humidified incubator with 5 % CO_2 at 37 °C and passaged the cells twice a week. All experiments were performed on cells between passage 15 and 25.

Cytotoxicity Quantitative Test

The cytotoxicity of the Co_3O_4@NECNFs nanohybrid electrodes was investigated by a standard Cell Counting Kit-8 (CCK-8) assay. The cells (2×10^5 cell/mL) were seeded onto a 96-well plate with a total volume of 100 μL/well and maintained under a 5% CO_2 incubator at 37 °C for 24 h. The modified NECNF nanohybrids were sterilized in 70% ethanol in Petri dishes for 10 min, thereafter, most of the ethanol was removed by evaporating for 20 min. Then, the samples were cut into an appropriate size and pre-wetted with cell culture medium for approximately 10 min prior to transfer to the middle of the seeding well plate for several hours. The 10 µL CCK-8 solution (Sigma Aldrich) was added into each well and incubated for 2 h in the CO_2 incubator. The viability measurements of the cells were carried out by measuring the absorbance at 450 nm using a microplate reader (Bio Tek Microplate reader).

Fluorescence Staining and Cell Imaging

To further evaluate the biocompatibility of the Co_3O_4@NECNFs nanohybrids, the PC12 cells, at a density of 1.7×10^6 cells/mL, were seeded onto the nanohybrid and placed in the middle of a confocal dish where the surface of the sample was coated with 0.1 mg/ml poly D-lysine solution (Sigma Aldrich). The cells were then co-inoculated with the presence of the nanohybrid composite which was placed on a confocal dish containing a cell culture medium volume of 300 µL. Next, the confocal dish was placed into an incubator for 24 h and the growth medium was replaced with live/dead cell dye solution, composed of calcein AM (1 µL) and ethidium homodimer-1 (4 µL) dissolved in 2 mL sterilized phosphate buffer saline. Following 20 min of incubation the stained cells were then imaged under a confocal microscope (Zeiss Z1 Spinning Disk Confocal Microscope) at 20× magnification. The live cells uptake calcein AM and were stained green, which was observed with the FITC channel, whereas dead cells uptake ethidium homodimer-1 and were stained in red, observed by the RHOD channel.

Real-Time in situ Electrochemical Detection of DA Secreted by Living Cells

Previous studies have shown that a high concentration of potassium stimulates membrane depolarization of the PC12 cells and causes the secretion of DA by exocytosis.[56, 59] The spikes of DA oxidation occur with a latency less than 1 second after membrane depolarization from the high extracellular potassium concentration and the peak current decreased upon successive stimulation due to the depletion of cellular DA stores.[55] It is assumed that the *in situ* detected peak current, originating from released DA, depends critically on the number of cells in the system and the diffusion distance between the cells and the electrode.[55] To account for the diffusion, the Co_3O_4@NECNFs electrode was placed near living cells and chronoamperometric methods were carried out under 0.3 V to record the current response of DA secreted by PC cells, where potassium chloride (120 mM) was injected into 7 mL 0.1 M PBS (pH 7.4) containing 8×10^6 cells, determined by an TC20^{TM} automated cell counter device (Bio-Rad).[184]

Results and Discussion

Nucleation and Characterization of the Co_3O_4@NECNFs Nanohybrid Electrode Materials

Theoretical calculations on nanocarbon materials with dopants indicate that synergistic effects between the dopants and scaffold can lead to stronger binding strength of metal ions for nucleation and growth.[64] The nucleation of cobalt oxide on the NECNFs has been shown previously to occur through the formation of C-O-metal and C-N-metal bonds between the NENCFs and cobalt atoms.[49] The surface chemical oxidation of the pristine ECNFs using nitric acid activates AECNFs with increased defects from O dopants. Fig S4.2 shows C1s and O1s XPS spectra of the AECNFs and indicate that the surface comprises carboxyl, ether, and hydroxyl groups. Those oxygen-containing functional groups can not only modify the electronic configuration of the carbon framework with more hydrophilicity, but also provide media to interact with other catalysts, such as the subsequent heteroatom dopants and metal ions.[11] Upon treatment of the AECNFs with ammonia (see methods for more details), the nitrogen adheres to the defect sites and the ECNFs become N-doped (NECNF). Figure 4.1a shows high-resolution N1s XPS spectra of the NECFNS. The spectra were fit to a sum of three characteristic peaks and are associated with graphitic nitrogen (gN, blue), pyrrolic nitrogen (rN, green), and pyridinic nitrogen (pN, orange); see SI for details on the peak fitting and stoichiometry in Table S4.1. Additionally, C1s and O1s spectra in Fig. S4.3 indicate that the surface functional groups found in the AECNFs, (carboxyls, ethers, and hydroxyls) persist upon N-doping.

The role of N and O doping in the nucleation and subsequent growth of cobalt oxide during electrodeposition is suspected to occur in an analogous manner to other works.[67, 193, 213, 214] The extra electron density, arising from the rN, gN, and the lone pair on pN, act as electron donors to the ECNF π-system and as Lewis base sites which couple strongly to the acidic cobalt ions from solution.[67,68,64] Moreover, the oxygen containing surface functional groups can act as binding sites which further facilitate cobalt electrodeposition and growth. The degree of surface modification for the different treatments was determined using Raman spectroscopy. Figure 4.1b shows Raman spectra for the ECNFs (black), AECNFs (red), and NECNFs (blue) samples. Two characteristic peaks are observed at ~1350 cm^{-1} and 1580 cm^{-1} and are assigned to the D band and G band, respectively. Previous reports have attributed the G band to in-plane carbon-carbon stretching modes consistent with a graphitic structure and the D band to defects and disorder in the carbon nanofiber.[213] Therefore the intensity ratio of the two bands (I_D/I_G) indicates a relative amount of defects for the material. An intensity ratio 0.93, 1.01, and 1.05 was found for the ECNFs, AECNFs, and NECNFs respectively and indicates that successive treatments cause an increase in defect sites. These findings are further corroborated by XRD studies; see Fig. S4.4 for more details. The emergence of more defects sites aids in the nucleation and subsequent growth of cobalt oxide and correlates with an enhancement of the electrochemical performance, *vide infra*.

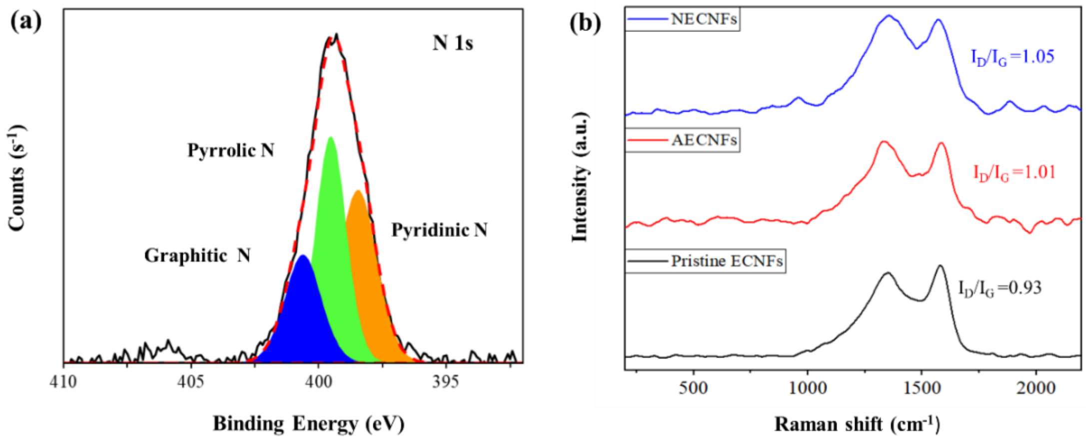

Figure 4.1 XPS and Ramam Spectra: (a) High-resolution N1s XPS spectra of N-doped CNFs. (b) Raman spectra of pristine ECNFs, AECNFs and NECNFs.

Because doping and functionalization of the carbon framework affects the surface electron distribution, and subsequently the band gap, surface affinity, and catalytic properties,[215] an appropriate characterization of the electronic structure was necessary.

Work function measurements, corresponding to the energy required to remove an electron from the Fermi level to vacuum, were employed using ultraviolet photoemission spectroscopy (UPS) and are shown in Fig. S4.5. The work function of ENCFs, AECNFs, and NECNFs were found to be 4.6, 4.5, and 3.8 eV, respectively. The stark difference in work function upon N-doping indicates that a change in the charge density and electronic structure occurs and most likely arises from dipolar contributions and electron donation to the graphitic lattice.[216] The decrease in work function is expected to play a role in facilitating electron transfer for both nucleation of the cobalt oxide and in electrocatalytic applications.

The surface morphology of the carbon nanofiber nanohybrids was characterized by field-emission scanning electron microscopy (FE-SEM). Figure 4.2a and d show the smooth surface structure with well-aligned orientation of the NECNFs. Electrodeposition of cobalt oxide was then performed at a fixed current density of 55 μA cm^{-2} yielding the designed Co_3O_4@NECNFs nanohybrid materials. Following 2 hours of electrodeposition, nucleation, and the uniform growth of spherical cobalt oxide nanograins appear on the surface with an average nanograin size of 162 ± 25 nm; see Figure 4.2b & e and Fig. S4.6. Upon further electrodeposition time, 4 hours, the nanograins grow in size to 350 ± 75 nm (Figure 4.2c & f and Fig. S4.6). Introduction of heteroatom with nitrogen dopant and oxygen-containing functional groups in the carbon skeleton play key roles in the formation of the three-dimensional nanostructures. Such three-dimensional cobalt oxide nanostructures have high surface area, leading to increased numbers of exposed active sites, good contact electrolytes and enhanced ion/charge transport and diffusion in electrochemical sensing.[217] Control experiments for the electrodeposition of cobalt oxide on AECNFs are shown in Fig. S4.7. It shows much more monolithic features, owing to the lack of nitrogen sites for the nucleation and growth of nanograins. The implantation of nitrogen atoms and N-containing functional groups offers abundant binding sites and strong coupling to anchor with cobalt ions and it is favorable for the *in situ* nucleation and growth of cobalt oxide nanomaterials.[51] The nitrogen-containing and oxygen-containing functional groups on the surface of ECNFs can trap delocalized electron around the defect sites; and those trapped charges further promote the reactions. [214, 218] The positively charged cobalt ions then absorb onto the surface of ECNFs, where the absorbed substances act as preferential nucleation sites for *in situ* growth of larger crystals.

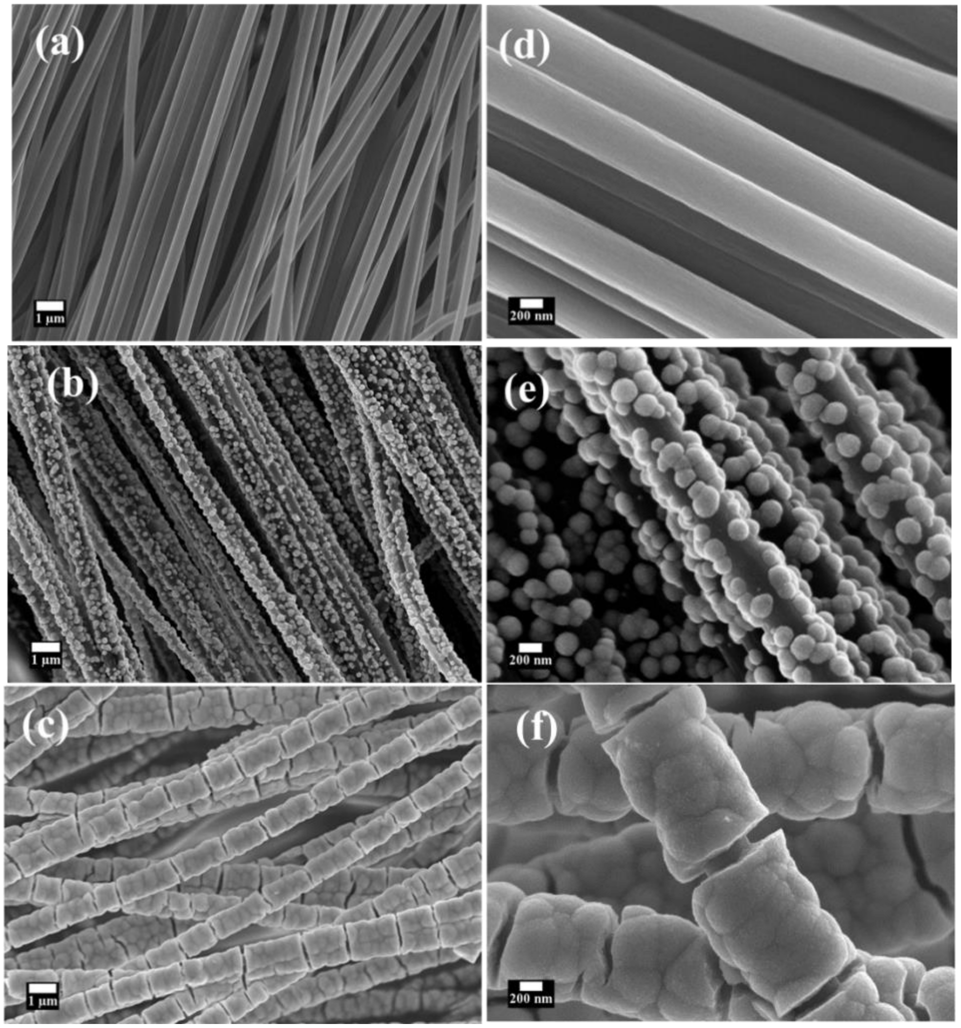

Figure 4.2 SEM images: low- (a) and high-magnification (d) well aligned ECNFs, Co_3O_4@NECNFs following 2h electrodeposition under low- (b) and high-magnification (e), Co_3O_4@NECNFs following 4h electrodeposition under low- (c) and high-magnification (f).

Figure 4.3a shows XPS survey spectra of the NECNFs before (black) and after 2 hours (blue) and 4 hours (red) of cobalt oxide electrodeposition. The N1s photoelectrons are preferentially attenuated in the two samples following electrodeposition presumably because the cobalt oxide tends to grow at these sites. Figure 4.3b shows the Co 2p core-level XPS spectra for the two different electrodeposition times. Both spectra display two main peaks located at 781.4 and 796.7 eV, corresponding to the $Co2p_{3/2}$ and $Co2p_{1/2}$ peaks, respectively, with a spin-orbit splitting of 15.3 eV.[219] To gain further insight into the oxidation state of the Co atoms, the doublet peaks were fit to a weighted sum of the two prominent peaks in reference spectra of Co^{2+} and Co^{3+}, located at 781.8 and 779.9 eV for $Co2p_{3/2}$, and at 797.4 and 795.7 eV for $Co2p_{1/2}$, respectively.[166, 220]

Figure 4.3c shows high resolution O1s XPS spectra for 2-hour (2h) Co_3O_4@NECNFs (blue), and 4-hour (4h) Co_3O_4@NECNFs (red). For NECNFs two main peaks are observed; Ox at 531.5 eV which corresponds to surface oxygen vacancies and/or oxygen-containing groups[221] and Oy at 533.2 eV associated with chemically or physically absorbed water molecules.[219] Upon electrodeposition a new peak emerges at 529.6 eV, labeled Oz, and arises from a metal-oxygen bond.[167] Raman spectroscopy was performed to further characterize the microstructure of the cobalt oxide nanoparticles on the surface of the NECNFs; Figure 4.3d shows the emergence of four Raman bands on 2h Co_3O_4@NECNFs (blue) and 4h Co_3O_4@NECNFs (red) compared to the bare NECNFs (Figure 4.1b). The peaks at 460, 508, 604 and 663 cm^{-1} are consistent with the reported values of E_g, F^2_{2g}, F^3_{2g}, and A_{1g} modes of crystalline Co_3O_4.[218, 222-224] The D band and G band peaks of the NECNFs are concomitant with these Raman bands from crystalline Co_3O_4, indicating a successful combination of carbon matrix with the metal oxide nanoparticles.

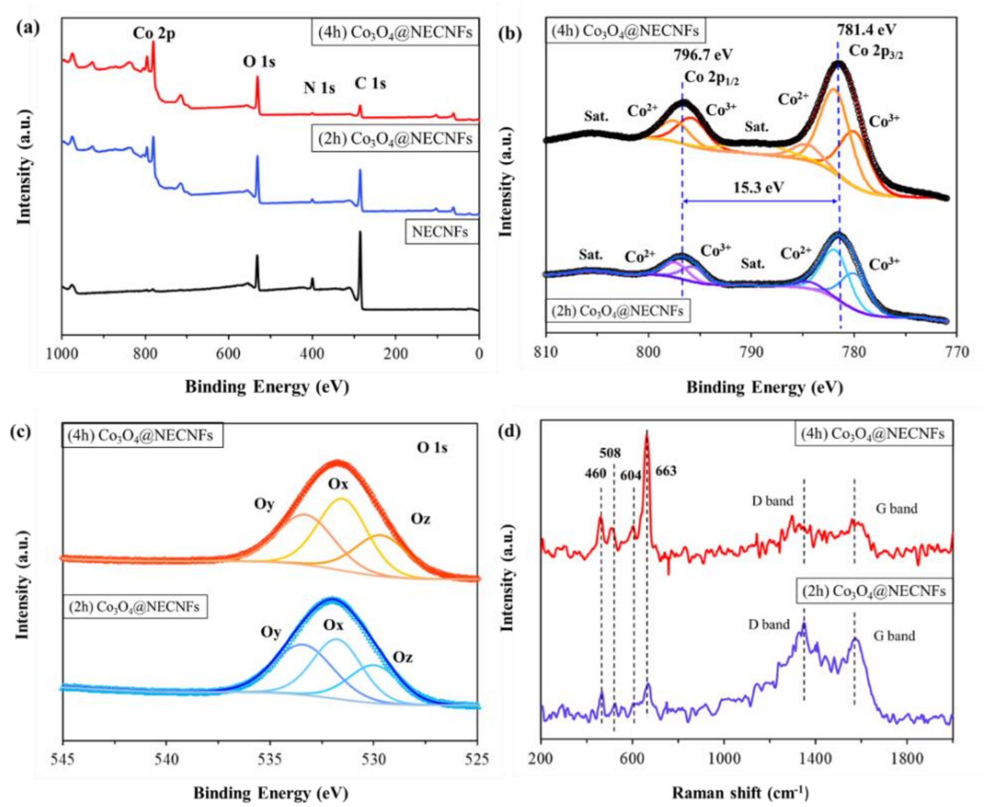

Figure 4.3 XPS and Raman Spectra: XPS survey spectra (a) Co2p spectra (b), O1s spectra (c), and Raman spectra (d) of NECNFs (black), 2 hour Co_3O_4@NECNFs (blue) and 4 hour Co_3O_4@NECNFs (red).

Electrochemical Characterization of the Co_3O_4@NECNFs Nanohybrid Electrode Materials

Figure 4．4a shows cyclic voltammetry (CV) measurements of glassy carbon (GCE, black), NENCFs (green), 2h Co_3O_4@NECNFs (blue), and 4h Co_3O_4@NECNFs (red) using a standard redox couple; ferri- ferrocyanide. Interestingly, an increase in current was observed for NECNF substrates upon electrodeposition of cobalt oxide, with the 4h Co_3O_4@NECNFs exhibiting the highest peak current, owing to striking ion/charge transport and diffusion applicability, and higher electrochemical active surface area. In addition to the change in peak current, a significant decrease in the anodic and cathodic peak separation, ~150 mV, is observed for samples with electrodeposited cobalt oxide and is concomitant with an increase in the electron transfer rate. Electrochemical impedance spectroscopy (EIS) was used to further explore the electrochemical kinetics occurring at the electrode surface / solution interface. Figure 4.4b shows Nyquist plots of a bare GCE (black), NECNFs (green), 2 hour Co_3O_4@NECNFs (blue), and 4 hour Co_3O_4@NECNFs (red). For bare GCE and NECNFs electrodes only one semicircle at high frequency is observed and corresponds to a charge-transfer resistance (R_{ct}) of 332 Ω and 139 Ω, respectively. For the Co_3O_4@NECNFs, two semicircles are observed; the high-frequency semicircle arises from electrolyte resistance (R_∞), while the low-frequency semicircle is associated with the sum of charge transfer resistance and/or mass transfer resistance (R_{mt}).[225] The decrease in resistance for the R_{ct}/R_{mt} for 2 hour Co_3O_4@NECNFs (89 Ω) and 4 hour Co_3O_4@NECNFs R_{ct}/R_{mt} (35 Ω) compared to NECNFs indicates that cobalt oxide acts to facilitate charge transport and separation.[158], which is in accordance with the previous report.[200] The excellent electrochemical performance can be largely ascribed to the carbon layer between the cobalt oxide nanostructures, which acts as conductive supports to reduce the inner resistance, and enhanced electrical conductivity.[226]

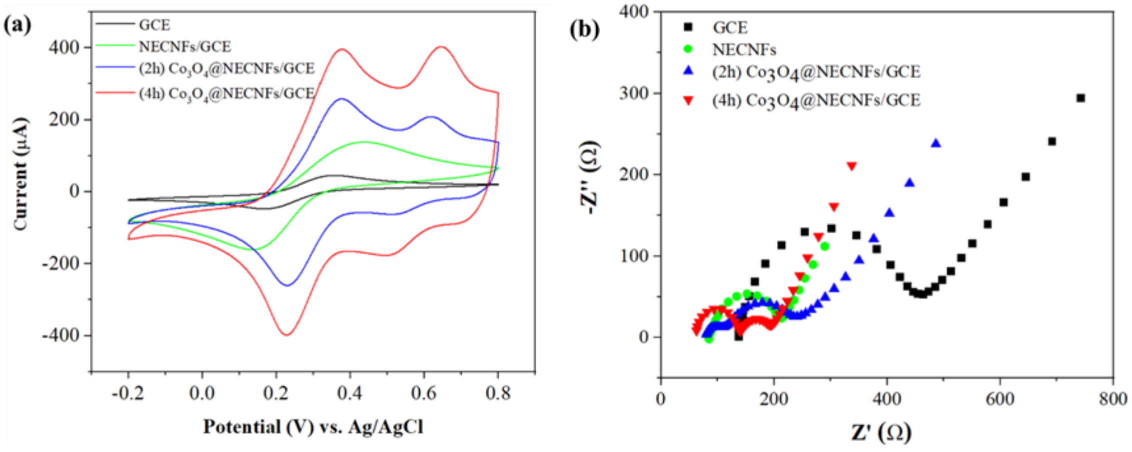

Figure 4.4 Electrochemical Characterization: (a) Cyclic voltammetry measurements of 5 mM $[Fe(CN)_6]^{3-/4-}$ in 0.1 M KCl at a scan rate of 20 mV/s using GCE (black), NENCFs (green), 2h Co_3O_4@NECNFs (blue), and 4h Co_3O_4@NECNFs (red) electrodes. (b) Nyquist plots of GCE (black) NENCFs (green), 2h Co_3O_4@NECNFs (blue), and 4h Co_3O_4@NECNFs (red) electrodes.

Electrocatalytic Oxidation of DA on Nanohybrid Electrode

Figure 4.5a shows cyclic voltammetry measurements of bare GCE (black), NECNFs (green), and Co_3O_4@NECNFs with 2 hour (blue) and 4 hour (red) electrodeposition in the presence of 0.1 mM DA in a 0.1 M PBS (pH 7.4) solution. Peak current analysis of the different electrodes is shown in Fig. S4.8. The 4h Co_3O_4@NECNFs exhibits higher peak current and indicates improved electrocatalytic activity compared to the other electrodes. The unique effect is attributed to the synergy between the remarkable catalytic activity of the cobalt oxide nanograins and the nitrogen dopants in the carbon matrix with highly conductive and high surface area that promote efficient electron transfer to the electrode. To further explore the electrocatalytic kinetics of DA oxidation on the 4h Co_3O_4@NECNFs, cyclic voltammetry measurements were measured for different scan rates (50 to 350 mVs^{-1}); see Fig. S4.9a. A linear relationship is shown in Fig. S4.9b for the oxidation and reduction peak currents with scan rate and indicates that adsorption of DA is followed by a surface-confined electrochemical reaction.[56, 210] For a comparison, experiments with cobalt oxide decorated onto AECNFs (4h Co_3O_4@AECNFs) for electrocatalytic kinetics of DA were further analyzed in Fig. S4.10. Linear relationship between peak currents and scan rate with gently slope (~66%) compared with 4h Co_3O_4@NECNFs, indicating slower reaction kinetics. Figure 4.5b shows differential pulse voltammetry measurements used to determine the limit of detection (LOD) of DA for the 4h Co_3O_4@NECNFs electrodes. The concentration of DA was varied between 50 nM to 100 µM in and the corresponding change is used to form a calibration curve (Figure 5C). The LOD for was determined using the following equation [56]

$$LOD = 3Sd/S \qquad \text{(4-1)}$$

where Sd represents the standard deviation of the blank signals (n=3) and S is the slope of calibration plot.

For the 4 hour Co_3O_4@NECNFs electrode the LOD for DA was 20 nM which represents a relatively low LOD and wide dynamic linear range compared to other electrochemical sensors. See Table S4.2 for comparison of electrochemical sensors from this and other works.

Because of the endogenous interference of ascorbic acid (AA) and uric acid (UA) with DA, arising from a similar oxidation potential, the selectivity of the electrochemical sensor was also assessed. Those interferents in biological fluids coexist with DA in high concentration levels. Generally, DA ranges from 0.01 to 1 µM and the AA of a few tens µM up to 500 µM in the extracellular fluid of the central nervous system or blood plasma.[227, 228] Therefore, it’s necessary to test the detection of DA in the presence of higher AA and UA concentration for selectivity. Figure 4.5 d shows voltammograms for the UA (40µM, blue line) and AA (40µM, orange line) interferents and the current responses of UA and AA are negligible when detecting DA at 10µM, (pink dotted line). The superior selectivity is attributed to the nitrogen dopants in the carbon matrix which make the surface charge more negative. Therefore, the substrate preferentially adsorbs the positively charged DA and repels the negatively charged UA and AA. To probe the fidelity and stability of the sensor, eight independently prepared sensors were compared and the electrocatalytic activity was measured over the course of a month. Fig. S4.11 shows that the relative standard deviation was 2.3% among the different electrodes and that only modest degradation occurred with time; ~95% of the activity was retained. Additional studies showing the voltammetric and chronoamperometric response of the sensor to DA concentration in human serum are shown in Fig. S4.11 and Table S4.3, respectively. The nanohybrid electrochemical sensor displayed the recoveries ranging from 99.6 to 101.7% with the RSD of 1.1 to 1.9% in human serum.

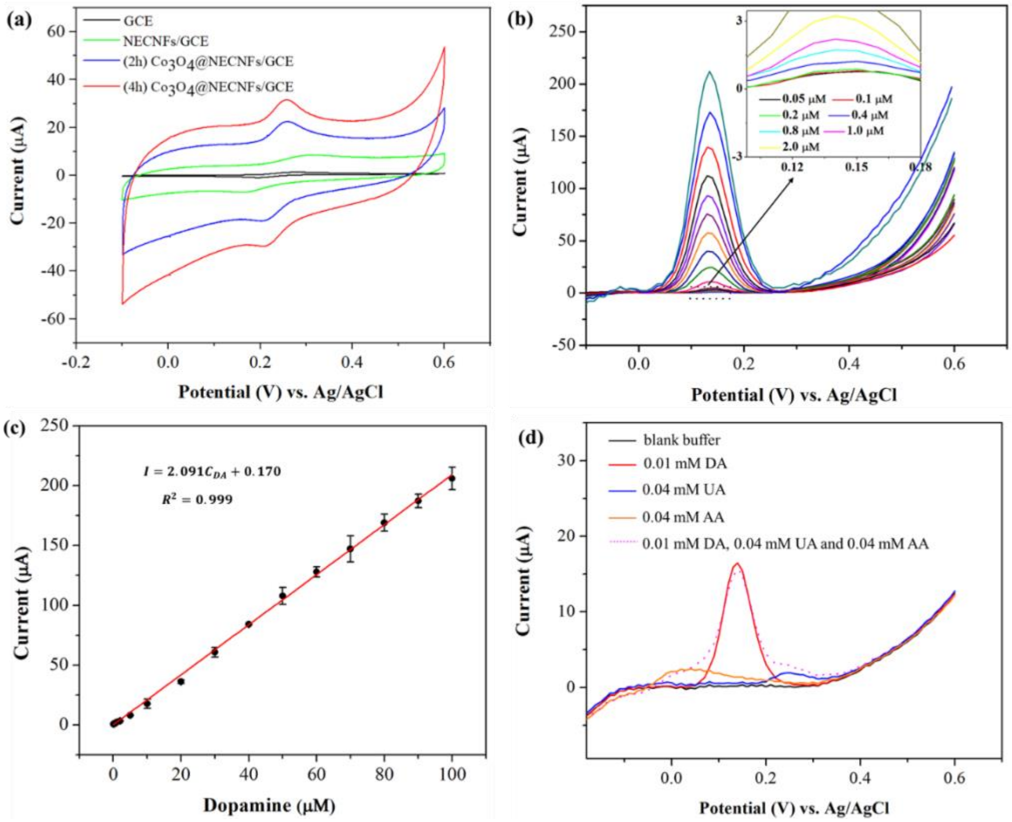

Figure 4.5 Cyclic Voltammograms and Differential Pulse Voltammograms: (a) CV curves of 0.1 mM DA in 0.1 M PBS (pH 7.4) solutions using GCE (black), NECNF (green), 2 hour Co_3O_4@NECNFs (blue), and 4 hour Co_3O_4@NECNFs (red) electrodes at a scan rate of 50 mV/s. (b) DPV measurements of the 4h Co_3O_4@NECNFs electrode with a varied DA concentration (0.05 to 100 µM). (c) Calibration curve of the peak current of the 4h Co_3O_4@NECNFs electrode with corresponding DA concentration. (d) DPV curves of the 4h Co_3O_4@NECNFs electrode for detection of 0.01 mM DA (red, line), 0.04 mM UA (blue, line), and 0.04 mM AA (orange, line) separately and together (pink dotted line).

Real-Time in situ Electrochemical Determination of DA Secreted by PC-12 Cells

The feasibility of the nanohybrid electrode for monitoring the release of DA from living cells was then tested. First, the biocompatibility was determined by performing a cell viability test, CCK-8 using the 4 hour Co_3O_4@NECNFs electrodes and living PC 12 cells. Following co-culturing of the cells and the electrode for 8 hours, the cells still exhibited good activity, and thus indicate excellent biocompatibility (see Figure 4.6a). A live/dead staining assay further corroborates the assay results. Figure 4.6 b shows the evolution of alive (green) and dead (red) PC12 cells dispersed on the Co_3O_4@NECNFs electrode after 24 hours, 48 hours, and 72 hours. The PC12 cells tended to aggregate together and the number of viable cells declined after 72 hours, however good biological activity is shown up to 48 hours. Though there is rare investigation of low-solubility compounds of cobalt oxides particles in toxicological studies, less-soluble cobalt oxide nanoparticles have shown less toxic than cobalt ions, exhibiting a low toxicity in vitro.[229, 230] Ortega et al. reported the cobalt oxide nanoparticles with much lower toxicity than that induced by soluble cobalt chloride with 72 h exposure time, and also demonstrated the toxicity at 72 h is higher than after 24 h exposure, both of which are good in accordance with our biocompatibility results.[229] Next, the real-time *in situ* amperometric response of DA secreted from living cells was monitored (Figure 4.6c). The addition of a high concentration of K^+ depolarizes the PC12 cells and induce the release of DA by exocytosis.[231, 232] Upon addition of KCl a current response is observed for samples containing PC12 cells (red), whereas such a response is not observed if cells are not present (blue). The concentration of secreted DA was calculated by matching the current value with the obtained calibration curve in Fig. S4.12 and found to be 0.14 μM, or approximately 1.7×10^{-8} μM per cells. The expected levels of physiological DA in the human plasma is 0.23 μM, and that in the human brain is in the range of 0.02-0.2 μA.[52] In this work, the nanohybrid electrode exhibits with a high sensitivity of 20 nM, capable of detecting the concentration levels of DA in plasma and human brain. These results indicate that the Co_3O_4@NECNFs electrode can be used to determine DA released from living cells, and thus represent promise for electrochemical detection in early clinic diagnosis of a living body.

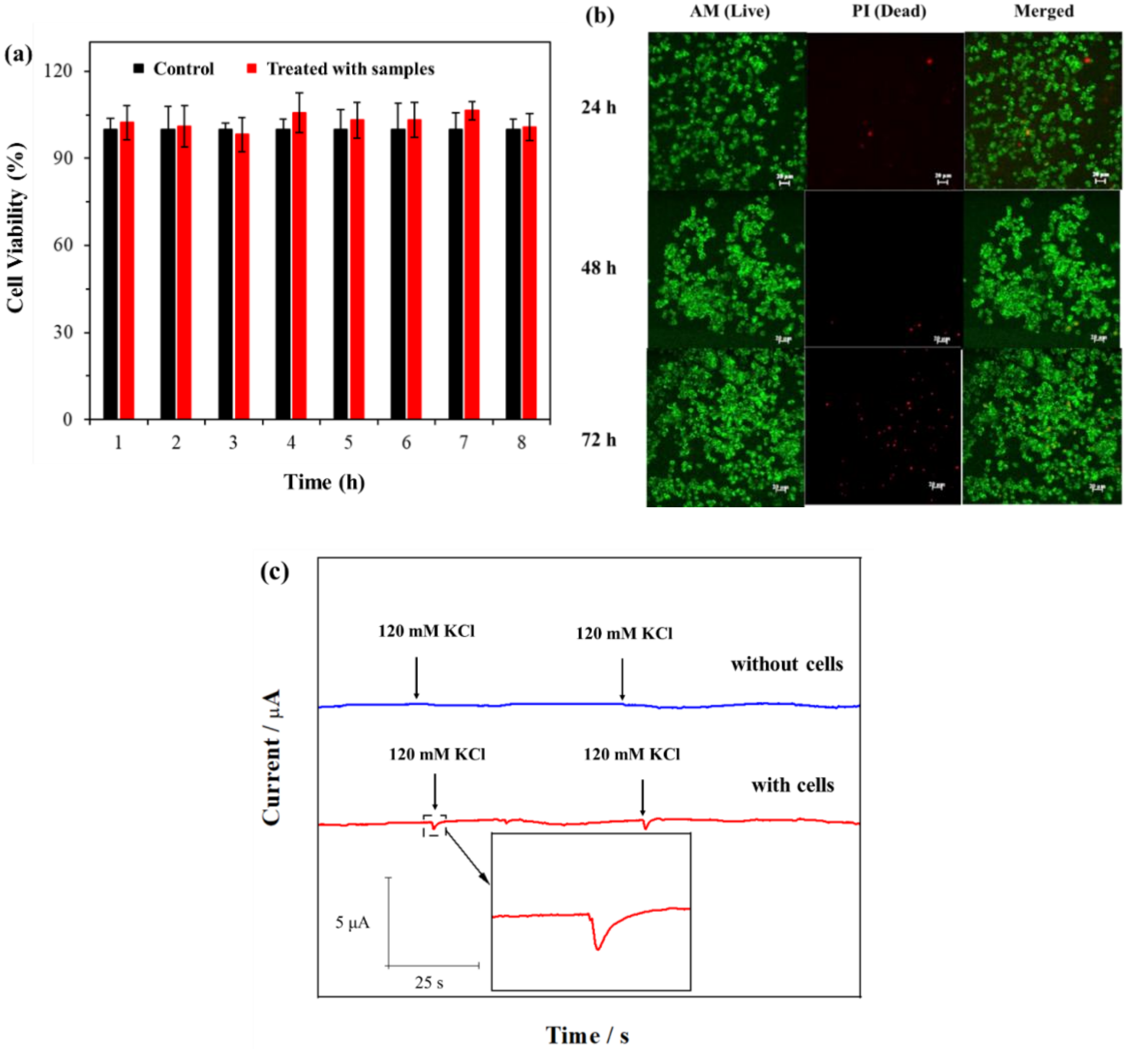

Figure 4.6 Cell Viability Test and Amperometric Test: (a) CCK-8 assay for cytotoxicity of 4h Co_3O_4@NECNFs after co-culturing with PC12 cells for several hours. (b) Fluorescence images of live (green) and dead (red) stained PC12 cells cultured on the 4h Co_3O_4@NECNFs for 24, 48, and 72 hours. (c) Amperometric responses of the 4h Co_3O_4@NECNFs electrode with (red) and without (blue) PC12 cells in 0.1 M PBS upon addition of 120 mM KCl.

Conclusion

This work presents a design for the fabrication of Co_3O_4 nanograin structures at the aligned ECNFs scaffold via pretreatment of N-dopants. The Co_3O_4@NECNFs electrode was tested as an electrochemical sensor for dopamine analysis. The Co_3O_4@NECNFs electrode demonstrates high sensitivity over a wide range of concentrations (0.05 to 100 μM) with an excellent limit of detection (20 nM) and remarkable selectivity against interferents. The positive attributes arise from the synergistic effects of the N-doped carbon nanofibers and the cobalt oxide. The N-doping affords nucleation sites for cobalt oxide growth during the low-current electrodeposition process and makes the electrode surface more negatively charged, leading to a greater selectivity, whereas the cobalt oxide acts as the catalytic site. The electrochemical sensors exhibit good biocompatibility over 48 hours in cells and is capable for real-time detection of DA secreted from PC12 living cells with response time in one second. More broadly, these studies direct to strategies for using dopants to control surface properties and enhance selectivity of flexible bioelectronics or devices for point-of-care early clinical diagnostics.

CHAPTER V

CONCLUSIONS

In Chapter II, the direct electrochemcistry and kinetics for redox active centers of glucose oxidase (GOx) was investigated by cyclic voltammetry (CV) with the presence of glucose, in virtue of the nanohybrid, a single-wall carbon nanotubes (SWCNTs)-poly(ethylenimine) (PEI) matrix. The Faradaic current of the GOx in CV decreases when the concentration of glucose increases, while the calculated electron transfer (ET) rate constant (k^0) of the GOx presents a monotonic increment mannner up to 144 % at 70 m M glucose concentration vs. absence of glucose under a deaerated electrolyte solution. In addtion, the k^0 and Faradiac current changes demonstrate a strong linear dependence to logarithmic value of gludose concentration up to 20 mM. These results suggest that the entrapped GOx, when exposing to glucose, become deactivated in the direct electrochemistry. Futher mechanistic analysis has shed light on the ET reaction of GOx shows a responsive correlation to the non-ergodicity of those active GOx sites. This finding may offer great significance and potential for the convergence of hybrid materials based on carbon nanotubes and nature proteins aiming at developing reagentless or mediator free glucose electronic devices.

Chapter III demonstrates a nanohybrid electrode based on uniformly mingled nanostructures of Co_3O_4 and MnO_2 deposited on a well-aligned electrospun carbon nanofibers (WA-ECNFs) mat for rapid glucose oxidation and sensing. The hybridization of Co_3O_4 and MnO_2 is synthesized by a simple one-step and template-free electrodeposition technique with a constant low-current at 60 μA for 3h at room temperature in an aqueous solution. The binary MnO_2/Co_3O_4@WA-ECNFs nano-matrix electrode exhibits excellent uniformity with high porosity, increased electrochemical active surface areas, conductivity and fast charge transfer, and improved efficiency for glucose electrooxidation in comparison to the monometallic MnO_2 or Co_3O_4 at the WA-ECNFs. The MnO_2/Co_3O_4@ECNF electrode shows superior sensing characteristics including a rapid glucose oxidation response within 5 seconds, a wide range detection from 5 μM to 10.9 mM, an excellent sensitivity of 1159 μA mM^{-1} cm^{-2}, and a detection limit of 0.3 μM (S/N=3) with satisfactory selectivity, great reproducibility and stability. These compelling results have shed light on the synergetic effect of the hybrid materials based on carbon nanofiber and metal oxides with multifunction in both morphology and catalytic activity , which would provide the broader research community great opportunities for electronic device in state-of-the-art application.

In Chapter IV, a new hybrid flexible electrochemical sensor has been created by decorating closely packed cobalt oxide (Co_3O_4) nanograins on nitrogen doped electrospun carbon nanofibers (NECNFs), where the Co_3O_4 nanograins uniformly distributed is maximized. Taking advantages of heteroatom dopants in the carbon skeleton and superior electrocatalytic activity of cobalt oxide, the performance and characteristics of the electrochemical sensor achieved a completely new level. In addition, the real-time detection of DA released from pheochromocytoma (PC12) cells by highly concentrated K^+ stimulation was also recorded by the flexible sensor, enabling the novel sensor to provide a facile application in early point-of care clinic diagnosis. Therefore, the contribution presented here will help serve the materials and biosensor communities promising hints in transitioning towards novel point-of-care application.

The primary purpose of the whole project was to investigate state-of-the-art electrochemical application of hybrid materials based on carbon nanotubes and nanofibers, and to get a comprehensive understanding of the role electron transfer in the aspect of specific electrochemcial redox reaction. To this end, the compelling findings in this dissertation presented some advances in knowledge and technical methods for development of hybrid nanoelectrodes based on carbon materials as electrocatalysts and electrochemcial detection of biomolecules. Future work could further optimize electrocatalytic performance thorugh combined strategies of introducing high-level benefical doping heteroatoms and surface functional groups, building a nanostructured architecture with large surface area and unique morphology, as well as incorporating other active species and engineering their interface to accellerate charge transport and improve catalytic efficiency. For practical applications, continous efforts of the research communities should be made on exploring advanced application of hybrid materials and device engineering. It is highly likely to develop flexible hybrid materials-based point-of-care medical electronic devices for real world application.

REFERENCES

1. Laurila, T.; Sainio, S.; Caro, M. A., Hybrid carbon based nanomaterials for electrochemical detection of biomolecules. *Progress in Materials Science* **2017,** *88*, 499-594.

2. George, J. M.; Antony, A.; Mathew, B., Metal oxide nanoparticles in electrochemical sensing and biosensing: a review. *Microchimica Acta* **2018,** *185* (7), 1-26.

3. Tao, H.; Fan, Q.; Ma, T.; Liu, S.; Gysling, H.; Texter, J.; Guo, F.; Sun, Z., Two-dimensional materials for energy conversion and storage. *Progress in Materials Science* **2020,** *111*, 100637.

4. Park, W.; Shin, H.; Choi, B.; Rhim, W.-K.; Na, K.; Han, D. K., Advanced hybrid nanomaterials for biomedical applications. *Progress in Materials Science* **2020**, 100686.

5. Wang, Y.; Guo, L.; Qi, P.; Liu, X.; Wei, G., Synthesis of three-dimensional graphene-based hybrid materials for water purification: A review. *Nanomaterials* **2019,** *9* (8), 1123.

6. Faustini, M.; Nicole, L.; Ruiz-Hitzky, E.; Sanchez, C., History of organic–inorganic hybrid materials: prehistory, art, science, and advanced applications. *Advanced Functional Materials* **2018,** *28* (27), 1704158.

7. Gregorczyk, K.; Knez, M., Hybrid nanomaterials through molecular and atomic layer deposition: Top down, bottom up, and in-between approaches to new materials. *Progress in Materials Science* **2016,** *75*, 1-37.

8. Park, S. S.; Ha, C. S., Hollow mesoporous functional hybrid materials: Fascinating platforms for advanced applications. *Advanced Functional Materials* **2018,** *28* (27), 1703814.

9. Al Zoubi, W.; Kamil, M. P.; Fatimah, S.; Nashrah, N.; Ko, Y. G., Recent advances in hybrid organic-inorganic materials with spatial architecture for state-of-the-art applications. *Progress in Materials Science* **2020,** *112,* 100663.

10. Tang, X.; Liu, D.; Wang, Y.-J.; Cui, L.; Ignaszak, A.; Yu, Y.; Zhang, J., Research Advances in Biomass-Derived Nanostructured Carbons and Their Composite materials for Electrochemical Energy Technologies. *Progress in Materials Science* **2020**, 100770.

11. Wang, J.; Kong, H.; Zhang, J.; Hao, Y.; Shao, Z.; Ciucci, F., Carbon-based electrocatalysts for sustainable energy applications. *Progress in Materials Science* **2020**, 100717.

12. Martín, C.; Martín-Pacheco, A.; Naranjo, A.; Criado, A.; Merino, S.; Díez-Barra, E.; Herrero, M. A.; Vázquez, E., Graphene hybrid materials? The role of graphene materials in the final structure of hydrogels. *Nanoscale* **2019,** *11* (11), 4822-4830.

13. Soldano, C., Hybrid metal-based carbon nanotubes: Novel platform for multifunctional applications. *Progress in Materials Science* **2015,** *69,* 183-212.

14. Wicklein, B.; Diem, A. M.; Knöller, A.; Cavalcante, M. S.; Bergström, L.; Bill, J.; Burghard, Z., Dual-Fiber Approach toward Flexible Multifunctional Hybrid Materials. *Advanced Functional Materials* **2018,** *28* (27), 1704274.

15. Navrotskaya, A. G.; Aleksandrova, D. D.; Krivoshapkina, E. F.; Sillanpää, M.; Krivoshapkin, P. V., Hybrid materials based on carbon nanotubes and nanofibers for environmental applications. *Frontiers in Chemistry* **2020,** *8*.

16. Zebda, A.; Gondran, C.; Le Goff, A.; Holzinger, M.; Cinquin, P.; Cosnier, S., Mediatorless high-power glucose biofuel cells based on compressed carbon nanotube-enzyme electrodes. *Nature communications* **2011,** *2* (1), 1-6.

17. Deng, S.; Jian, G.; Lei, J.; Hu, Z.; Ju, H., A glucose biosensor based on direct electrochemistry of glucose oxidase immobilized on nitrogen-doped carbon nanotubes. *Biosensors and Bioelectronics* **2009,** *25* (2), 373-377.

18. Muguruma, H.; Iwasa, H.; Hidaka, H.; Hiratsuka, A.; Uzawa, H., Mediatorless direct electron transfer between flavin adenine dinucleotide-dependent glucose dehydrogenase and single-walled carbon nanotubes. *ACS Catalysis* **2017,** *7* (1), 725-734.

19. Xia, H.; Zeng, J., Rational Surface Modification of Carbon Nanomaterials for Improved Direct Electron Transfer-Type Bioelectrocatalysis of Redox Enzymes. *Catalysts* **2020,** *10* (12), 1447.

20. Wang, J., Electrochemical glucose biosensors. *Chemical reviews* **2008,** *108* (2), 814-825.

21. Degani, Y.; Heller, A., Direct electrical communication between chemically modified enzymes and metal electrodes. I. Electron transfer from glucose oxidase to metal electrodes via electron relays, bound covalently to the enzyme. *Journal of Physical Chemistry* **1987,** *91* (6), 1285-1289.

22. Holland, J. T.; Lau, C.; Brozik, S.; Atanassov, P.; Banta, S., Engineering of glucose oxidase for direct electron transfer via site-specific gold nanoparticle conjugation. *Journal of the American Chemical Society* **2011,** *133* (48), 19262-19265.

23. Blaik, R. A.; Lan, E.; Huang, Y.; Dunn, B., Gold-coated M13 bacteriophage as a template for glucose oxidase biofuel cells with direct electron transfer. *ACS nano* **2016,** *10* (1), 324-332.

24. Hyun, K.; Han, S. W.; Koh, W.-G.; Kwon, Y., Direct electrochemistry of glucose oxidase immobilized on carbon nanotube for improving glucose sensing. *International journal of hydrogen energy* **2015,** *40* (5), 2199-2206.

25. Zhao, M.; Gao, Y.; Sun, J.; Gao, F., Mediatorless glucose biosensor and direct electron transfer type glucose/air biofuel cell enabled with carbon nanodots. *Analytical chemistry* **2015,** *87* (5), 2615-2622.

26. Wooten, M.; Karra, S.; Zhang, M.; Gorski, W., On the direct electron transfer, sensing, and enzyme activity in the glucose oxidase/carbon nanotubes system. *Analytical chemistry* **2014,** *86* (1), 752-757.

27. Zhang, X.; Liu, D.; Li, L.; You, T., Direct electrochemistry of glucose oxidase on novel free-standing nitrogen-doped carbon nanospheres@ carbon nanofibers composite film. *Scientific reports* **2015,** *5* (1), 1-11.

28. Zhong, X.; Yuan, W.; Kang, Y.; Xie, J.; Hu, F.; Li, C. M., Biomass-Derived Hierarchical Nanoporous Carbon with Rich Functional Groups for Direct-Electron-Transfer-Based Glucose Sensing. *ChemElectroChem* **2016,** *3* (1), 144-151.

29. Sheng, M.; Gao, Y.; Sun, J.; Gao, F., Carbon nanodots–chitosan composite film: a platform for protein immobilization, direct electrochemistry and bioelectrocatalysis. *Biosensors and Bioelectronics* **2014,** *58*, 351-358.

30. Malel, E.; Mandler, D., Direct electron transfer between glucose oxidase and gold nanoparticles; when size matters. *ChemElectroChem* **2019,** *6* (1), 147-154.

31. Mano, N., Engineering glucose oxidase for bioelectrochemical applications. *Bioelectrochemistry* **2019,** *128*, 218-240.

32. Moolayadukkam, S.; Thomas, S.; Sahoo, R. C.; Lee, C. H.; Lee, S. U.; Matte, H. R., Role of transition metals in layered double hydroxides for differentiating the oxygen evolution and nonenzymatic glucose sensing. *ACS applied materials & interfaces* **2020,** *12* (5), 6193-6204.

33. Xu, J.; Li, F.; Wang, D.; Nawaz, M. H.; An, Q.; Han, D.; Niu, L., Co3O4 nanostructures on flexible carbon cloth for crystal plane effect of nonenzymatic electrocatalysis for glucose. *Biosensors and Bioelectronics* **2019,** *123*, 25-29.

34. Sinha, L.; Pakhira, S.; Bhojane, P.; Mali, S.; Hong, C. K.; Shirage, P. M., Hybridization of Co3O4 and α-MnO2 nanostructures for high-performance nonenzymatic glucose sensing. *ACS Sustainable Chemistry & Engineering* **2018,** *6* (10), 13248-13261.

35. Lee, J.; Hyun, K.; Kwon, Y., A study on the stability and sensitivity of mediator-based enzymatic glucose sensor measured by catalyst consisting of multilayer stacked via layer-by-layer. *Journal of Industrial and Engineering Chemistry* **2021,** *93*, 383-387.

36. Chen, M.; Cao, X.; Chang, K.; Xiang, H.; Wang, R., A novel electrochemical non-enzymatic glucose sensor based on Au nanoparticle-modified indium tin oxide electrode and boronate affinity. *Electrochimica Acta* **2021,** *368*, 137603.

37. Meng, A.; Hong, X.; Zhang, H.; Tian, W.; Li, Z.; Sheng, L.; Li, Q., Nickel sulfide nanoworm network architecture as a binder-free high-performance non-enzymatic glucose sensor. *Microchimica Acta* **2021,** *188* (2), 1-9.

38. Jang, K.-b.; Park, K. R.; min Kim, K.; Hyun, S.-k.; Ahn, C.; Kim, J. C.; Lim, S.-c.; Han, H.; Mhin, S., Electrochemical performance of the spinel NiCo2O4 based nanostructure synthesized by chemical bath method for glucose detection. *Applied Surface Science* **2021**, 148927.

39. Guo, C.; Li, H.; Zhang, X.; Huo, H.; Xu, C., 3D porous CNT/MnO2 composite electrode for high-performance enzymeless glucose detection and supercapacitor application. *Sensors and Actuators B: Chemical* **2015,** *206*, 407-414.

40. Liu, L.; Jiang, Z.; Fang, L.; Xu, H.; Zhang, H.; Gu, X.; Wang, Y., Probing the crystal plane effect of Co3O4 for enhanced electrocatalytic performance toward efficient overall water splitting. *ACS applied materials & interfaces* **2017,** *9* (33), 27736-27744.

41. Shah, J.; Jain, S.; Gahtori, B.; Sharma, C.; Kotnala, R. K., Water splitting on the mesoporous surface and oxygen vacancies of iron oxide generates electricity by hydroelectric cell. *Materials Chemistry and Physics* **2021,** *258*, 123981.

42. Lotfi, Z.; Gholivand, M.; Shamsipur, M., Non-enzymatic glucose sensor based on a g-C3N4/NiO/CuO nanocomposite. *Analytical Biochemistry* **2021,** *616*, 114062.

43. Li, L.; Scott, K.; Yu, E. H., A direct glucose alkaline fuel cell using MnO2–carbon nanocomposite supported gold catalyst for anode glucose oxidation. *Journal of power sources* **2013,** *221*, 1-5.

44. Ponnusamy, R.; Venkatesan, R.; Kandasamy, M.; Chakraborty, B.; Rout, C. S., MnO2 polymorph selection for non-enzymatic glucose detection: An integrated experimental and density functional theory investigation. *Applied Surface Science* **2019,** *487*, 1033-1042.

45. Wen, Q.; Wang, S.; Yan, J.; Cong, L.; Pan, Z.; Ren, Y.; Fan, Z., MnO2–graphene hybrid as an alternative cathodic catalyst to platinum in microbial fuel cells. *Journal of power sources* **2012,** *216*, 187-191.

46. Wang, H.-Y.; Hung, S.-F.; Chen, H.-Y.; Chan, T.-S.; Chen, H. M.; Liu, B., In operando identification of geometrical-site-dependent water oxidation activity of spinel Co3O4. *Journal of the American Chemical Society* **2016,** *138* (1), 36-39.

47. Du, S.; Ren, Z.; Zhang, J.; Wu, J.; Xi, W.; Zhu, J.; Fu, H., Co 3 O 4 nanocrystal ink printed on carbon fiber paper as a large-area electrode for electrochemical water splitting. *Chemical Communications* **2015,** *51* (38), 8066-8069.

48. Zeng, Z.; Zhang, T.; Liu, Y.; Zhang, W.; Yin, Z.; Ji, Z.; Wei, J., Magnetic Field-Enhanced 4-Electron Pathway for Well-Aligned Co_3O_4/Electrospun Carbon Nanofibers in the Oxygen Reduction Reaction. *ChemSusChem* **2018,** *11* (3), 580-588.

49. Liang, Y.; Wang, H.; Zhou, J.; Li, Y.; Wang, J.; Regier, T.; Dai, H., Covalent hybrid of spinel manganese–cobalt oxide and graphene as advanced oxygen reduction electrocatalysts. *Journal of the American Chemical Society* **2012,** *134* (7), 3517-3523.

50. Du, G.; Liu, X.; Zong, Y.; Hor, T. A.; Yu, A.; Liu, Z., Co 3 O 4 nanoparticle-modified MnO 2 nanotube bifunctional oxygen cathode catalysts for rechargeable zinc–air batteries. *Nanoscale* **2013,** *5* (11), 4657-4661.

51. Mei, J.; Liao, T.; Ayoko, G. A.; Bell, J.; Sun, Z., Cobalt oxide-based nanoarchitectures for electrochemical energy applications. *Progress in Materials Science* **2019,** *103*, 596-677.

52. Emran, M. Y.; Shenashen, M. A.; Mekawy, M.; Azzam, A. M.; Akhtar, N.; Gomaa, H.; Selim, M. M.; Faheem, A.; El-Safty, S. A., Ultrasensitive in-vitro monitoring of monoamine neurotransmitters from dopaminergic cells. *Sensors and Actuators B: Chemical* **2018,** *259*, 114-124.

53. Li, B.-R.; Hsieh, Y.-J.; Chen, Y.-X.; Chung, Y.-T.; Pan, C.-Y.; Chen, Y.-T., An ultrasensitive nanowire-transistor biosensor for detecting dopamine release from living

PC12 cells under hypoxic stimulation. *Journal of the American Chemical Society* **2013,** *135* (43), 16034-16037.

54. Lei, Y.; Butler, D.; Lucking, M. C.; Zhang, F.; Xia, T.; Fujisawa, K.; Granzier-Nakajima, T.; Cruz-Silva, R.; Endo, M.; Terrones, H., Single-atom doping of MoS2 with manganese enables ultrasensitive detection of dopamine: Experimental and computational approach. *Sci. Adv.* **2020,** *6* (32), eabc4250.

55. Abe, H.; Ino, K.; Li, C.-Z.; Kanno, Y.; Inoue, K. Y.; Suda, A.; Kunikata, R.; Matsudaira, M.; Takahashi, Y.; Shiku, H., Electrochemical imaging of dopamine release from three-dimensional-cultured PC12 cells using large-scale integration-based amperometric sensors. *Analytical chemistry* **2015,** *87* (12), 6364-6370.

56. Shu, Y.; Lu, Q.; Yuan, F.; Tao, Q.; Jin, D.; Yao, H.; Xu, Q.; Hu, X., Stretchable Electrochemical Biosensing Platform Based on Ni-MOF Composite/Au Nanoparticle-Coated Carbon Nanotubes for Real-Time Monitoring of Dopamine Released from Living Cells. *ACS Applied Materials & Interfaces* **2020,** *12* (44), 49480-49488.

57. Mercante, L. A.; Pavinatto, A.; Iwaki, L. E.; Scagion, V. P.; Zucolotto, V.; Oliveira Jr, O. N.; Mattoso, L. H.; Correa, D. S., Electrospun polyamide 6/poly (allylamine hydrochloride) nanofibers functionalized with carbon nanotubes for electrochemical detection of dopamine. *ACS applied materials & interfaces* **2015,** *7* (8), 4784-4790.

58. Wiatrak, B.; Kubis-Kubiak, A.; Piwowar, A.; Barg, E., PC12 cell line: cell types, coating of culture vessels, differentiation and other culture conditions. *Cells* **2020,** *9* (4), 958.

59. Kim, D.-S.; Kang, E.-S.; Baek, S.; Choo, S.-S.; Chung, Y.-H.; Lee, D.; Min, J.; Kim, T.-H., Electrochemical detection of dopamine using periodic cylindrical gold nanoelectrode arrays. *Scientific reports* **2018,** *8* (1), 1-10.

60. Zan, X.; Bai, H.; Wang, C.; Zhao, F.; Duan, H., Graphene paper decorated with a 2D array of dendritic platinum nanoparticles for ultrasensitive electrochemical detection of dopamine secreted by live cells. *Chemistry–A European Journal* **2016,** *22* (15), 5204-5210.

61. Xu, Q.; Yuan, H.; Dong, X.; Zhang, Y.; Asif, M.; Dong, Z.; He, W.; Ren, J.; Sun, Y.; Xiao, F., Dual nanoenzyme modified microelectrode based on carbon fiber coated with AuPd alloy nanoparticles decorated graphene quantum dots assembly for electrochemical detection in clinic cancer samples. *Biosensors and Bioelectronics* **2018,** *107*, 153-162.

62. Fang, J.; Xie, Z.; Wallace, G.; Wang, X., Co-deposition of carbon dots and reduced graphene oxide nanosheets on carbon-fiber microelectrode surface for selective detection of dopamine. *Applied Surface Science* **2017,** *412*, 131-137.

63. Kim, S. G.; Jun, J.; Kim, Y. K.; Kim, J.; Lee, J. S.; Jang, J., Facile synthesis of Co3O4-incorporated multichannel carbon nanofibers for electrochemical applications. *ACS applied materials & interfaces* **2020,** *12* (18), 20613-20622.

64. Hou, T. Z.; Chen, X.; Peng, H. J.; Huang, J. Q.; Li, B. Q.; Zhang, Q.; Li, B., Design principles for heteroatom-doped nanocarbon to achieve strong anchoring of polysulfides for lithium–sulfur batteries. *Small* **2016,** *12* (24), 3283-3291.

65. Guan, L.; Hu, H.; Li, L.; Pan, Y.; Zhu, Y.; Li, Q.; Guo, H.; Wang, K.; Huang, Y.; Zhang, M., Intrinsic defect-rich hierarchically porous carbon architectures enabling enhanced capture and catalytic conversion of polysulfides. *ACS nano* **2020,** *14* (5), 6222-6231.

66. Li, L.; Liu, D.; Wang, K.; Mao, H.; You, T., Quantitative detection of nitrite with N-doped graphene quantum dots decorated N-doped carbon nanofibers composite-based electrochemical sensor. *Sensors and Actuators B: Chemical* **2017,** *252*, 17-23.

67. Zhang, R.; Chen, X. R.; Chen, X.; Cheng, X. B.; Zhang, X. Q.; Yan, C.; Zhang, Q., Lithiophilic sites in doped graphene guide uniform lithium nucleation for dendrite-free lithium metal anodes. *Angewandte Chemie* **2017,** *129* (27), 7872-7876.

68. Peng, H. J.; Hou, T. Z.; Zhang, Q.; Huang, J. Q.; Cheng, X. B.; Guo, M. Q.; Yuan, Z.; He, L. Y.; Wei, F., Strongly coupled interfaces between a heterogeneous carbon host and a sulfur-containing guest for highly stable lithium-sulfur batteries: mechanistic insight into capacity degradation. *Advanced Materials Interfaces* **2014,** *1* (7), 1400227.

69. Wang, Y.; Shao, Y.; Matson, D. W.; Li, J.; Lin, Y., Nitrogen-doped graphene and its application in electrochemical biosensing. *ACS nano* **2010,** *4* (4), 1790-1798.

70. Odebunmi, E.; Owalude, S., Kinetic and thermodynamic studies of glucose oxidase catalysed oxidation reaction of glucose. **2007**.

71. Guo, C. X.; Li, C. M., Direct electron transfer of glucose oxidase and biosensing of glucose on hollow sphere-nanostructured conducting polymer/metal oxide composite. *Physical Chemistry Chemical Physics* **2010,** *12* (38), 12153-12159.

72. Baghayeri, M.; Veisi, H.; Ghanei-Motlagh, M., Amperometric glucose biosensor based on immobilization of glucose oxidase on a magnetic glassy carbon electrode modified with a novel magnetic nanocomposite. *Sensors and Actuators B: Chemical* **2017,** *249*, 321-330.

73. Roth, J. P.; Klinman, J. P., Catalysis of electron transfer during activation of O2 by the flavoprotein glucose oxidase. *Proceedings of the National Academy of Sciences* **2003,** *100* (1), 62-67.

74. Frew, J. E.; Hill, H. A. O., Direct and indirect electron transfer between electrodes and redox proteins. *European journal of biochemistry* **1988,** *172* (2), 261-269.

75. Adachi, T.; Kitazumi, Y.; Shirai, O.; Kano, K., Direct electron transfer-type bioelectrocatalysis of redox enzymes at nanostructured electrodes. *Catalysts* **2020,** *10* (2), 236.

76. Artes, J. M.; Diez-Perez, I.; Sanz, F.; Gorostiza, P., Direct measurement of electron transfer distance decay constants of single redox proteins by electrochemical tunneling spectroscopy. *Acs Nano* **2011,** *5* (3), 2060-2066.

77. Liu, J.; Paddon-Row, M. N.; Gooding, J. J., Heterogeneous electron-transfer kinetics for flavin adenine dinucleotide and ferrocene through alkanethiol mixed monolayers on gold electrodes. *The Journal of Physical Chemistry B* **2004,** *108* (24), 8460-8466.

78. Yehezkeli, O.; Raichlin, S.; Tel-Vered, R.; Kesselman, E.; Danino, D.; Willner, I., Biocatalytic implant of Pt nanoclusters into glucose oxidase: A method to electrically wire the enzyme and to transform it from an oxidase to a hydrogenase. *The Journal of Physical Chemistry Letters* **2010,** *1* (19), 2816-2819.

79. Rafighi, P.; Tavahodi, M.; Haghighi, B., Fabrication of a third-generation glucose biosensor using graphene-polyethyleneimine-gold nanoparticles hybrid. *Sensors and Actuators B: Chemical* **2016,** *232*, 454-461.

80. Luong, J. H.; Glennon, J. D.; Gedanken, A.; Vashist, S. K., Achievement and assessment of direct electron transfer of glucose oxidase in electrochemical biosensing using carbon nanotubes, graphene, and their nanocomposites. *Microchimica Acta* **2017,** *184* (2), 369-388.

81. Tiwari, J. N.; Vij, V.; Kemp, K. C.; Kim, K. S., Engineered carbon-nanomaterial-based electrochemical sensors for biomolecules. *ACS nano* **2016,** *10* (1), 46-80.

82. Si, P.; Ding, S.; Yuan, J.; Lou, X. W.; Kim, D.-H., Hierarchically structured one-dimensional TiO2 for protein immobilization, direct electrochemistry, and mediator-free glucose sensing. *ACS nano* **2011,** *5* (9), 7617-7626.

83. Lalaoui, N. m.; Rousselot-Pailley, P.; Robert, V.; Mekmouche, Y.; Villalonga, R.; Holzinger, M.; Cosnier, S.; Tron, T.; Le Goff, A., Direct electron transfer between a site-specific pyrene-modified laccase and carbon nanotube/gold nanoparticle supramolecular assemblies for bioelectrocatalytic dioxygen reduction. *Acs Catalysis* **2016,** *6* (3), 1894-1900.

84. Jose, M. V.; Marx, S.; Murata, H.; Koepsel, R. R.; Russell, A. J., Direct electron transfer in a mediator-free glucose oxidase-based carbon nanotube-coated biosensor. *Carbon* **2012,** *50* (11), 4010-4020.

85. Bartlett, P. N.; Al-Lolage, F. A., There is no evidence to support literature claims of direct electron transfer (DET) for native glucose oxidase (GOx) at carbon nanotubes or graphene. *Journal of Electroanalytical Chemistry* **2018,** *819*, 26-37.

86. Liang, B.; Guo, X.; Fang, L.; Hu, Y.; Yang, G.; Zhu, Q.; Wei, J.; Ye, X., Study of direct electron transfer and enzyme activity of glucose oxidase on graphene surface. *Electrochemistry Communications* **2015,** *50,* 1-5.

87. Zhang, J.; Feng, M.; Tachikawa, H., Layer-by-layer fabrication and direct electrochemistry of glucose oxidase on single wall carbon nanotubes. *Biosensors and Bioelectronics* **2007,** *22* (12), 3036-3041.

88. Janegitz, B. C.; Pauliukaite, R.; Ghica, M. E.; Brett, C. M.; Fatibello-Filho, O., Direct electron transfer of glucose oxidase at glassy carbon electrode modified with functionalized carbon nanotubes within a dihexadecylphosphate film. *Sensors and Actuators B: Chemical* **2011,** *158* (1), 411-417.

89. So, K.; Kitazumi, Y.; Shirai, O.; Kano, K., Analysis of factors governing direct electron transfer-type bioelectrocatalysis of bilirubin oxidase at modified electrodes. *Journal of Electroanalytical Chemistry* **2016,** *783*, 316-323.

90. Guiseppi-Elie, A.; Lei, C.; Baughman, R. H., Direct electron transfer of glucose oxidase on carbon nanotubes. *Nanotechnology* **2002,** *13* (5), 559.

91. Cai, C.; Chen, J., Direct electron transfer of glucose oxidase promoted by carbon nanotubes. *Analytical biochemistry* **2004,** *332* (1), 75-83.

92. Liu, Y.; Zhang, J.; Cheng, Y.; Jiang, S. P., Effect of carbon nanotubes on direct electron transfer and electrocatalytic activity of immobilized glucose oxidase. *ACS omega* **2018,** *3* (1), 667-676.

93. Simonov, A. N.; Grosse, W.; Mashkina, E. A.; Bethwaite, B.; Tan, J.; Abramson, D.; Wallace, G. G.; Moulton, S. E.; Bond, A. M., New insights into the analysis of the electrode kinetics of flavin adenine dinucleotide redox center of glucose oxidase immobilized on carbon electrodes. *Langmuir* **2014,** *30* (11), 3264-3273.

94. Zhao, H.-Z.; Sun, J.-J.; Song, J.; Yang, Q.-Z., Direct electron transfer and conformational change of glucose oxidase on carbon nanotube-based electrodes. *Carbon* **2010,** *48* (5), 1508-1514.

95. Wang, Y.; Yao, Y., Direct electron transfer of glucose oxidase promoted by carbon nanotubes is without value in certain mediator-free applications. *Microchimica Acta* **2012,** *176* (3-4), 271-277.

96. Goran, J. M.; Mantilla, S. M.; Stevenson, K. J., Influence of surface adsorption on the interfacial electron transfer of flavin adenine dinucleotide and glucose oxidase at carbon nanotube and nitrogen-doped carbon nanotube electrodes. *Analytical chemistry* **2013,** *85* (3), 1571-1581.

97. Liu, Y.; Dolidze, T. D.; Singhal, S.; Khoshtariya, D. E.; Wei, J., New evidence for a quasi-simultaneous proton-coupled two-electron transfer and direct wiring for glucose oxidase captured by the carbon nanotube–polymer matrix. *The Journal of Physical Chemistry C* **2015,** *119* (27), 14900-14910.

98. Wei, J.; Liu, H.; Dick, A. R.; Yamamoto, H.; He, Y.; Waldeck, D. H., Direct wiring of cytochrome c's heme unit to an electrode: Electrochemical studies. *Journal of the American Chemical Society* **2002,** *124* (32), 9591-9599.

99. Weber, K.; Creager, S. E., Voltammetry of redox-active groups irreversibly adsorbed onto electrodes. Treatment using the Marcus relation between rate and overpotential. *Anal. Chem.* **1994,** *66* (19), 3164-3172.

100. Tender, L.; Carter, M. T.; Murray, R. W., Cyclic voltammetric analysis of ferrocene alkanethiol monolayer electrode kinetics based on Marcus theory. *Anal. Chem.* **1994,** *66* (19), 3173-3181.

101. Laviron, E., General expression of the linear potential sweep voltammogram in the case of diffusionless electrochemical systems. *J. Electroanal. Chem.* **1979,** *101* (1), 19-28.

102. Eckermann, A. L.; Feld, D. J.; Shaw, J. A.; Meade, T. J., Electrochemistry of redox-active self-assembled monolayers. *Coord. Chem. Rev.* **2010,** *254* (15-16), 1769-1802.

103. Chidsey, C. E., Free energy and temperature dependence of electron transfer at the metal-electrolyte interface. *Science* **1991,** *251* (4996), 919-922.

104. Zeng, Z.; Wei, J.; Liu, Y.; Zhang, W.; Mabe, T., Magnetoreception of Photoactivated Cryptochrome 1 in Electrochemistry and Electron Transfer. *ACS Omega* **2018,** *3* (5), 4752-4759.

105. Zeng, Z.; Zhang, W.; Ji, Z.; Yin, Z.; Wei, J., Magnetically-enhanced electron transfer from immobilized galvinoxyl radicals. *Electrochem. Commun.* **2018**.

106. Cable, M.; Smith, E. T., Identifying the n= 2 reaction mechanism of FAD through voltammetric simulations. *Analytica chimica acta* **2005,** *537* (1-2), 299-306.

107. Wang, Y.; Sun, M.; Qiao, J.; Ouyang, J.; Na, N., FAD roles in glucose catalytic oxidation studied by multiphase flow of extractive electrospray ionization (MF-EESI) mass spectrometry. *Chemical science* **2018,** *9* (3), 594-599.

108. Numan, A.; Shahid, M. M.; Omar, F. S.; Ramesh, K.; Ramesh, S., Facile fabrication of cobalt oxide nanograin-decorated reduced graphene oxide composite as ultrasensitive platform for dopamine detection. *Sensors and Actuators B: Chemical* **2017,** *238*, 1043-1051.

109. Bagdžiūnas, G.; Ramanavičius, A., Towards direct enzyme wiring: A theoretical investigation of charge carrier transfer mechanisms between glucose oxidase and organic semiconductors. *Physical chemistry chemical physics* **2019,** *21* (6), 2968-2976.

110. Samukaite-Bubniene, U.; Mazetyte-Stasinskiene, R.; Chernyakova, K.; Karpicz, R.; Ramanavicius, A., Time-resolved fluorescence spectroscopy based evaluation of stability of glucose oxidase. *International Journal of Biological Macromolecules* **2020,** *163*, 676-682.

111. Lu, Y.; Zhong, D., Understanding short-range electron-transfer dynamics in proteins. *The journal of physical chemistry letters* **2019,** *10* (3), 346-351.

112. Khoshtariya, D. E.; Wei, J.; Liu, H.; Yue, H.; Waldeck, D. H., Charge-transfer mechanism for cytochrome c adsorbed on nanometer thick films. Distinguishing frictional control from conformational gating. *Journal of the American Chemical Society* **2003,** *125* (25), 7704-7714.

113. Hecht, H.; Kalisz, H.; Hendle, J.; Schmid, R.; Schomburg, D., Crystal structure of glucose oxidase from Aspergillus niger refined at 2· 3 Å reslution. *Journal of molecular biology* **1993,** *229* (1), 153-172.

114. Hecht, H.; Schomburg, D.; Kalisz, H.; Schmid, R., The 3D structure of glucose oxidase from Aspergillus niger. Implications for the use of GOD as a biosensor enzyme. *Biosensors and Bioelectronics* **1993,** *8* (3-4), 197-203.

115. Wohlfahrt, G.; Witt, S.; Hendle, J.; Schomburg, D.; Kalisz, H. M.; Hecht, H.-J., 1.8 and 1.9 Å resolution structures of the Penicillium amagasakiense and Aspergillus niger glucose oxidases as a basis for modelling substrate complexes. *Acta Crystallographica Section D: Biological Crystallography* **1999,** *55* (5), 969-977.

116. Matyushov, D. V., Nanosecond Stokes shift dynamics, dynamical transition, and gigantic reorganization energy of hydrated heme proteins. *The Journal of Physical Chemistry B* **2011,** *115* (36), 10715-10724.

117. Bagdžiūnas, G.; Žukauskas, Š.; Ramanavičius, A., Insights into a hole transfer mechanism between glucose oxidase and a p-type organic semiconductor. *Biosensors and Bioelectronics* **2018,** *102*, 449-455.

118. Sun, B.; Hong, W.; Thibau, E. S.; Aziz, H.; Lu, Z.-H.; Li, Y., Polyethylenimine (PEI) as an effective dopant to conveniently convert ambipolar and p-type polymers into unipolar n-type polymers. *ACS applied materials & interfaces* **2015,** *7* (33), 18662-18671.

119. Olsman, N.; Goentoro, L., Allosteric proteins as logarithmic sensors. *Proceedings of the National Academy of Sciences* **2016,** *113* (30), E4423-E4430.
120. Li, Z.; Zhang, H.; Xueping, G.; Liang, Y.; An, X.; Yang, C.; Fang, B.; Xie, H.; Wei, J., A nanocomposite of copper (ii) functionalized graphene and application for sensing sulfurated organophosphorus pesticides. *New Journal of Chemistry* **2013,** *37* (12), 3956-3963.

121. Lee, S.; Lee, J.; Park, S.; Boo, H.; Kim, H. C.; Chung, T. D., Disposable non-enzymatic blood glucose sensing strip based on nanoporous platinum particles. *Appl. Mater. Today* **2018,** *10*, 24-29.

122. Gao, H.; Xiao, F.; Ching, C. B.; Duan, H., One-step electrochemical synthesis of PtNi nanoparticle-graphene nanocomposites for nonenzymatic amperometric glucose detection. *ACS Appl. Mater. Interfaces* **2011,** *3* (8), 3049-3057.

123. Dong, Q.; Wang, X.; Willis, W. S.; Song, D.; Huang, Y.; Zhao, J.; Li, B.; Lei, Y., Nitrogen-doped Hollow Co_3O_4 Nanofibers for both Solid-state pH Sensing and Improved Non-enzymatic Glucose Sensing. *Electroanalysis* **2019,** *31* (4), 678-687.

124. Zhu, H.; Li, L.; Zhou, W.; Shao, Z.; Chen, X., Advances in non-enzymatic glucose sensors based on metal oxides. *J. Mater. Chem. B* **2016,** *4* (46), 7333-7349.

125. Zhi, M.; Xiang, C.; Li, J.; Li, M.; Wu, N., Nanostructured carbon–metal oxide composite electrodes for supercapacitors: a review. *Nanoscale* **2013,** *5* (1), 72-88.

126. Zhang, Z.; Liu, J.; Gu, J.; Su, L.; Cheng, L., An overview of metal oxide materials as electrocatalysts and supports for polymer electrolyte fuel cells. *Energy Environ. Sci.* **2014,** *7* (8), 2535-2558.

127. Li, Y.; Zhang, L.; Peng, J.; Zhang, W.; Peng, K., Magnetic field enhancing electrocatalysis of Co3O4/NF for oxygen evolution reaction. *Journal of Power Sources* **2019,** *433*, 226704.

128. Dong, X.-C.; Xu, H.; Wang, X.-W.; Huang, Y.-X.; Chan-Park, M. B.; Zhang, H.; Wang, L.-H.; Huang, W.; Chen, P., 3D graphene–cobalt oxide electrode for high-performance supercapacitor and enzymeless glucose detection. *ACS Nano* **2012,** *6* (4), 3206-3213.

129. Yuan, B.; Xu, C.; Deng, D.; Xing, Y.; Liu, L.; Pang, H.; Zhang, D., Graphene oxide/nickel oxide modified glassy carbon electrode for supercapacitor and nonenzymatic glucose sensor. *Electrochim. Acta* **2013,** *88*, 708-712.

130. Ci, S.; Huang, T.; Wen, Z.; Cui, S.; Mao, S.; Steeber, D. A.; Chen, J., Nickel oxide hollow microsphere for non-enzyme glucose detection. *Biosens. Bioelectron.* **2014,** *54*, 251-257.

131. Ahmad, R.; Vaseem, M.; Tripathy, N.; Hahn, Y.-B., Wide linear-range detecting nonenzymatic glucose biosensor based on CuO nanoparticles inkjet-printed on electrodes. *Anal. Chem.* **2013,** *85* (21), 10448-10454.

132. Song, J.; Xu, L.; Zhou, C.; Xing, R.; Dai, Q.; Liu, D.; Song, H., Synthesis of graphene oxide based CuO nanoparticles composite electrode for highly enhanced nonenzymatic glucose detection. *ACS Appl. Mater. Interfaces* **2013,** *5* (24), 12928-12934.

133. Meng, F.; Shi, W.; Sun, Y.; Zhu, X.; Wu, G.; Ruan, C.; Liu, X.; Ge, D., Nonenzymatic biosensor based on Cu_xO nanoparticles deposited on polypyrrole nanowires for improving detectionrange. *Biosens. Bioelectron.* **2013,** *42*, 141-147.

134. Du, G.; Liu, X.; Zong, Y.; Hor, T. A.; Yu, A.; Liu, Z., Co_3O_4 nanoparticle-modified MnO_2 nanotube bifunctional oxygen cathode catalysts for rechargeable zinc–air batteries. *Nanoscale* **2013,** *5* (11), 4657-4661.

135. Zeng, Z.; Zhang, W.; Liu, Y.; Lu, P.; Wei, J., Uniformly electrodeposited α-MnO2 film on super-aligned electrospun carbon nanofibers for a bifunctional catalyst design in oxygen reduction reaction. *Electrochimica Acta* **2017,** *256*, 232-240.

136. Wang, H.-Y.; Hung, S.-F.; Chen, H.-Y.; Chan, T.-S.; Chen, H. M.; Liu, B., In operando identification of geometrical-site-dependent water oxidation activity of spinel Co_3O_4. *J. Am. Chem. Soc.* **2015,** *138* (1), 36-39.

137. Du, S.; Ren, Z.; Zhang, J.; Wu, J.; Xi, W.; Zhu, J.; Fu, H., Co_3O_4 nanocrystal ink printed on carbon fiber paper as a large-area electrode for electrochemical water splitting. *Chem. Commun.* **2015,** *51* (38), 8066-8069.

138. Chang, T.; Shen, Z.; Huang, Y.; Lu, J.; Ren, D.; Sun, J.; Cao, J.; Liu, H., Post-plasma-catalytic removal of toluene using MnO_2–Co_3O_4 catalysts and their synergistic mechanism. *Chem. Eng. J.* **2018,** *348*, 15-25.

139. Li, X.; Sun, Y.; Wu, Q.; Liu, H.; Gu, W.; Wang, X.; Cheng, Z.; Fu, Z.; Lu, Y., Optimized electronic configuration to improve the surface absorption and bulk conductivity for enhanced oxygen evolution reaction. *J. Am. Chem. Soc.* **2019,** *141* (7), 3121-3128.

140. Wang, Z.; Peng, S.; Hu, Y.; Li, L.; Yan, T.; Yang, G.; Ji, D.; Srinivasan, M.; Pan, Z.; Ramakrishna, S., Cobalt nanoparticles encapsulated in carbon nanotube-grafted nitrogen and sulfur co-doped multichannel carbon fibers as efficient bifunctional oxygen electrocatalysts. *J. Mater. Chem. A* **2017,** *5* (10), 4949-4961.

141. Ji, L.; Wang, J.; Wu, K.; Yang, N., Tunable Electrochemistry of Electrosynthesized Copper Metal–Organic Frameworks. *Adv. Funct. Mater.* **2018,** *28* (13), 1706961.

142. Li, Y.; Xie, M.; Zhang, X.; Liu, Q.; Lin, D.; Xu, C.; Xie, F.; Sun, X., Co-MOF nanosheet array: a high-performance electrochemical sensor for non-enzymatic glucose detection. *Sens. Actuator B-Chem.* **2019,** *278*, 126-132.

143. Liu, X.; Li, M.; Han, G.; Dong, J., The catalysts supported on metallized electrospun polyacrylonitrile fibrous mats for methanol oxidation. *Electrochim. Acta* **2010,** *55* (8), 2983-2990.

144. Liu, Y.; Zeng, Z.; Bloom, B.; Waldeck, D. H.; Wei, J., Stable Low-Current Electrodeposition of α-MnO_2 on Superaligned Electrospun Carbon Nanofibers for High-Performance Energy Storage. *Small* **2018,** *14* (3), 1703237.

145. Aboagye, A.; Liu, Y.; Ryan, J. G.; Wei, J.; Zhang, L., Hierarchical carbon composite nanofibrous electrode material for high-performance aqueous supercapacitors. *Mater. Chem. Phys.* **2018,** *214*, 557-563.

146. Mao, X.; Rutledge, G. C.; Hatton, T. A., Nanocarbon-based electrochemical systems for sensing, electrocatalysis, and energy storage. *Nano Today* **2014,** *9* (4), 405-432.

147. Hu, L.; Chen, W.; Xie, X.; Liu, N.; Yang, Y.; Wu, H.; Yao, Y.; Pasta, M.; Alshareef, H. N.; Cui, Y., Symmetrical MnO_2–carbon nanotube–textile nanostructures for wearable pseudocapacitors with high mass loading. *ACS Nano* **2011,** *5* (11), 8904-8913.

148. Liu, Y.; Huang, J.; Hou, H.; You, T., Simultaneous determination of dopamine, ascorbic acid and uric acid with electrospun carbon nanofibers modified electrode. *Electrochem. Commun.* **2008,** *10* (10), 1431-1434.

149. Liu, Y.; Chen, Z.; Shek, C.-H.; Wu, C. L.; Lai, J. K., Hierarchical mesoporous MnO_2 superstructures synthesized by soft-interface method and their catalytic performances. *ACS Appl. Mater. Interfaces* **2014,** *6* (12), 9776-9784.

150. Yang, S.; Liu, H.; Zhang, Y.; Wang, S.; Li, L.; Liu, X., Facile fabrication of hierarchical micro-meso-macro porous metal oxide with high photochemical and electrochemical performances. *Appl. Surf. Sci.* **2019,** *465*, 672-677.

151. Wang, X.; Huo, S.; Wang, R.; Wang, H.; Brett, D. J.; Ji, S., Synthesis of high surface area mesoporous MnO_2 via a "metastable" aqueous interfacial reaction. *J. Colloid Interface Sci.* **2017,** *503*, 76-85.

152. Liu, Y.; Zeng, Z.; Sharma, R. K.; Gbewonyo, S.; Allado, K.; Zhang, L.; Wei, J., A bi-functional configuration for a metal-oxide film supercapacitor. *Journal of Power Sources* **2019,** *409*, 1-5.

153. Abdalla, I.; Shen, J.; Yu, J.; Li, Z.; Ding, B., Co 3 O 4/carbon composite nanofibrous membrane enabled high-efficiency electromagnetic wave absorption. *Scientific reports* **2018,** *8* (1), 1-11.

154. Yang, Z.; Lv, J.; Pang, H.; Yan, W.; Qian, K.; Guo, T.; Guo, Z., Facile Synthesis of coaxial CNTs/MnO x-carbon hybrid nanofibers and their greatly enhanced lithium storage performance. *Scientific reports* **2015,** *5*, 17473.

155. Zhao, Y.; Ran, W.; He, J.; Huang, Y.; Liu, Z.; Liu, W.; Tang, Y.; Zhang, L.; Gao, D.; Gao, F., High-performance asymmetric supercapacitors based on multilayer MnO_2/graphene oxide nanoflakes and hierarchical porous carbon with enhanced cycling stability. *Small* **2015,** *11* (11), 1310-1319.

156. Qian, T.; Yu, C.; Zhou, X.; Ma, P.; Wu, S.; Xu, L.; Shen, J., Ultrasensitive dopamine sensor based on novel molecularly imprinted polypyrrole coated carbon nanotubes. *Biosens. Bioelectron.* **2014,** *58*, 237-241.

157. Yen, S.-C.; Liu, Z.-W.; Juang, R.-S.; Sahoo, S.; Huang, C.-H.; Chen, P.; Hsiao, Y.-S.; Fang, J.-T., Carbon nanotube/conducting polymer hybrid nanofibers as

novel organic bioelectronic interfaces for efficient removal of protein-bound uremic toxins. *ACS Appl. Mater. Interfaces* **2019,** *11* (47), 43843-43856.

158. Li, X.; Shao, S.; Yang, Y.; Mei, Y.; Qing, W.; Guo, H.; Peng, L. E.; Wang, P.; Tang, C. Y., Engineering Interface with a One-Dimensional RuO_2/TiO_2 Heteronanostructure in an Electrocatalytic Membrane Electrode: Toward Highly Efficient Micropollutant Decomposition. *ACS Appl. Mater. Interfaces* **2020,** *12* (19), 21596-21604.

159. Yu, D.; Yao, J.; Qiu, L.; Wang, Y.; Zhang, X.; Feng, Y.; Wang, H., In situ growth of Co_3O_4 nanoparticles on α-MnO_2 nanotubes: a new hybrid for high-performance supercapacitors. *J. Mater. Chem. A* **2014,** *2* (22), 8465-8471.

160. Awan, Z.; Nahm, K. S.; Xavier, J. S., Nanotubular MnO_2/graphene oxide composites for the application of open air-breathing cathode microbial fuel cells. *Biosens. Bioelectron.* **2014,** *53*, 528-534.

161. Han, W.; Dong, F.; Han, W.; Tang, Z., Mn-Polyacrylonitrile Nanofibers Decorated with Co-Metal—Organic Frameworks as Precursors of CoMnO x Catalysts for the Combustion of Toluene. *ACS Appl. Nano Mater.* **2020**.

162. Ekoi, E. J.; Gowen, A.; Dorrepaal, R.; Dowling, D. P., Characterisation of titanium oxide layers using Raman spectroscopy and optical profilometry: Influence of oxide properties. *Results in Physics* **2019,** *12*, 1574-1585.

163. Chen, S.; Zhu, J.; Wu, X.; Han, Q.; Wang, X., Graphene oxide− MnO_2 nanocomposites for supercapacitors. *ACS Nano* **2010,** *4* (5), 2822-2830.

164. Jiang, H.; Yang, L.; Li, C.; Yan, C.; Lee, P. S.; Ma, J., High–rate electrochemical capacitors from highly graphitic carbon–tipped manganese oxide/mesoporous carbon/manganese oxide hybrid nanowires. *Energy Environ. Sci.* **2011,** *4* (5), 1813-1819.

165. Ahmad, K.; Mohammad, A.; Mobin, S. M., Hydrothermally grown α-MnO_2 nanorods as highly efficient low cost counter-electrode material for dye-sensitized solar cells and electrochemical sensing applications. *Electrochim. Acta* **2017,** *252*, 549-557.

166. Wang, J.; Gao, R.; Zhou, D.; Chen, Z.; Wu, Z.; Schumacher, G.; Hu, Z.; Liu, X., Boosting the electrocatalytic activity of Co3O4 nanosheets for a Li-O2 battery through modulating inner oxygen vacancy and exterior Co3+/Co2+ ratio. *ACS Catal.* **2017,** *7* (10), 6533-6541.

167. Yan, X.; Tian, L.; He, M.; Chen, X., Three-dimensional crystalline/amorphous Co/Co3O4 core/shell nanosheets as efficient electrocatalysts for the hydrogen evolution reaction. *Nano letters* **2015,** *15* (9), 6015-6021.

168. Qiu, L.; Han, X.; Lu, Q.; Zhao, J.; Wang, Y.; Chen, Z.; Zhong, C.; Hu, W.; Deng, Y., Co_3O_4 Nanoparticles Supported on N-doped Electrospinning Carbon Nanofibers as an Efficient and Bifunctional Oxygen Electrocatalyst for Rechargeable Zn-Air Batteries. *Inorg. Chem. Front.* **2019,** *6*, 3554–3561.

169. Tang, W.; Yao, M.; Deng, Y.; Li, X.; Han, N.; Wu, X.; Chen, Y., Decoration of one-dimensional MnO_2 with Co_3O_4 nanoparticles: a heterogeneous interface for remarkably promoting catalytic oxidation activity. *Chem. Eng. J.* **2016,** *306*, 709-718.

170. Wang, J.-G.; Yang, Y.; Huang, Z.-H.; Kang, F., A high-performance asymmetric supercapacitor based on carbon and carbon–MnO_2 nanofiber electrodes. *Carbon* **2013,** *61*, 190-199.

171. Ding, Y.; Wang, Y.; Su, L.; Bellagamba, M.; Zhang, H.; Lei, Y., Electrospun Co_3O_4 nanofibers for sensitive and selective glucose detection. *Biosens. Bioelectron.* **2010,** *26* (2), 542-548.

172. Zhu, Q.; Li, Y.; Gao, Y.; Wang, X.; Song, S., Reduced Graphene-Wrapped MnO_2 Nanowires Self-Inserted with Co_3O_4 Nanocages: Remarkable Enhanced Performances for Lithium-Ion Anode Applications. *Chem. Eur. J.* **2016,** *22* (20), 6876-6880.

173. Xiao, X.; Zhang, X.; Zhang, Z.; You, J.; Liu, S.; Wang, Y., Macro-/meso-porous NiCo 2 O 4 synthesized by template-free solution combustion to enhance the performance of a nonenzymatic amperometric glucose sensor. *Microchim. Acta* **2020,** *187* (1), 64.

174. Zeng, Z.; Liu, Y.; Zhang, W.; Chevva, H.; Wei, J., Improved supercapacitor performance of MnO_2-electrospun carbon nanofibers electrodes by mT magnetic field. *J. Power Sources* **2017,** *358*, 22-28.

175. Ma, W.; Chen, S.; Yang, S.; Chen, W.; Weng, W.; Cheng, Y.; Zhu, M., Flexible all-solid-state asymmetric supercapacitor based on transition metal oxide nanorods/reduced graphene oxide hybrid fibers with high energy density. *Carbon* **2017,** *113*, 151-158.

176. Bazán, J. C.; Arvia, A. J., The diffusion of ferro-and ferricyanide ions in aqueous solutions of sodium hydroxide. *Electrochim. Acta* **1965,** *10*, 1025-1032.

177. Zhang, E.; Xie, Y.; Ci, S.; Jia, J.; Wen, Z., Porous Co_3O_4 hollow nanododecahedra for nonenzymatic glucose biosensor and biofuel cell. *Biosens. Bioelectron.* **2016,** *81*, 46-53.

178. Weina, X.; Guanlin, L.; Chuanshen, W.; Hu, C.; Wang, X., A novel β-MnO_2 micro/nanorod arrays directly grown on flexible carbon fiber fabric for high-performance enzymeless glucose sensing. *Electrochim. Acta* **2017,** *225*, 121-128.

179. Liu, M.; Liu, R.; Chen, W., Graphene wrapped Cu_2O nanocubes: non-enzymatic electrochemical sensors for the detection of glucose and hydrogen peroxide with enhanced stability. *Biosens. Bioelectron.* **2013,** *45*, 206-212.

180. Wei, J.; Liu, H.; Dick, A. R.; Yamamoto, H.; He, Y.; Waldeck, D. H., Direct Wiring of Cytochrome c's Heme Unit to an Electrode: Electrochemical Studies. *J. Am. Chem. Soc.* **2002,** *124* (32), 9591-9599.

181. Palmer, M.; Masikini, M.; Jiang, L.-W.; Wang, J.-J.; Cummings, F.; Chamier, J.; Inyang, O.; Chowdhury, M., Enhanced electrochemical glucose sensing performance of CuO: NiO mixed oxides thin film by plasma assisted nitrogen doping. *Journal of Alloys and Compounds* **2020,** *853*, 156900.

182. Han, L.; Yang, D.-P.; Liu, A., Leaf-templated synthesis of 3D hierarchical porous cobalt oxide nanostructure as direct electrochemical biosensing interface with enhanced electrocatalysis. *Biosens. Bioelectron.* **2015,** *63*, 145-152.

183. Ramasamy, R.; Ramachandran, K.; Philip, G. G.; Ramachandran, R.; Therese, H. A., Design and development of Co_3O_4/NiO composite nanofibers for the application of highly sensitive and selective non-enzymatic glucose sensors. *RSC Adv.* **2015,** *5* (93), 76538-76547.

184. Zhao, A.; She, J.; Manoj, D.; Wang, T.; Sun, Y.; Zhang, Y.; Xiao, F., Functionalized graphene fiber modified by dual nanoenzyme: Towards high-performance flexible nanohybrid microelectrode for electrochemical sensing in live cancer cells. *Sensors and Actuators B: Chemical* **2020,** *310*, 127861.

185. Nguyen, T. N.; Jin, X.; Nolan, J. K.; Xu, J.; Le, K. V. H.; Lam, S.; Wang, Y.; Alam, M. A.; Lee, H., Printable Nonenzymatic Glucose Biosensors Using Carbon Nanotube-PtNP Nanocomposites Modified with AuRu for Improved Selectivity. *ACS Biomaterials Science & Engineering* **2020,** *6* (9), 5315-5325.

186. Ashraf, G.; Asif, M.; Aziz, A.; Iftikhar, T.; Liu, H., Rice-Spikelet-like Copper Oxide Decorated with Platinum Stranded in the CNT Network for Electrochemical In Vitro Detection of Serotonin. *ACS Applied Materials & Interfaces* **2021**.

187. Xiao, F.; Li, Y.; Zan, X.; Liao, K.; Xu, R.; Duan, H., Growth of metal–metal oxide nanostructures on freestanding graphene paper for flexible biosensors. *Advanced Functional Materials* **2012,** *22* (12), 2487-2494.

188. Valentine, C. J.; Takagishi, K.; Umezu, S.; Daly, R.; De Volder, M., Paper based electrochemical sensors using paper as scaffold to create porous carbon nanotube electrodes. *ACS Applied Materials & Interfaces* **2020**.

189. Cen, D.; Ding, Y.; Wei, R.; Huang, X.; Gao, G.; Wu, G.; Mei, Y.; Bao, Z., Synthesis of Metal Oxide/Carbon Nanofibers via Biostructure Confinement as High-Capacity Anode Materials. *ACS Applied Materials & Interfaces* **2020**.

190. Park, S. J.; Lee, S. H.; Yang, H.; Park, C. S.; Lee, C.-S.; Kwon, O. S.; Park, T. H.; Jang, J., Human dopamine receptor-conjugated multidimensional conducting polymer nanofiber membrane for dopamine detection. *ACS applied materials & interfaces* **2016,** *8* (42), 28897-28903.

191. Yang, C.; Hu, K.; Wang, D.; Zubi, Y.; Lee, S. T.; Puthongkham, P.; Mirkin, M. V.; Venton, B. J., Cavity carbon-nanopipette electrodes for dopamine detection. *Analytical chemistry* **2019,** *91* (7), 4618-4624.

192. Yang, C.; Jacobs, C. B.; Nguyen, M. D.; Ganesana, M.; Zestos, A. G.; Ivanov, I. N.; Puretzky, A. A.; Rouleau, C. M.; Geohegan, D. B.; Venton, B. J., Carbon nanotubes grown on metal microelectrodes for the detection of dopamine. *Analytical chemistry* **2016,** *88* (1), 645-652.

193. Guan, H.; Zhang, J.; Liu, Y.; Zhao, Y.; Zhang, B., Rapid quantitative determination of hydrogen peroxide using an electrochemical sensor based on PtNi alloy/CeO2 plates embedded in N-doped carbon nanofibers. *Electrochimica Acta* **2019,** *295*, 997-1005.

194. Xu, X.; Du, Y.; Wang, C.; Guo, Y.; Zou, J.; Zhou, K.; Zeng, Z.; Liu, Y.; Li, L., High-entropy alloy nanoparticles on aligned electronspun carbon nanofibers for supercapacitors. *Journal of Alloys and Compounds* **2020,** *822*, 153642.

195. Yang, K.; Tang, J.; Liu, Y.; Kong, M.; Zhou, B.; Shang, Y.; Zhang, W.-H., Controllable Synthesis of Peapod-like Sb@ C and Corn-like C@ Sb Nanotubes for Sodium Storage. *ACS nano* **2020,** *14* (5), 5728-5737.

196. Pan, F.; Li, B.; Sarnello, E.; Fei, Y.; Gang, Y.; Xiang, X.; Du, Z.; Zhang, P.; Wang, G.; Nguyen, H. T., Atomically Dispersed Iron–Nitrogen Sites on Hierarchically Mesoporous Carbon Nanotube and Graphene Nanoribbon Networks for CO2 Reduction. *ACS nano* **2020,** *14* (5), 5506-5516.

197. Lu, L.; Zhou, L.; Chen, J.; Yan, F.; Liu, J.; Dong, X.; Xi, F.; Chen, P., Nanochannel-confined graphene quantum dots for ultrasensitive electrochemical analysis of complex samples. *ACS nano* **2018,** *12* (12), 12673-12681.

198. Shin, D.; Jeong, B.; Mun, B. S.; Jeon, H.; Shin, H.-J.; Baik, J.; Lee, J., On the origin of electrocatalytic oxygen reduction reaction on electrospun nitrogen–carbon species. *The Journal of Physical Chemistry C* **2013,** *117* (22), 11619-11624.

199. Xie, H.; Luo, G.; Niu, Y.; Weng, W.; Zhao, Y.; Ling, Z.; Ruan, C.; Li, G.; Sun, W., Synthesis and utilization of Co3O4 doped carbon nanofiber for fabrication of hemoglobin-based electrochemical sensor. *Materials Science and Engineering: C* **2020,** *107*, 110209.

200. Liang, Y.; Wang, H.; Diao, P.; Chang, W.; Hong, G.; Li, Y.; Gong, M.; Xie, L.; Zhou, J.; Wang, J., Oxygen reduction electrocatalyst based on strongly coupled cobalt oxide nanocrystals and carbon nanotubes. *Journal of the American Chemical Society* **2012,** *134* (38), 15849-15857.

201. Chattopadhyay, S.; Dash, S. K.; Tripathy, S.; Das, B.; Mandal, D.; Pramanik, P.; Roy, S., Toxicity of cobalt oxide nanoparticles to normal cells; an in vitro and in vivo study. *Chemico-biological interactions* **2015,** *226*, 58-71.

202. Thanh, T. D.; Balamurugan, J.; Lee, S. H.; Kim, N. H.; Lee, J. H., Effective seed-assisted synthesis of gold nanoparticles anchored nitrogen-doped graphene for electrochemical detection of glucose and dopamine. *Biosensors and Bioelectronics* **2016,** *81*, 259-267.

203. Peltola, E.; Wester, N.; Holt, K. B.; Johansson, L.-S.; Koskinen, J.; Myllymäki, V.; Laurila, T., Nanodiamonds on tetrahedral amorphous carbon significantly enhance dopamine detection and cell viability. *Biosensors and Bioelectronics* **2017,** *88*, 273-282.

204. Salamon, J.; Sathishkumar, Y.; Ramachandran, K.; Lee, Y. S.; Yoo, D. J.; Kim, A. R., One-pot synthesis of magnetite nanorods/graphene composites and its catalytic activity toward electrochemical detection of dopamine. *Biosensors and Bioelectronics* **2015,** *64*, 269-276.

205. Zhao, J.; Zhao, L.; Lan, C.; Zhao, S., Graphene quantum dots as effective probes for label-free fluorescence detection of dopamine. *Sensors and Actuators B: Chemical* **2016,** *223*, 246-251.

206. Govindaraju, S.; Ankireddy, S. R.; Viswanath, B.; Kim, J.; Yun, K., Fluorescent gold nanoclusters for selective detection of dopamine in cerebrospinal fluid. *Scientific reports* **2017,** *7*, 40298.

207. Vázquez-Guardado, A.; Barkam, S.; Peppler, M.; Biswas, A.; Dennis, W.; Das, S.; Seal, S.; Chanda, D., Enzyme-free plasmonic biosensor for direct detection of neurotransmitter dopamine from whole blood. *Nano letters* **2018,** *19* (1), 449-454.

208. Park, S. J.; Lee, J.; Seo, S. E.; Kim, K. H.; Park, C. S.; Lee, S. H.; Ban, H. S.; Lee, B. D.; Song, H. S.; Kim, J., High-Performance Conducting Polymer Nanotube-based Liquid-Ion Gated Field-Effect Transistor Aptasensor for Dopamine Exocytosis. *Scientific Reports* **2020,** *10* (1), 1-12.

209. Zhang, X.; Zheng, J., Hollow carbon sphere supported Ag nanoparticles for promoting electrocatalytic performance of dopamine sensing. *Sensors and Actuators B: Chemical* **2019,** *290*, 648-655.

210. Zou, J.; Wu, S.; Liu, Y.; Sun, Y.; Cao, Y.; Hsu, J.-P.; Wee, A. T. S.; Jiang, J., An ultra-sensitive electrochemical sensor based on 2D g-C3N4/CuO nanocomposites for dopamine detection. *Carbon* **2018,** *130*, 652-663.

211. Huang, Q.; Lin, X.; Tong, L.; Tong, Q.-X., Graphene quantum dots/multiwalled carbon nanotubes composite-based electrochemical sensor for detecting dopamine release from living cells. *ACS Sustainable Chemistry & Engineering* **2020,** *8* (3), 1644-1650.

212. Feng, X.; Zhang, Y.; Zhou, J.; Li, Y.; Chen, S.; Zhang, L.; Ma, Y.; Wang, L.; Yan, X., Three-dimensional nitrogen-doped graphene as an ultrasensitive electrochemical sensor for the detection of dopamine. *Nanoscale* **2015,** *7* (6), 2427-2432.

213. Liu, L.; Yin, Y. X.; Li, J. Y.; Wang, S. H.; Guo, Y. G.; Wan, L. J., Uniform lithium nucleation/growth induced by lightweight nitrogen-doped graphitic carbon foams for high-performance lithium metal anodes. *Advanced Materials* **2018,** *30* (10), 1706216.
214. Xu, M.; Wang, F.; Zhang, Y.; Yang, S.; Zhao, M.; Song, X., Co 3 O 4–carbon nanotube heterostructures with bead-on-string architecture for enhanced lithium storage performance. *Nanoscale* **2013,** *5* (17), 8067-8072.

215. Wang, X.; Li, X.; Zhang, L.; Yoon, Y.; Weber, P. K.; Wang, H.; Guo, J.; Dai, H., N-doping of graphene through electrothermal reactions with ammonia. *science* **2009,** *324* (5928), 768-771.

216. Akada, K.; Obata, S.; Saiki, K., Work Function Lowering of Graphite by Sequential Surface Modifications: Nitrogen and Hydrogen Plasma Treatment. *ACS omega* **2019,** *4* (15), 16531-16535.

217. Polshettiwar, V.; Baruwati, B.; Varma, R. S., Self-assembly of metal oxides into three-dimensional nanostructures: synthesis and application in catalysis. *ACS nano* **2009,** *3* (3), 728-736.

218. Kuo, C.-H.; Li, W.; Song, W.; Luo, Z.; Poyraz, A. S.; Guo, Y.; Ma, A. W.; Suib, S. L.; He, J., Facile synthesis of Co3O4@ CNT with high catalytic activity for CO oxidation under moisture-rich conditions. *ACS applied materials & interfaces* **2014,** *6* (14), 11311-11317.

219. Pang, M.; Long, G.; Jiang, S.; Ji, Y.; Han, W.; Wang, B.; Liu, X.; Xi, Y.; Wang, D.; Xu, F., Ethanol-assisted solvothermal synthesis of porous nanostructured cobalt oxides (CoO/Co3O4) for high-performance supercapacitors. *Chemical Engineering Journal* **2015,** *280*, 377-384.

220. Yu, J.; Chen, G.; Sunarso, J.; Zhu, Y.; Ran, R.; Zhu, Z.; Zhou, W.; Shao, Z., Cobalt Oxide and Cobalt-Graphitic Carbon Core–Shell Based Catalysts with Remarkably High Oxygen Reduction Reaction Activity. *Advanced science* **2016,** *3* (9), 1600060.

221. Xu, L.; Jiang, Q.; Xiao, Z.; Li, X.; Huo, J.; Wang, S.; Dai, L., Plasma-engraved Co3O4 nanosheets with oxygen vacancies and high surface area for the oxygen evolution reaction. *Angewandte Chemie* **2016,** *128* (17), 5363-5367.

222. Smyrnioti, M.; Ioannides, T., Synthesis of cobalt-based nanomaterials from Organic Precursors. *Cobalt* **2017**, 49.
223. He, B.; Chen, X.; Lu, J.; Yao, S.; Wei, J.; Zhao, Q.; Jing, D.; Huang, X.; Wang, T., One-pot synthesized Co/Co3O4-N-graphene composite as electrocatalyst for oxygen reduction reaction and oxygen evolution reaction. *Electroanalysis* **2016,** *28* (10), 2435-2443.

224. Dai, L.; Liu, M.; Song, Y.; Liu, J.; Wang, F., Mn3O4-decorated Co3O4 nanoparticles supported on graphene oxide: Dual electrocatalyst system for oxygen reduction reaction in alkaline medium. *Nano Energy* **2016,** *27*, 185-195.

225. Mei, B.-A.; Lau, J.; Lin, T.; Tolbert, S. H.; Dunn, B. S.; Pilon, L., Physical interpretations of electrochemical impedance spectroscopy of redox active electrodes for electrical energy storage. *The Journal of Physical Chemistry C* **2018,** *122* (43), 24499-24511.

226. Wang, X.; Guan, H.; Chen, S.; Li, H.; Zhai, T.; Tang, D.; Bando, Y.; Golberg, D., Self-stacked Co3O4 nanosheets for high-performance lithium ion batteries. *Chemical communications* **2011,** *47* (45), 12280-12282.

227. Saha, S.; Sarkar, P.; Turner, A. P., Interference-free electrochemical detection of nanomolar dopamine using doped polypyrrole and silver nanoparticles. *Electroanalysis* **2014,** *26* (10), 2197-2206.

228. Mikirova, N.; Casciari, J.; Riordan, N.; Hunninghake, R., Clinical experience with intravenous administration of ascorbic acid: achievable levels in blood for different states of inflammation and disease in cancer patients. *Journal of Translational Medicine* **2013,** *11* (1), 191.

229. Ortega, R.; Bresson, C.; Darolles, C.; Gautier, C.; Roudeau, S.; Perrin, L.; Janin, M.; Floriani, M.; Aloin, V.; Carmona, A., Low-solubility particles and a Trojan-horse type mechanism of toxicity: the case of cobalt oxide on human lung cells. *Particle and fibre toxicology* **2014,** *11* (1), 1-18.

230. Papis, E.; Rossi, F.; Raspanti, M.; Dalle-Donne, I.; Colombo, G.; Milzani, A.; Bernardini, G.; Gornati, R., Engineered cobalt oxide nanoparticles readily enter cells. *Toxicology letters* **2009,** *189* (3), 253-259.

231. Chen, Y.; Guo, C.; Lim, L.; Cheong, S.; Zhang, Q.; Tang, K.; Reboud, J., Compact microelectrode array system: tool for in situ monitoring of drug effects on neurotransmitter release from neural cells. *Analytical chemistry* **2008,** *80* (4), 1133-1140.

232. Zhang, G.; Buchler, I. P.; DePasquale, M.; Wormald, M.; Liao, G.; Wei, H.; Barrow, J. C.; Carr, G. V., Development of a PC12 cell based assay for screening catechol-O-methyltransferase inhibitors. *ACS chemical neuroscience* **2019,** *10* (10), 4221-4226.

233. Xiao, F.; Li, Y.; Gao, H.; Ge, S.; Duan, H., Growth of coral-like PtAu–MnO_2 binary nanocomposites on free-standing graphene paper for flexible nonenzymatic glucose sensors. *Biosens. Bioelectron.* **2013,** *41*, 417-423.

234. Chen, D.; Pang, D.; Zhang, S.; Song, H.; Zhu, W.; Zhu, J., Synergistic coupling of $NiCo_2O_4$ nanorods onto porous Co_3O_4 nanosheet surface for tri-functional glucose, hydrogen-peroxide sensors and supercapacitor. *Electrochim. Acta* **2020,** *330*, 135326.

APPENDIX A

THE GlUCOSE EFFECT ON DIRECT ELECTROCHEMISTRY AND ELECTRON TRANSFER REACTION OF GLUCOSE OXIDASE ENTRAPPED IN A CARBON NANOTUBE-POLYMER MATRIX

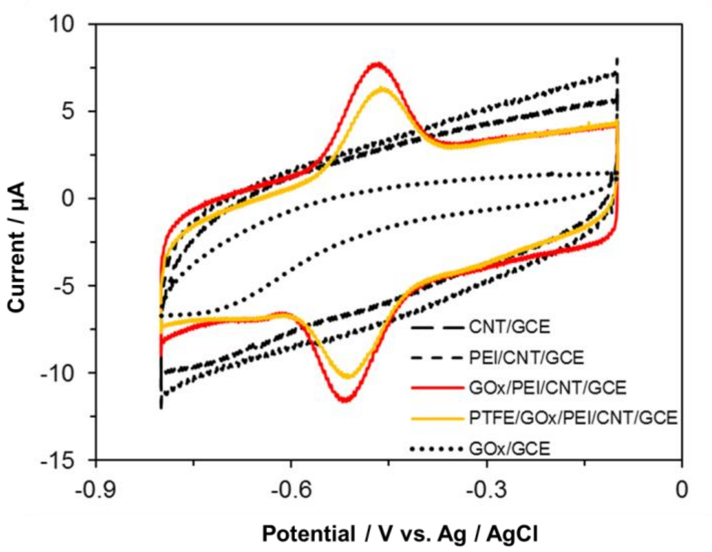

Fig. S2.1 Cyclic Voltammograms for Different Modified Electrodes: Cyclic Voltammograms of the SWCNT/GCE, PEI/SWCNT/GCE, GOx/PEI/SWCNT/GCE, PTFE/GOx/PEI/SWCNT/GCE and GOx/GCE in nitrogen-saturated 0.02 M PBS containing 0.1 M KCl (pH 7.4) at a scan rate of 50 mV s^{-1}.

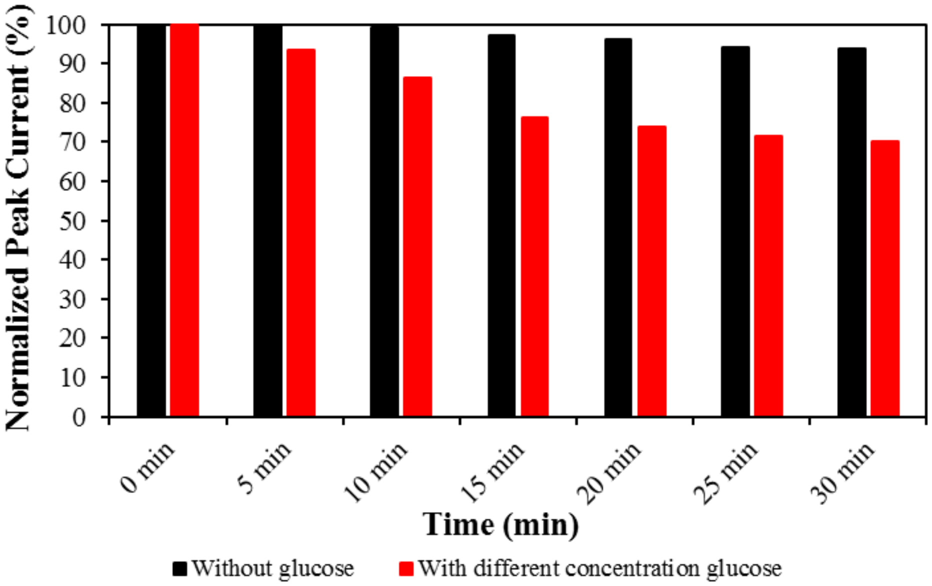

Fig. S2.2 Time Profile for Stability Test: Time profiles for the glassy carbon electrode modified with PTFE/GOx/PEI/SWCNT without glucose at different time incubation for CVs, and in the presence of different concentrations of glucose (red bar left to right:0.0 mM, 1.0 mM, 2.0 mM, 5.0 mM, 10.0 mM, 20.0 mM, and 50.0 mM) at a scan rate of 50 mV s^{-1} at the same time with electrode without adding glucose. It shows that the decrease of peak current is caused by the addition of glucose, not the disability of GOx. The normalized peak current is the Faradaic current of direct CV peaks of GOx immobilized in the electrode.

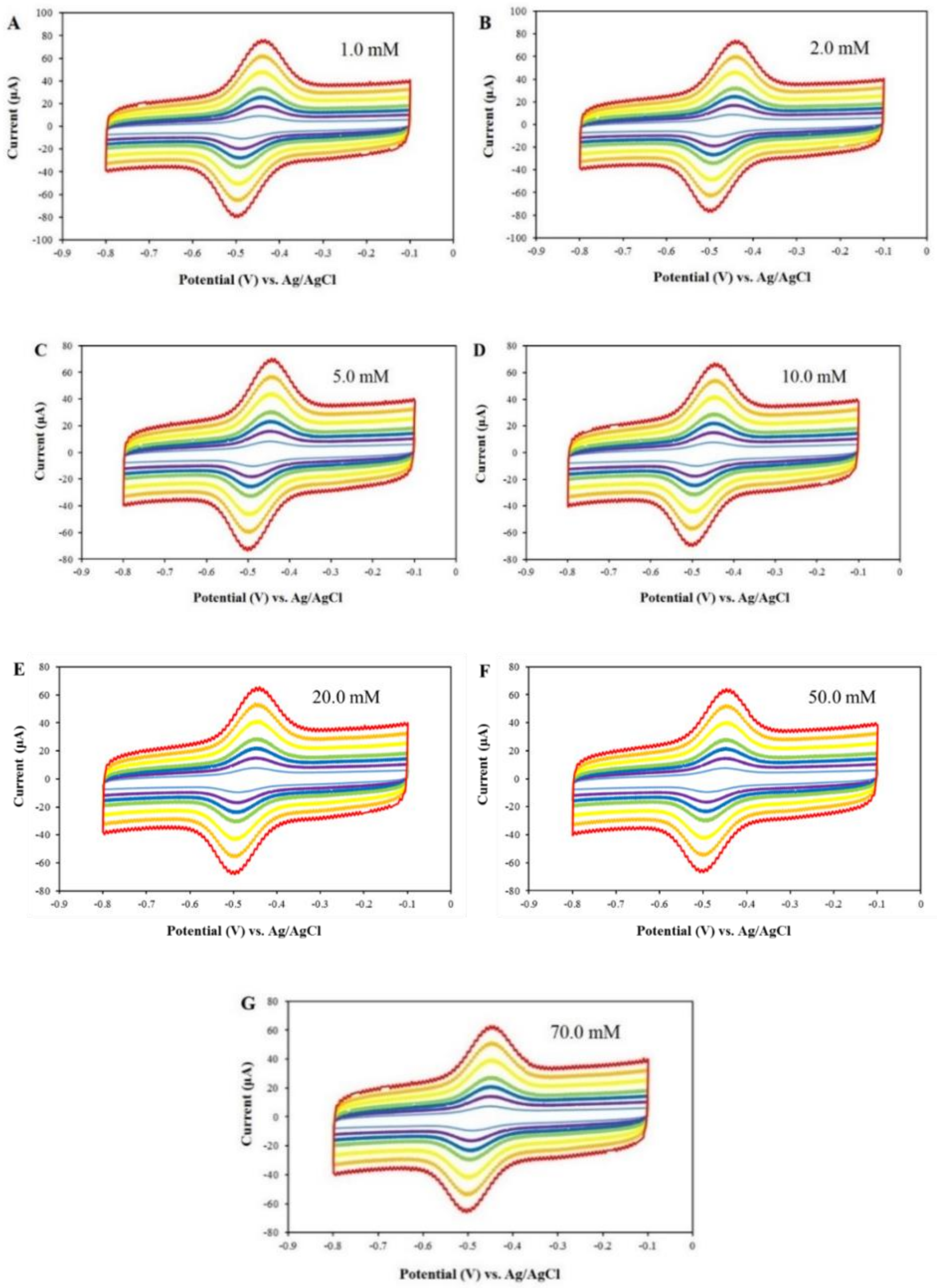

Fig. S2.3 Cyclic Voltammograms under Different Concentration of Glucose: Cyclic voltammograms for the glassy carbon electrode modified with PTFE/GOx/PEI/SWCNT in the presence of glucose under a nitrogen-saturated condition (1.0 mM (A), 2.0 mM (B), 5.0 mM (C), 10.0 mM (D), 20.0 mM (E), 50.0 mM (F), and 70.0 mM (G)). Note that the scan rates are 50 mV s^{-1}, 100 mV s^{-1}, 150 mV s^{-1}, 200 mV s^{-1}, 300 mV s^{-1}, 400 mV s^{-1}, and 500 mV s^{-1}.

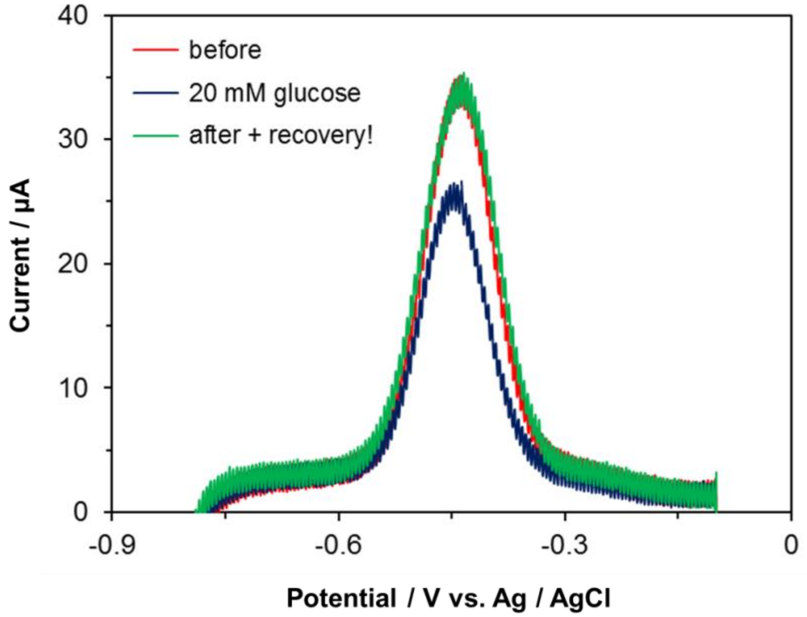

Fig. S2.4 Cyclic Voltammograms for Recovery Experimental Test: the oxidation peaks of the GOx electrode before and after 20 mM glucose addition and recovery of electrode with absence of glucose after the CV experiments.

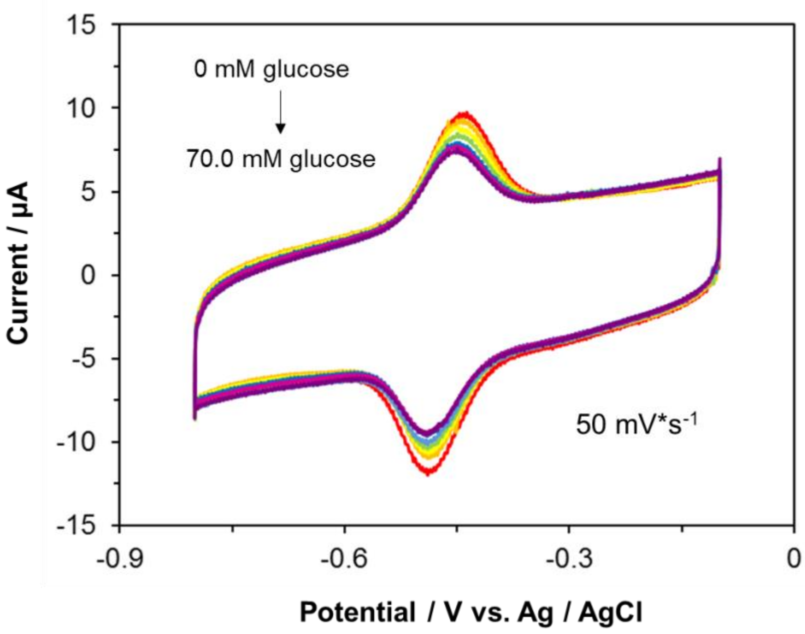

Fig. S2.5 Cyclic Voltammograms at Scan rate of 50 mV*s^{-1}: representative cyclic voltammogram for the glassy carbon electrode modified with PTFE/GOx/PEI/CNTs at the scan rate of 50 mV s^{-1} under different concentrations of glucose.

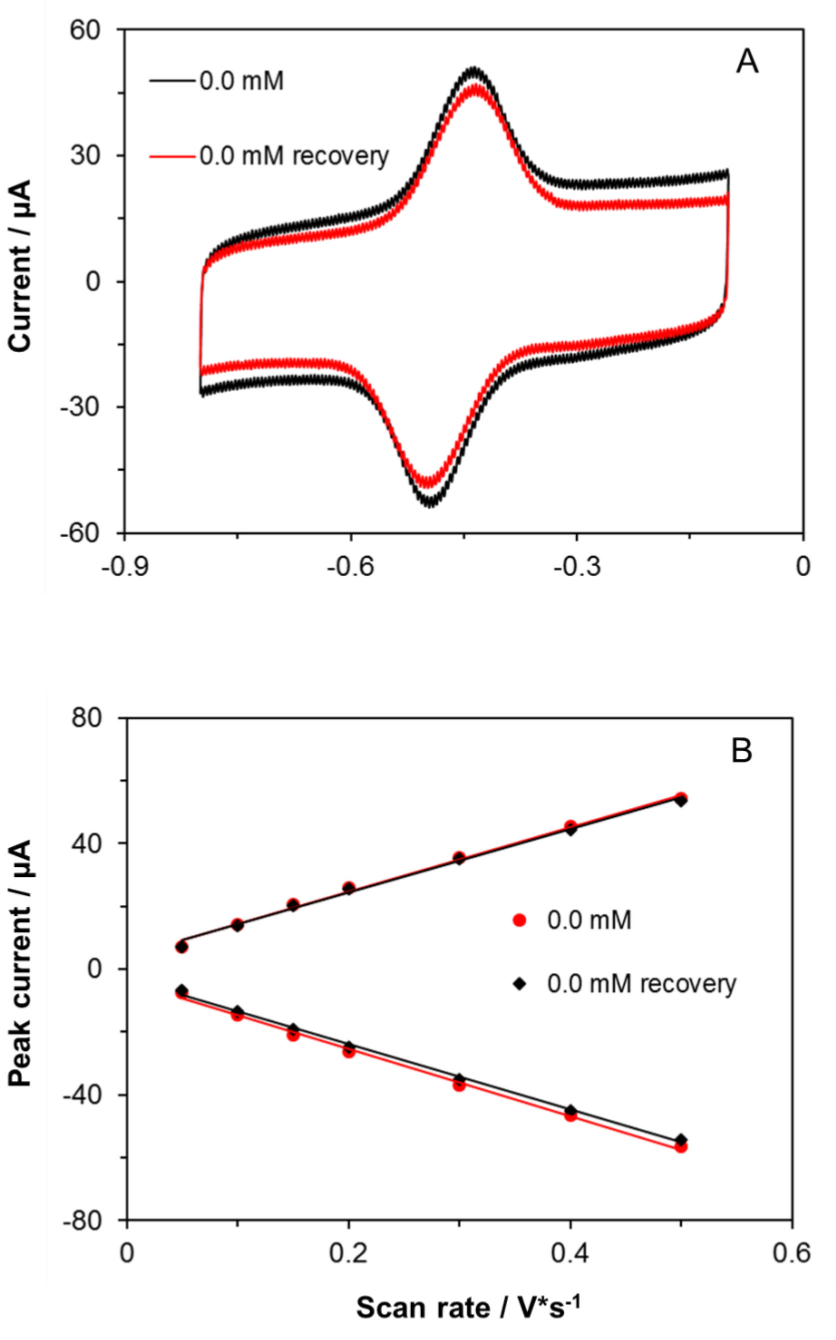

Fig. S2.6 Cyclic Voltammograms and Linear Dependce of I_P versus ν: (A) Cyclic voltammograms for the PTFE/GOx/PEI/SWCNTs/GCE system in the absence of glucose before and after a series of glucose concentration experiments at a scan rate of 300 mV s^{-1}. (B) The linear dependence of the peak current on the voltage scan rate in the absence of glucose before and after a series of glucose concentration experiments.

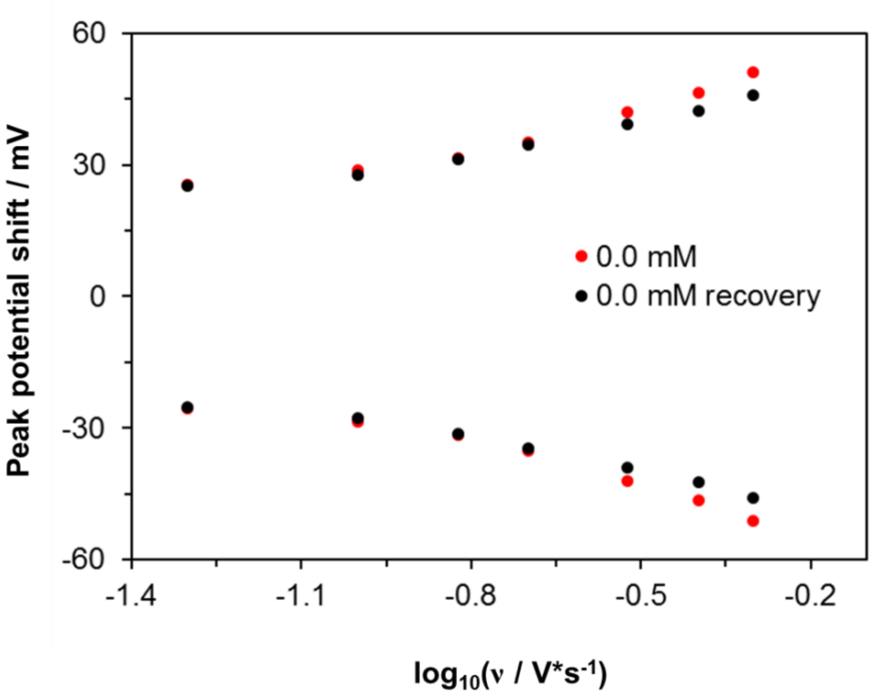

Fig.S2.7 The Dependence of ΔE versus log (ν) for k^0 Calculation: the dependence of the peak potential shift on the scan rate in the absence of glucose before and after a series of glucose concentration experiments.

TABLE S2.1

ET RATE CONSTANT DATA OF THE GOX OBTAINED BY MARCUS MODEL AND LAVIRON METHOD.

Concentrations (mM)	Extended Marcus Method (0.3 eV) (s^{-1})	Extended Marcus Method (0.5 eV) (s^{-1})	Extended Marcus Method (0.8 eV) (s^{-1})	Laviron Method (s^{-1})
0.0	3.74±0.08	3.84±0.05	3.91±0.04	3.51±0.26
1.0	3.95±0.08	4.03±0.07	4.10±0.03	3.78±0.33
2.0	4.26±0.05	4.36±0.11	4.53±0.02	4.42±0.53
5.0	4.72±0.09	4.83±0.03	5.08±0.03	4.78±0.57
10.0	5.06±0.10	5.24±0.04	5.54±0.08	5.35±0.84
20.0	5.30±0.05	5.50±0.09	5.79±0.04	5.92±0.89
50.0	5.33±0.04	5.52±0.08	5.80±0.03	5.95±0.95
70.0	5.38±0.03	5.52±0.10	5.82±0.03	6.01±0.95
0.0 (after)	3.80±0.05	3.89±0.02	3.96±0.05	3.70±0.34

APPENDIX B

MINGLED MNO2 AND CO3O4 BINARY NANOSTRUCTURES ON WELL-ALIGNED ELECTROSPUN CARBON NANOFIBERS FOR NONENZYMATIC GLUCOSE OXIDATION AND SENSING

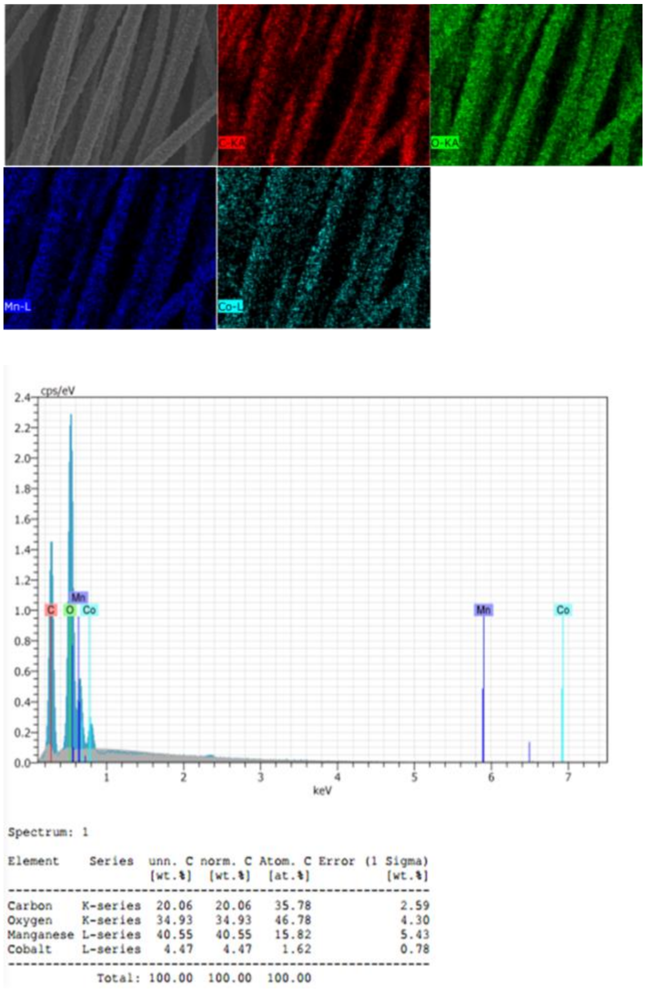

```
Spectrum: 1

Element    Series   unn. C norm. C Atom. C Error (1 Sigma)
                    [wt.%]  [wt.%]  [at.%]          [wt.%]
-----------------------------------------------------------
Carbon    K-series  20.06   20.06   35.78            2.59
Oxygen    K-series  34.93   34.93   46.78            4.30
Manganese L-series  40.55   40.55   15.82            5.43
Cobalt    L-series   4.47    4.47    1.62            0.78
-----------------------------------------------------------
             Total: 100.00  100.00  100.00
```

Fig. S3.1 EDX Mapping Images: SEM associated with EDX mapping images and analysis of the MnO_2/Co_3O_4@ECNFs. The red, green, blue and cyan indicate the element distribution of C, O, Mn and Co, respectively.

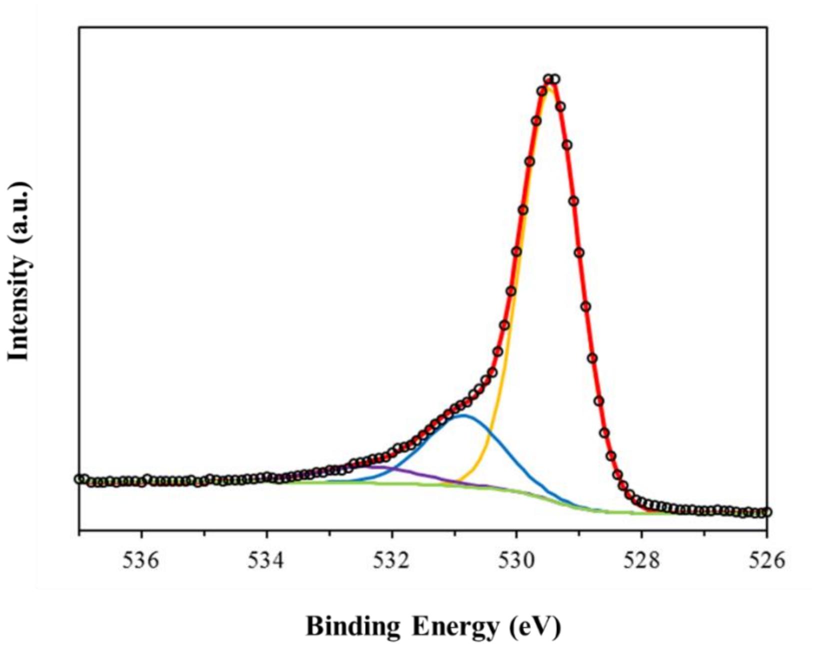

Fig. S3.2 XPS spectra: high resolution for XPS spectrum O(1s) of the MnO$_2$/Co$_3$O$_4$@ECNFs.

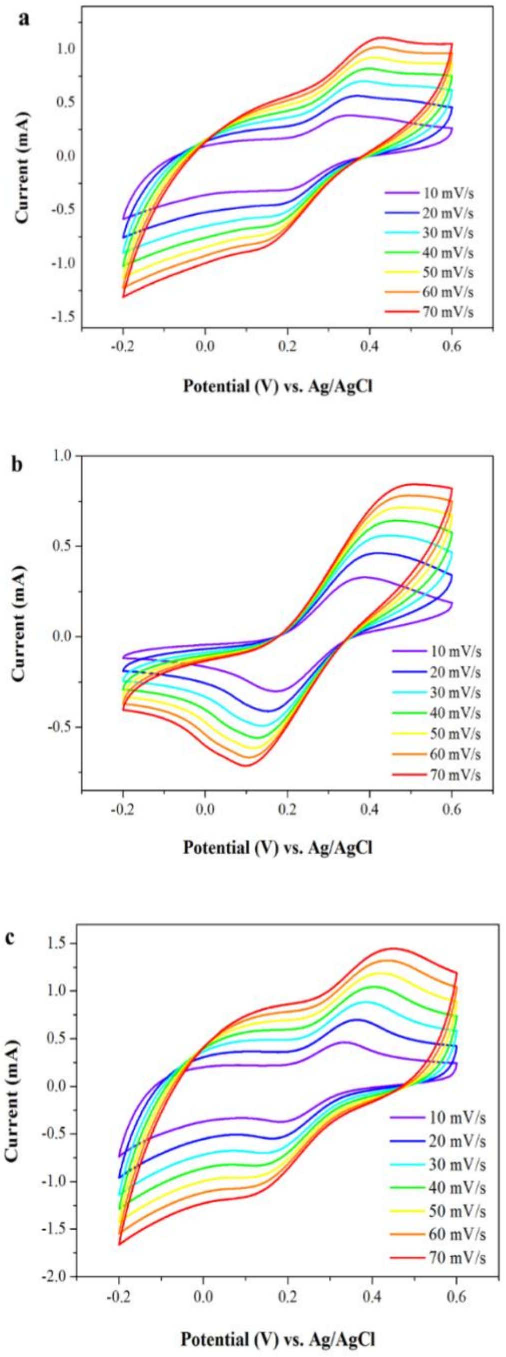

Fig. S3.3 Cyclic Voltammograms for Different Modified Electrodes: Cyclic Voltammograms (CVs) of different modified GC electrode (a: MnO_2/ECNFs, b: Co_3O_4/ECNFs, c: MnO_2/Co_3O_4@ECNFs) immersed in 0.6 M NaOH containing 5 mM $[Fe(CN)_6]^{3-}$, scan rate from 10 to 70 mV s-^{1}.

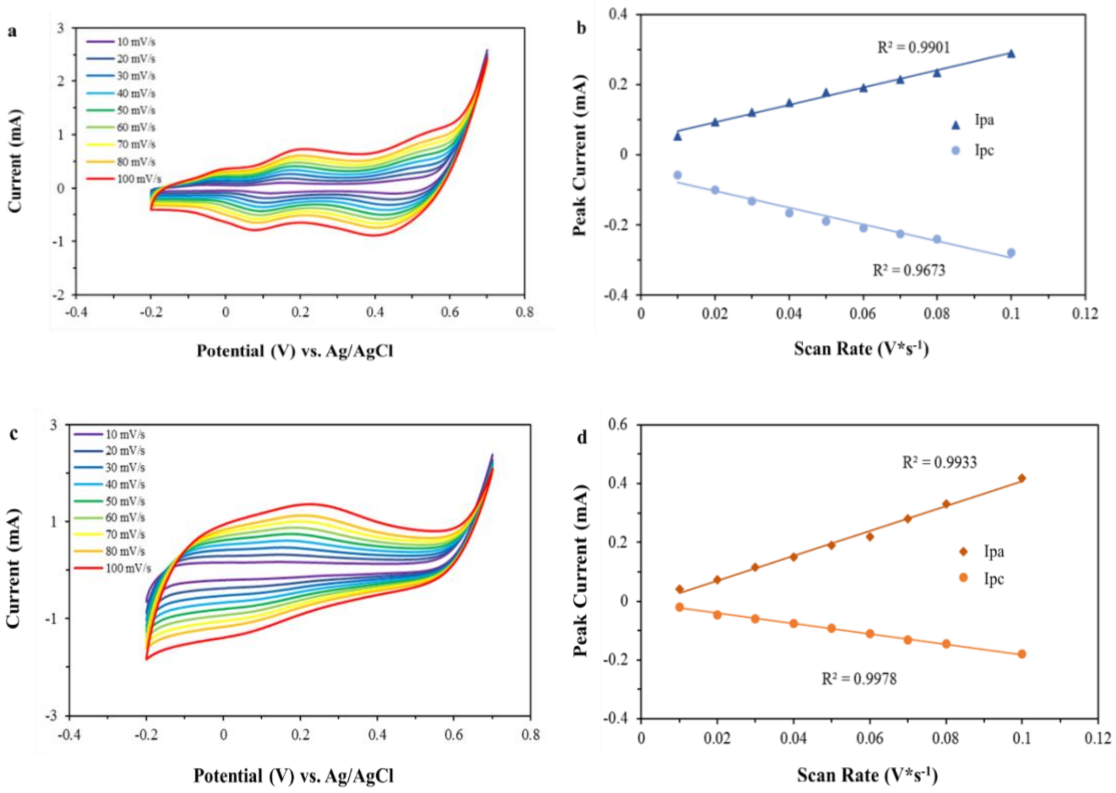

Fig. S3.4 Cyclic Voltammograms and Linear Dependence of I_P versus $\nu^{1/2}$: CV curves of the Co_3O_4@ECNFs (a) and MnO_2@ECNFs (c) with different scan rates (10, 20, 30, 40, 50, 60, 70, 80 and 100 mV/s) in 0.6 M NaOH; and the plot of peak currents vs. scan rates of the Co_3O_4@ECNFs (b) and MnO_2@ECNFs (d).

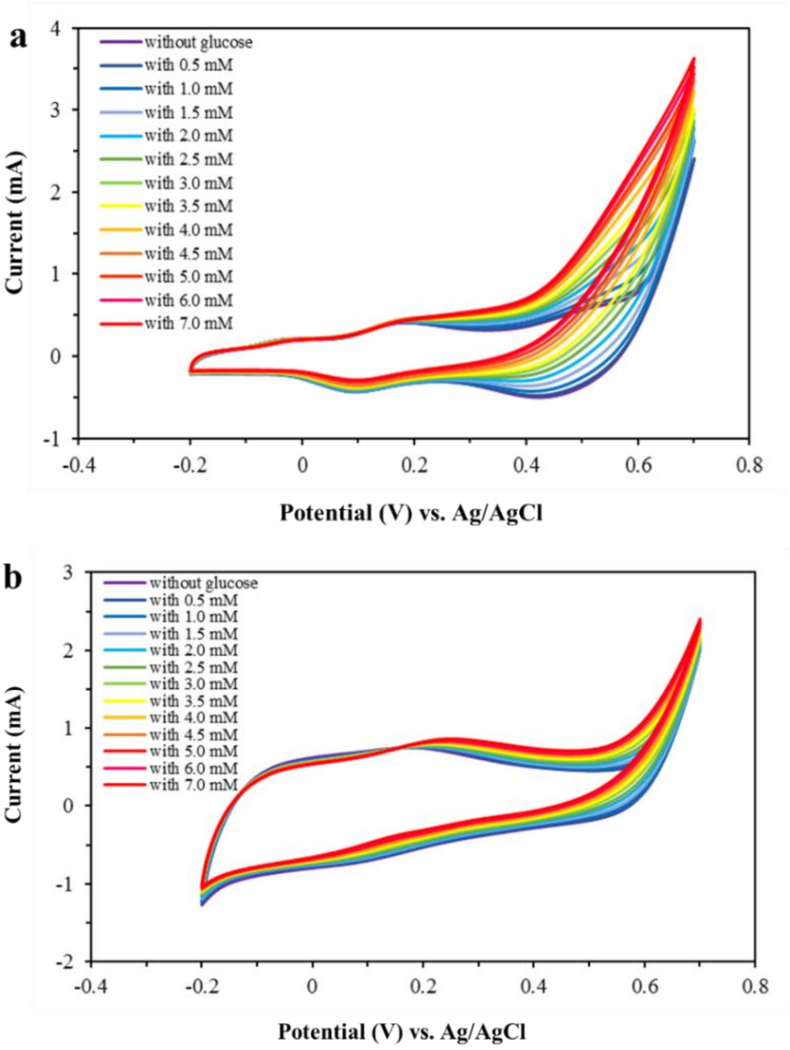

Fig. S3.5 Cyclic Voltammograms for Electrocatalytic Performance Test: cyclic voltammograms of Co_3O_4@ECNFs (a) and MnO_2@ECNFs (b) at various concentrations of glucose, in the range from 0.5 to 7 mM, with a scan rate of 50 mV/s.

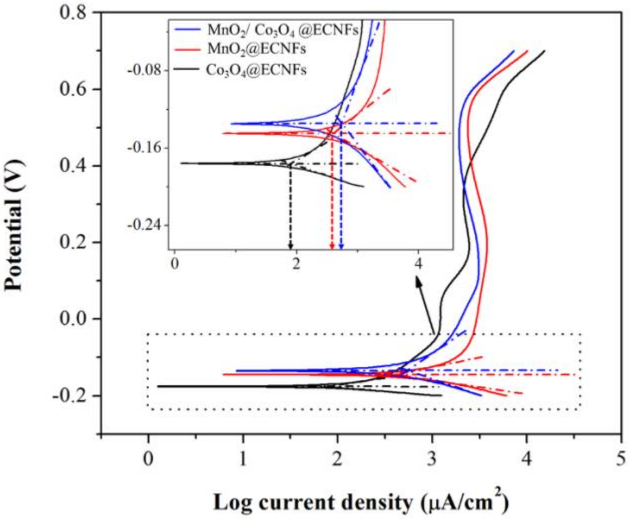

Fig. S3.6 Tafel plots for the analysis of various developed electrodes with 1 mM glucose oxidation reaction.

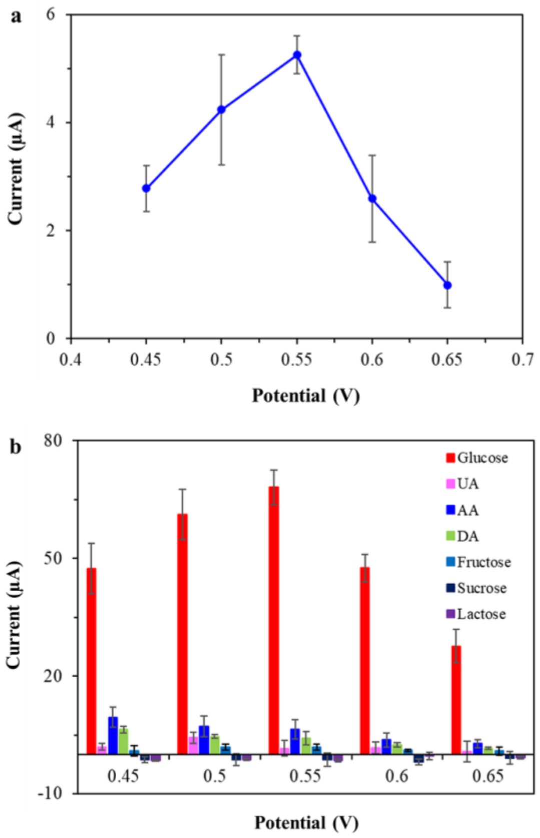

Fig. S3.7 Amperometric Test under Different Applied Voltages: amperometric response of the MnO_2/Co_3O_4@ECNFs sensor (a) with presence of 10 µM glucose and (b) with addition of interference species at 0.02M of each at glucose concentration of 0.2 M under different applied voltages vs. Ag/AgCl.

TABLE S3.1

THE COMPARISON OF SENSING PERFORMANCE OF THE PROPOSED GLUCOSE SENSOR WITH OTHER REPORTED MNO2- AND Co3O4- BASED MATERIALS

Electrode Material	**Linear Range**	**Sensitivity (μA mM^{-1} cm^{-2})**	**Detection Limit**	**Ref, Publishing year**
PtAu-MnO_2/Graphene	0.1 mM-30.0 mM	58.54	0.02 mM	[233]
Co_3O_4 NF	20 µM-2.04 mM	36.25	0.97 µM	[171]
MnO_2 nanorods/Co_3O_4	60 µM-7 mM	127	0.03 µM	[34]
MnO_2/CNTs	5.0 µM-1.0 mM	3406.4	0.5 µM	[39]
Co_3O_4 NOE	0.5 µM-1.0 mM	64.71	0.012 µM	[33]
Co_3O_4-HND	2.0 µM-6.06 mM	708.4	0.58 µM	[177]
$NiCo_2O_4$	5 µM-1.00 mM	2100	0.38 µM	[234]
MnO_2/Co_3O_4@ECNFs	5 µM-1.93 mM	1159	0.3 µM	In this work

TABLE S3.2

DETERMINATION RESULTS OF GLUCOSE SPIKED IN HUMAN SERUM SAMPLES.

Samples	**Spiked (mM)**	**Found (mM)**	**Recovery (%)**	**R.S.D. (%)**
Serum 1	3.76	3.73	99.2	2.02
Serum 2	4.34	4.38	100.9	3.62
Serum 3	5.00	5.02	100.4	2.11

APPENDIX C

GROWTH COBALT OXIDE NANOGRAINS ON N-DOPED ALIGNED ELECTROSPUN CARBON NANOFIBERS FOR ELECTROCHEMICAL DETECTION OF DOPAMINE SECRETED BY LIVING CELLS

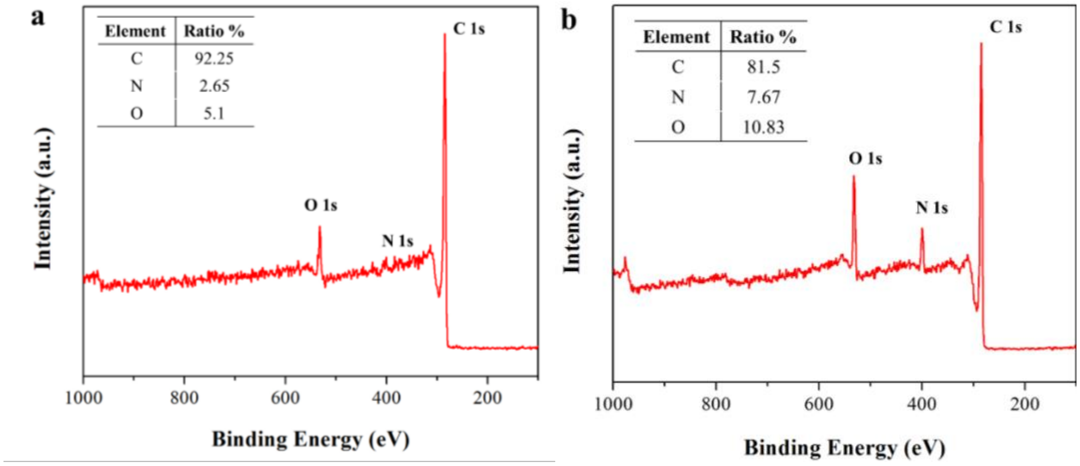

Element	Ratio %
C	92.25
N	2.65
O	5.1

Element	Ratio %
C	81.5
N	7.67
O	10.83

Fig. S4.1 XPS survey spectra of pristine electrospun carbon nanofibers (ECNFs) (a) and N-doped electrospun carbon nanofibers (NECNFs) (b).

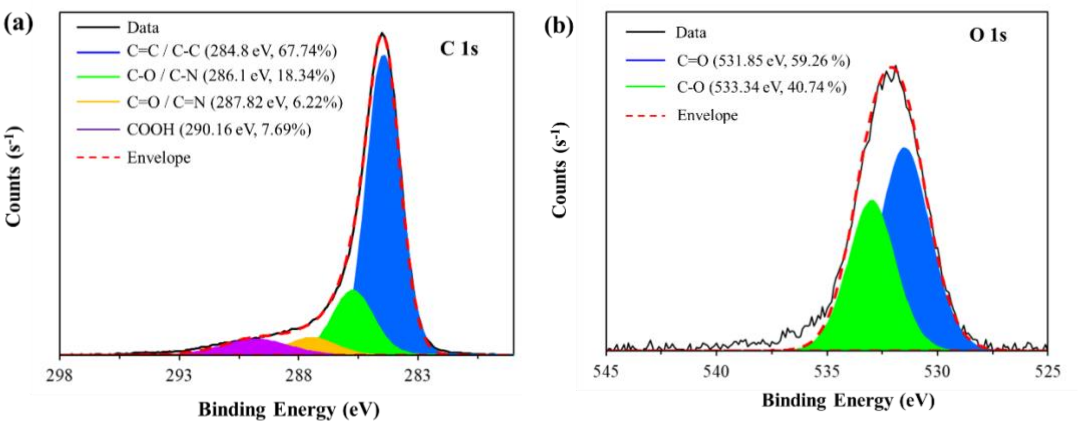

Fig. S4.2 XPS Spectra: high-resolution C1s and O1s XPS spectra of AECNFs.

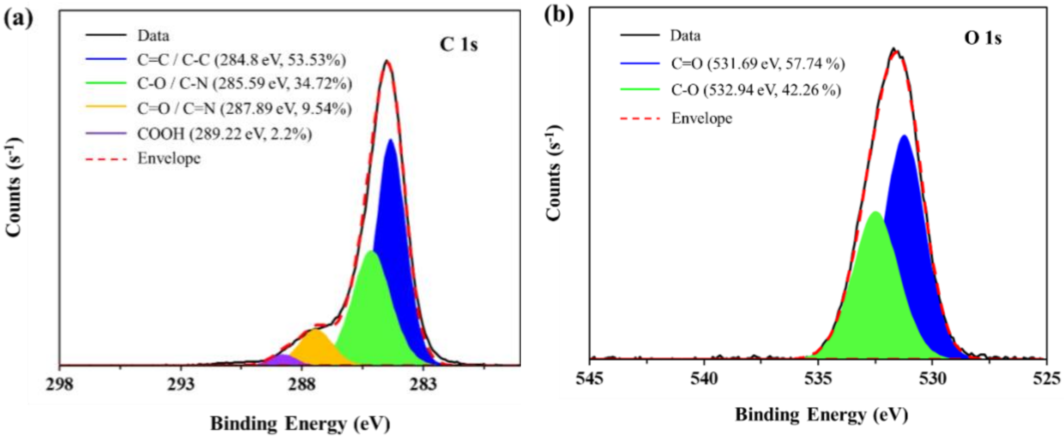

Fig. S4.3 XPS Spectra: high-resolution C 1s and O 1s XPS spectra of NECNFs.

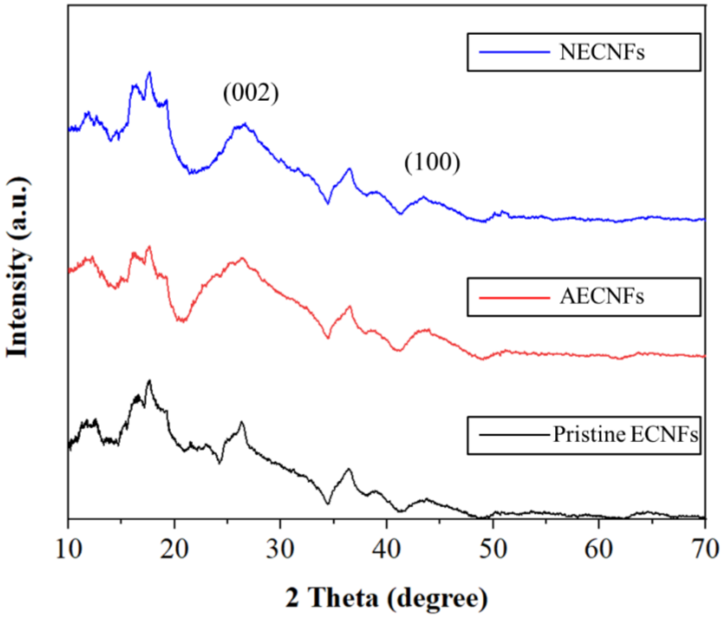

Fig. S4.4 XRD patterns of the pristine ECNFs, AECNFs and NECNFs.

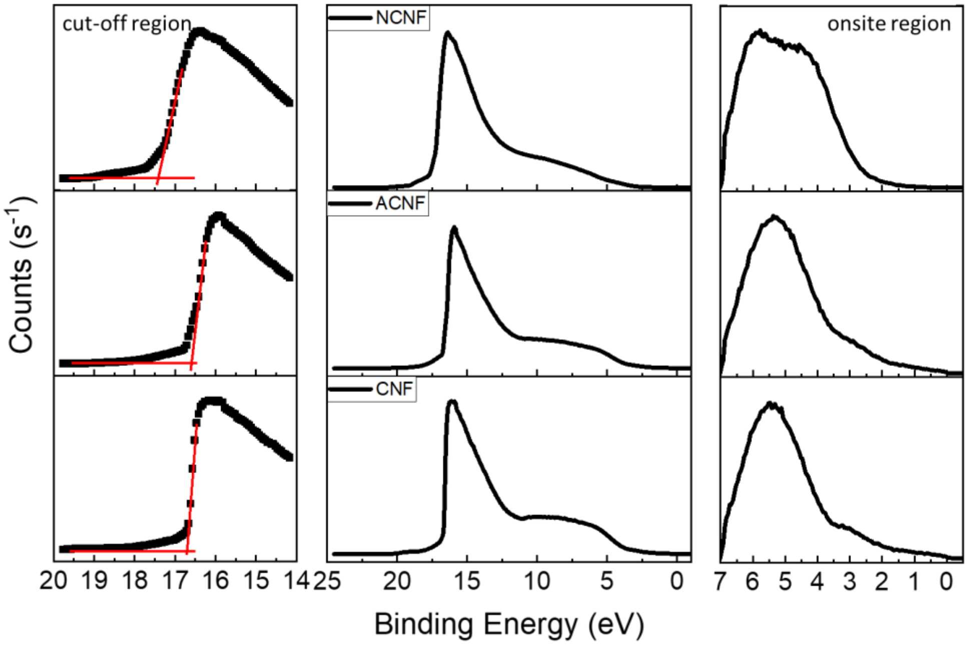

Fig. S4.5 UPS spectra of pristine ECNFs, AECNFs and NECNFs.

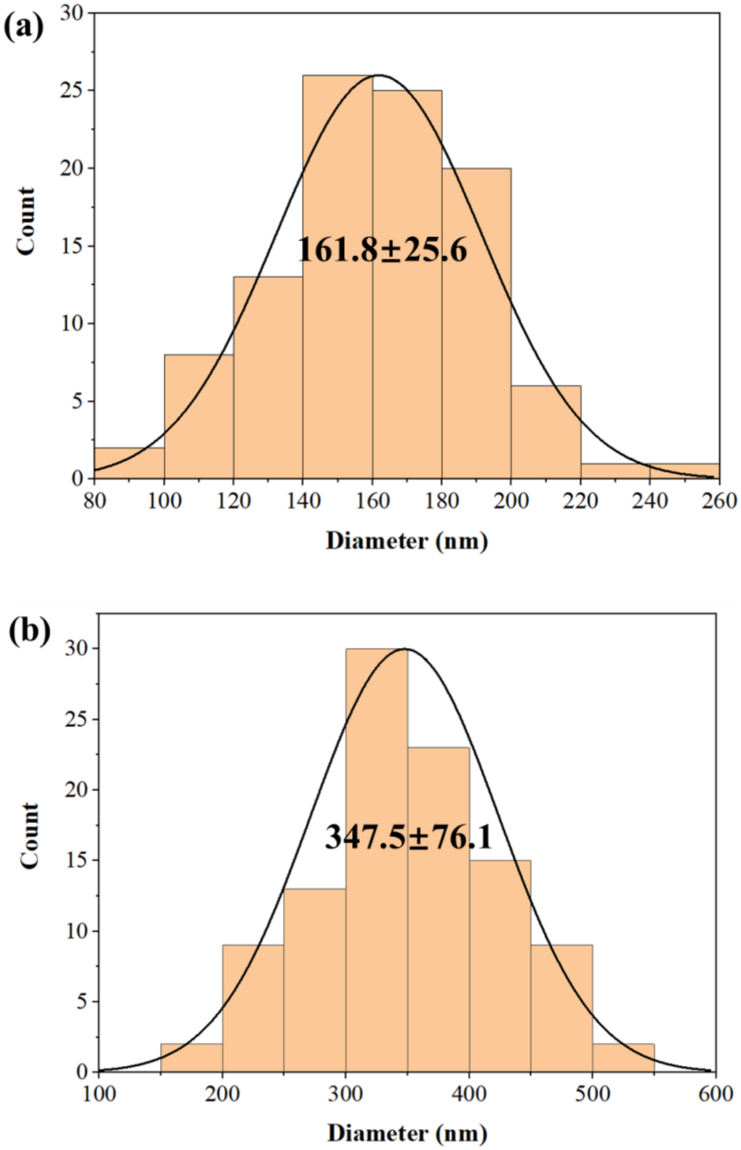

Fig. S4.6 Size Distribution Histograms: Co_3O_4 nanograins size distribution growth on to nitrogen doped ECNFs with different electrodeposition hours, 2h (a) and 4h (b).

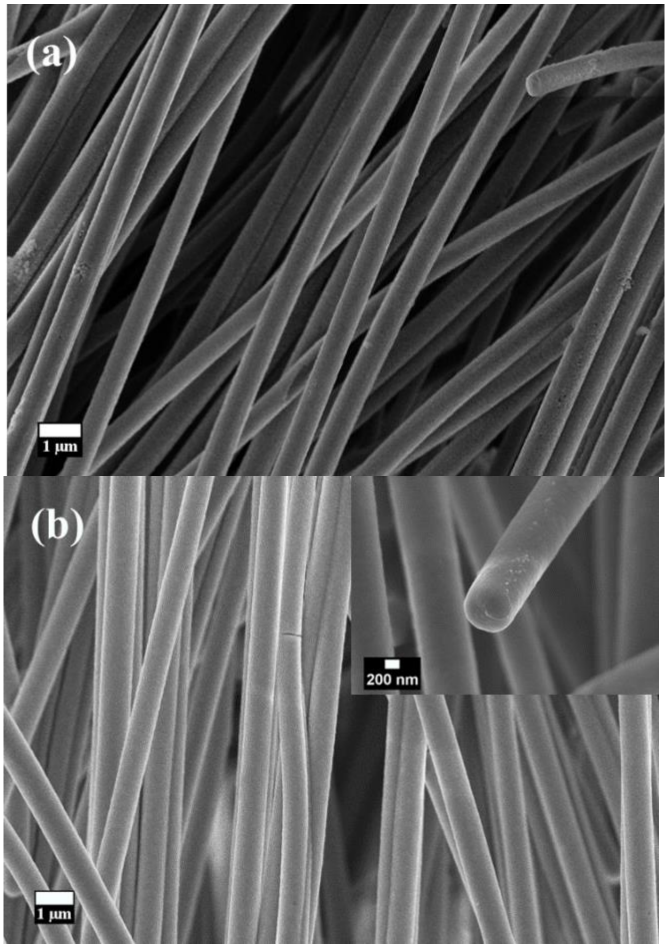

Fig. S4.7 SEM images of cobalt oxide nanofilm electrodeposits onto AECNFs with 2h (a) and 4h (b). Diameter of fibers: 527 ±41 nm (a) and 734 ± 66 nm (b).

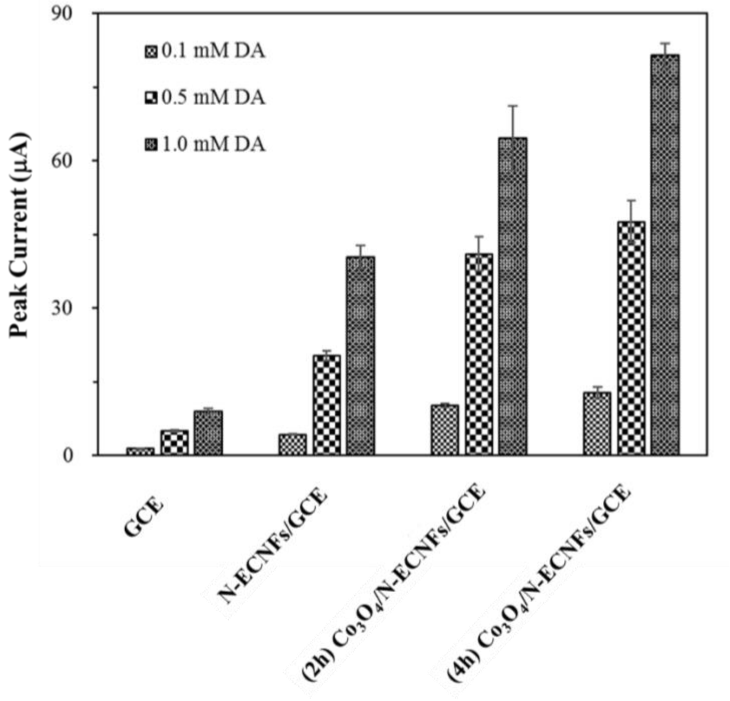

Fig. S4.8 Peak Current Histograms of Electrochemical Oxidation: peak current of electrocatalytic oxidation towards DA over different electrode materials.

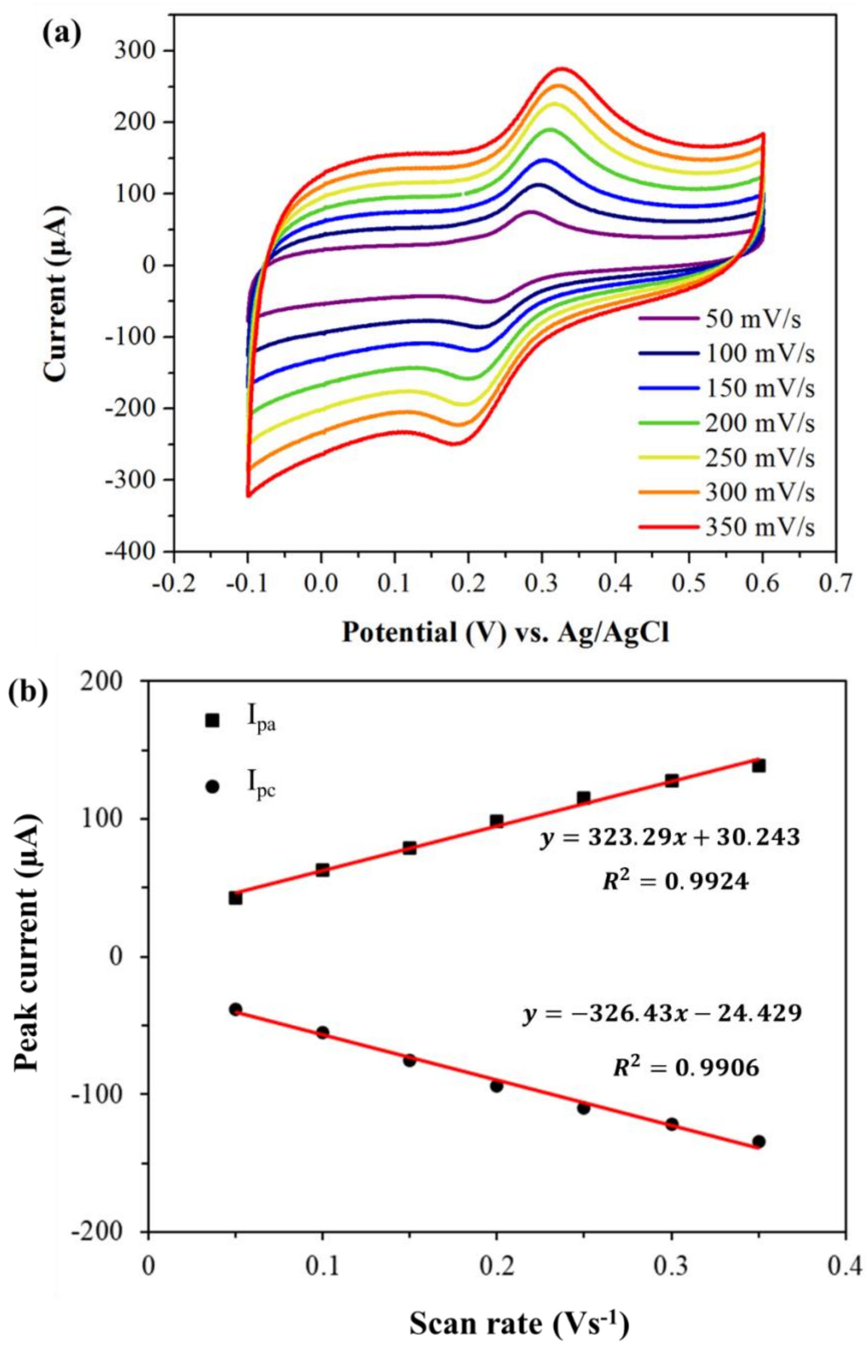

Fig. S4.9 Cyclic Voltaommograms and Linear Dependence of I_P versus $\nu^{1/2}$: 4h Co_3O_4/NECNFs in 0.1 M PBS (pH 7.4) containing 0.5 mM DA (a) CVs at different scan rates. (b) The plots of peak current versus scan rate.

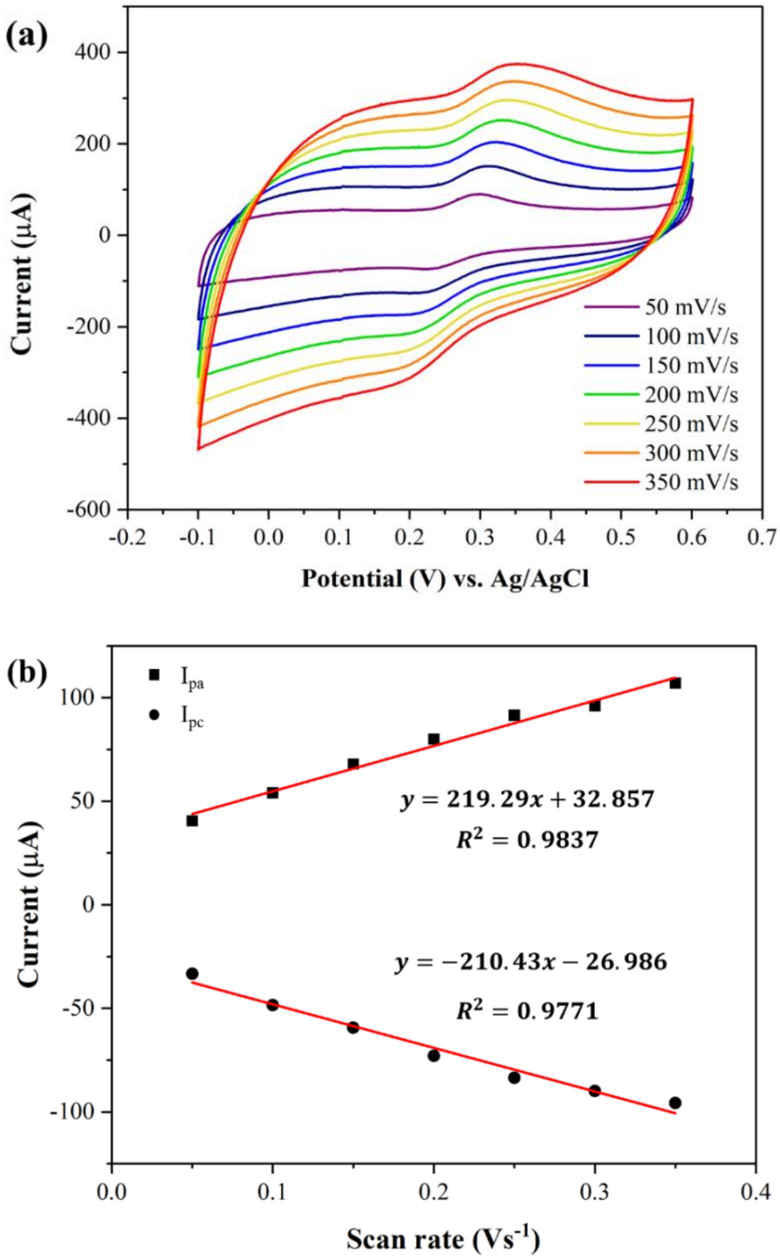

Fig. S4.10 Cyclic Voltaommograms and Linear Dependence of I_P versus $\nu^{1/2}$: 4h Co_3O_4/AECNFs in 0.1 M PBS (pH 7.4) containing 0.5 mM DA (a) CVs at different scan rates. (b) The plots of peak current versus scan rate.

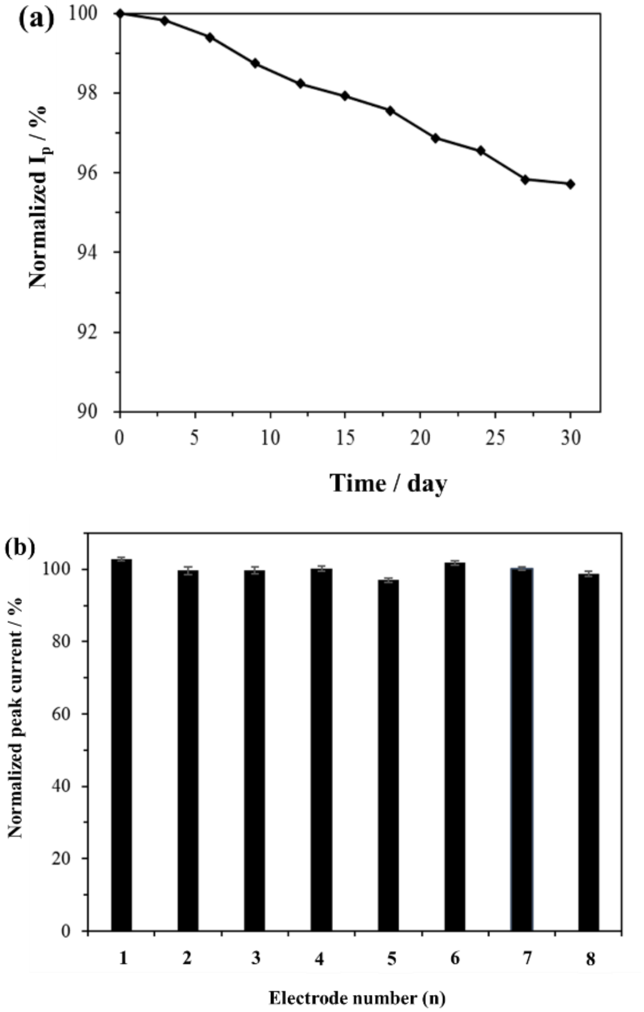

Fig. S4.11 Stability and Reproducibility Tests: the plot of normalized peak currents of DPV responses for 0.05 mM DA over different periods for stability test (a) and seperately 4h Co_3O_4@NECNFs electrodes for reprodicibility test (b).

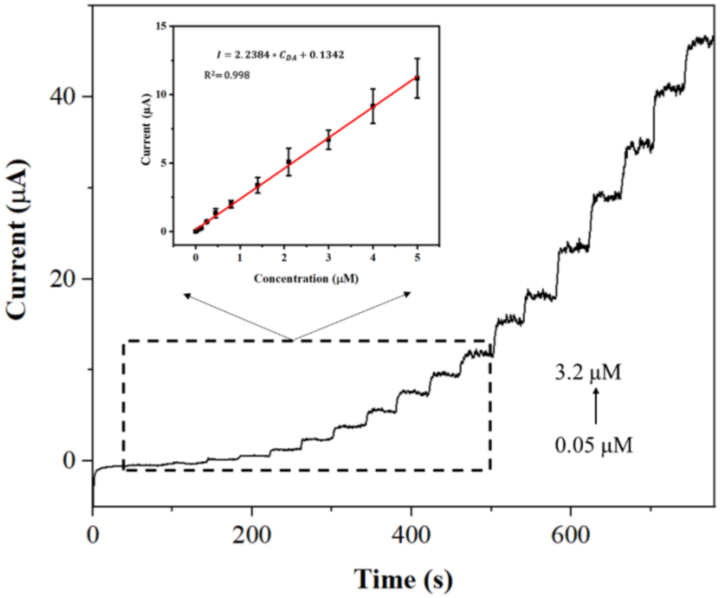

Fig. S4.12 Amperometric Test: amperometric response of 4h Co_3O_4@NECNFs electrode to a serial of DA concentration and inset shows the calibration curve of current response with the dotted rectangular section.

TABLE S4.1

THE PEAK FITTING STOICHIOMETRY OF N1S FOR NECNFS

Name	Peak BE (eV)	Atomic (%)
gN	401.1	22.61
rN	400.0	39.93
pN	398.9	37.47

TABLE S4.2

COMPARISON OF DIFFERENT NANOMATERIALS-BASED ELECTROCHEMCIAL SENSORS FOR DETECTION OF DA

electrode	limit of detection (LOD) (µM)	linear range (µM)	reference
Pt/rGO	0.005	0.087~100	[60]
rGO/CD/CF	0.02	0.1~100	[62]
Co_3O_4/rGO	0.277	1~30	[108]
PA6/PAH	0.15	1~70	[57]
AuNP/NG	0.01	0.03~48	[202]
ND_H	0.05	0.05~1000	[203]
Fe_3O_4/rGO	0.007	0.01~100.55	[204]
NiO NLF	0.008	0.5~5	[52]
HCSs	0.6	3~2000	[209]
CuO/2D g-C_3N_4	0.0001	0.002~71.1	[210]
GODs-MWCNFs	0.87	0.005~100	[211]
3D-N-Graphene	0.001	3~100	[212]
CAuNE	5.83	1~100	[59]
Ni-MOF/AuNPs/CNTs	0.01	0.05~15	[56]
Co_3O_4/NECNFs	0.02	0.05~100	This work

TABLE S4.3

DETECTION RESULTS OF DA IN HUMAN SERUM (N=6)

human serum	spiked (μM)	found (μM)	recovery (%)	RSD (%)
sample 1	5.0	5.08±0.18	101.6	1.6
sample 2	10.0	9.96±0.22	99.6	1.1
sample 3	15.0	15.04±0.52	100.3	1.7
sample 4	20.0	20.33±0.66	101.7	1.5
sample 5	25.0	24.89±0.97	99.6	1.9